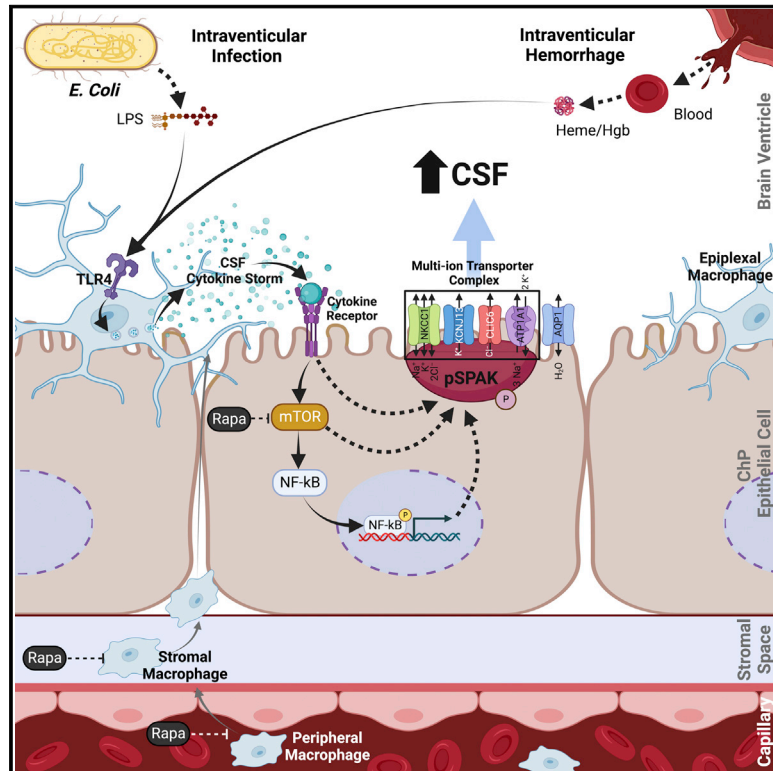


The choroid plexus links innate immunity to CSF dysregulation in hydrocephalus

Graphical abstract



Authors

Stephanie M. Robert,
Benjamin C. Reeves, Emre Kiziltug, ...,
Seth L. Alper, Eric Delpire,
Kristopher T. Kahle

Correspondence

kahle.kristopher@mgh.harvard.edu

In brief

Infectious and hemorrhagic hydrocephalus converge on highly similar immune and secretory responses at the choroid plexus that drive pathological cerebrospinal fluid secretion, thus opening up immunomodulation as a potential non-surgical intervention.

Highlights

- Integrated multi-omics study of infectious and hemorrhagic hydrocephalus
- Blood or bacteria in CSF elicit highly similar ChP immune and secretory responses
- Crosstalk between ChP immune and epithelial cells drives pathologic CSF secretion
- Immunomodulators treat PIH/PHH by antagonizing a SPAK-regulated ChP transportome



Article

The choroid plexus links innate immunity to CSF dysregulation in hydrocephalus

Stephanie M. Robert,^{1,24} Benjamin C. Reeves,^{1,24} Emre Kiziltug,^{1,24} Phan Q. Duy,^{1,24} Jason K. Karimy,¹ M. Shahid Mansuri,^{1,2,24} Arnaud Marlier,¹ Garrett Allington,^{1,3} Ana B.W. Greenberg,¹ Tyrone DeSpensa, Jr.,¹ Amrita K. Singh,¹ Xue Zeng,¹ Kedous Y. Mekbib,¹ Adam J. Kundishora,¹ Carol Nelson-Williams,¹ Le Thi Hao,¹ Jinwei Zhang,⁴ TuKiet T. Lam,^{2,5} Rashaun Wilson,^{2,5} William E. Butler,⁶ Michael L. Diluna,¹ Philip Feinberg,^{7,8} Dorothy P. Schafer,⁷ Kiavash Movahedi,^{9,10} Allen Tannenbaum,^{11,12} Sunil Koundal,¹³ Xinan Chen,¹⁴ Helene Benveniste,¹³ David D. Limbrick, Jr.,¹⁵ Steven J. Schiff,¹ Bob S. Carter,⁶ Murat Gunel,¹ J. Marc Simard,^{16,17,18} Richard P. Lifton,¹⁹ Seth L. Alper,²⁰ Eric Delpire,²¹ and Kristopher T. Kahle^{6,22,23,25,*}

¹Department of Neurosurgery, Yale School of Medicine, New Haven, CT 06520, USA

²Department of Molecular Biophysics and Biochemistry, Yale University School of Medicine, New Haven, CT 06520, USA

³Department of Pathology, Yale School of Medicine, New Haven, CT 06520, USA

⁴Institute of Biomedical and Clinical Sciences, University of Exeter Medical School, Hatherly Laboratory, Exeter EX1 2LU, UK

⁵Keck MS & Proteomics Resource, Yale University School of Medicine, New Haven, CT 06520, USA

⁶Department of Neurosurgery, Massachusetts General Hospital and Harvard Medical School, Boston, MA 02114, USA

⁷Department of Neurobiology, Brudnick Neuropsychiatric Research Institute University of Massachusetts Chan Medical School, Worcester, MA 01655, USA

⁸Medical Scientist Training Program, UMass Chan Medical School, Worcester, MA 01655, USA

⁹Laboratory of Cellular and Molecular Immunology, Vrije Universiteit Brussel, 1050 Brussels, Belgium

¹⁰Myeloid Cell Immunology Laboratory, VIB Center for Inflammation Research, 1050 Brussels, Belgium

¹¹Department of Applied Mathematics and Statistics, Stony Brook University, Stony Brook, NY 11794, USA

¹²Department of Medical Physics, Memorial Sloan Kettering Cancer Center, New York City, NY 11794, USA

¹³Department of Anesthesiology, Yale School of Medicine, New Haven, CT 06520, USA

¹⁴Department of Applied Mathematics and Statistics, Stony Brook University, Stony Brook, NY 11794, USA

¹⁵Department of Neurosurgery, Washington University School of Medicine, St. Louis, MO 63110, USA

¹⁶Department of Neurosurgery, University of Maryland, School of Medicine, Baltimore, MD 21201, USA

¹⁷Department of Pathology, University of Maryland, School of Medicine, Baltimore, MD 21201, USA

¹⁸Department of Physiology, University of Maryland, School of Medicine, Baltimore, MD 21201, USA

¹⁹Laboratory of Human Genetics and Genomics, the Rockefeller University, New York, NY 10065, USA

²⁰Department of Medicine, Harvard Medical School, Boston, MA 02115, USA

²¹Department of Anesthesiology, Vanderbilt University School of Medicine, Nashville, TN 37232, USA

²²Broad Institute of Harvard and MIT, Cambridge, MA, 02142, USA

²³Department of Neurosurgery and Division of Genetics and Genomics, Boston Children's Hospital, Boston, MA, USA

²⁴These authors contributed equally

²⁵Lead contact

*Correspondence: kahle.kristopher@mgh.harvard.edu

<https://doi.org/10.1016/j.cell.2023.01.017>

SUMMARY

The choroid plexus (ChP) is the blood-cerebrospinal fluid (CSF) barrier and the primary source of CSF. Acquired hydrocephalus, caused by brain infection or hemorrhage, lacks drug treatments due to obscure pathobiology. Our integrated, multi-omic investigation of post-infectious hydrocephalus (PIH) and post-hemorrhagic hydrocephalus (PHH) models revealed that lipopolysaccharide and blood breakdown products trigger highly similar TLR4-dependent immune responses at the ChP-CSF interface. The resulting CSF “cytokine storm”, elicited from peripherally derived and border-associated ChP macrophages, causes increased CSF production from ChP epithelial cells via phospho-activation of the TNF-receptor-associated kinase SPAK, which serves as a regulatory scaffold of a multi-ion transporter protein complex. Genetic or pharmacological immunomodulation prevents PIH and PHH by antagonizing SPAK-dependent CSF hypersecretion. These results reveal the ChP as a dynamic, cellularly heterogeneous tissue with highly regulated immune-secretory capacity, expand our understanding of ChP immune-epithelial cell cross talk, and reframe PIH and PHH as related neuroimmune disorders vulnerable to small molecule pharmacotherapy.



INTRODUCTION

The choroid plexus (ChP) projects into each of the four cerebrospinal fluid (CSF)-filled ventricles and comprises an epithelial cell sheet populated by immune and mesenchymal cell types.^{5,6} The ChP is the body's secretory epithelium par excellence, producing a half-liter of CSF per day via the concerted action of its multiple ion and water transport molecules.⁷ The ChP is also the blood-CSF barrier, gating circulating immune cell entry into the CSF in the setting of infection or tissue damage.^{8–12} The ChP's location at the nexus of the CSF, brain parenchyma, and systemic circulation allows it to sense perturbations and transduce danger signals into homeostatic responses. However, the cellular and molecular mechanisms that coordinate the immune and secretory functions of the ChP are poorly understood.

Hydrocephalus is characterized by the expansion of the cerebral ventricles (ventriculomegaly). Post-infectious hydrocephalus (PIH) and post-hemorrhagic hydrocephalus (PHH), the most common forms of hydrocephalus, are treated by neurosurgical CSF diversion with or without ChP cauterization to decrease CSF production.^{13–15} These life-saving operations have significant long-term morbidity and failure rates, and are unavailable in impoverished areas.^{14,16,17} Furthermore, ChP cauterization may also disrupt normal ChP functions important for brain development and immune function.¹⁸ Drug treatments for hydrocephalus remain unavailable.¹⁸ An improved understanding of ChP biology could identify therapeutic targets for hydrocephalus and other CSF disorders and neuroimmune diseases.^{8,12,18–21}

PIH and PHH are commonly attributed to intraventricular CSF accumulation secondary to decreased CSF reabsorption due to obstruction of intraventricular CSF flow and/or blockage of the extraventricular arachnoid granulations.²² In contrast, the role of ChP's immune-secretory functions to the pathogenesis of hydrocephalus remains under-investigated. Interestingly, human PIH and PHH exhibit similar CSF immune cell and cytokine profiles,^{23,24} and CSF neutrophilic pleocytosis can predict the development of PHH.²⁵ These observations suggest an important, yet uncharacterized, role of ChP and CSF inflammation in the pathogenesis of acquired hydrocephalus.

Systemic epithelia respond to pro-inflammatory stimuli by increasing rates of fluid transport²⁶ to clear organisms or tissue debris.^{27–29} However, inappropriately triggered or maladaptively sustained epithelial inflammation can dysregulate ion transport homeostasis. Examples include chemical, autoimmune, and infectious forms of pleuritis, colitis, and pancreatitis.^{29–32} Intraventricular hemorrhage (IVH) is known to cause inflammation-induced ChP CSF hypersecretion in PHH models.^{2,33–36} Nonetheless, the mechanism(s) by which the ChP contributes to PHH and PIH remain obscure, hindering the development of non-surgical treatment strategies.

Lipopolysaccharide (LPS)-expressing bacteria commonly cause PIH.^{37–39} LPS is the canonical pathogen-associated molecular pattern (PAMP) for Toll-like receptor-4 (TLR4).^{40,41} PHH-derived hemoglobin, and possibly other blood products, are TLR4-stimulating damage-associated molecular patterns (DAMPs).^{42,43} We hypothesized that PIH and PHH have convergent pathophysiology that dysregulates ChP immune-secretory function. To test this, we created rat models of PIH and PHH and

conducted a multi-omics investigation of these animals to dissect the physiologic, cellular, and molecular pathology of PIH and PHH. Our results suggest that PIH and PHH are related neuroinflammatory disorders amenable to systemic immunomodulation.

RESULTS

***E. coli* PIH models exhibit ChP-mediated CSF hypersecretion**

Escherichia coli (*E. coli*) CSF infection is a common cause of PIH in resource-limited countries.^{37–39} PIH is characterized by CSF space inflammation and the acute development of ventriculomegaly.¹⁴ To investigate mechanisms of CSF infection on ChP function in PIH, we administered infectious material into the brain by intracerebroventricular (ICV) delivery. Wild-type *E. coli* (*E. coli*^{+LPS}) or *E. coli* genetically engineered to lack LPS in the outer membrane (*E. coli*^{-LPS}, see STAR Methods) were infused in sterile artificial CSF (aCSF) into the lateral ventricles of 8-week-old Wistar rats for 72 h via stereotactically placed infusion pumps (Figure 1A). Control animals received ICV infusions of sterile aCSF. We found that the lateral ventricular volume of animals 72 h after infusion of *E. coli*^{+LPS} was increased ~3-fold relative to control rats (Figures 1B and 1C). The ventriculomegaly in animals subjected to 72 h ICV infusion of LPS alone (10 ng/ μ L in aCSF) resembled *E. coli*^{+LPS}-treated animals (Figures 1B and 1C) and persisted when evaluated 2 weeks after treatment (Figure S1A). These findings suggest ICV-delivered LPS can model the acute development and persistence of ventriculomegaly characteristic of human PIH.

The pathways that regulate CSF homeostasis are poorly understood. Acute ventriculomegaly in PIH could arise from impaired CSF efflux (e.g., due to obstruction of the cerebral aqueduct causing reduced bulk flow or reduced CSF egress via glymphatic and meningeal lymphatic pathways) and/or augmented CSF volume flux via an increase in ChP-dependent CSF production.^{44–46} To examine CSF outflow in our PIH model, we injected the CSF tracer Evans Blue into the lateral ventricles of PIH rats after 72 h of LPS infusion and found that dye distribution was unimpeded through the cerebral aqueduct and 4th ventricle, suggestive of aqueductal patency and preservation of bulk CSF flow (Figure 1D). *In vivo* magnetic resonance imaging (MRI) of control and LPS-treated animals confirmed increased lateral ventricle volume in LPS-treated animals with normal intracranial volume (Figures S1B–S1F), as well as cerebral aqueduct patency (Figures S1G and S1H).

To examine glymphatic function in our PIH model, we performed *in vivo* dynamic contrast-enhanced, T1-weighted MRI after CSF infusion of gadoteric acid (see STAR Methods).^{47–49} The MRI data were analyzed using computational fluid dynamics analysis based on regularized optimal mass theory, which derives metrics describing the transport of the Gd-tagged contrast tracer in the brain.⁵⁰ Quantification of glymphatic v-flux (mm^3) and glymphatic mean tissue speed (mm/s) data revealed no significant differences in brain-wide glymphatic transport between LPS-treated and control animals (Figures S1I–S1K). Notably, this nomenclature refers to 'glymphatic' transport because modeling included both diffusion and advection drivers for solute transport.⁵⁰ However, other perivascular transport models including the "mixing model" and "intramural periarterial drainage" (IPAD) have been proposed and

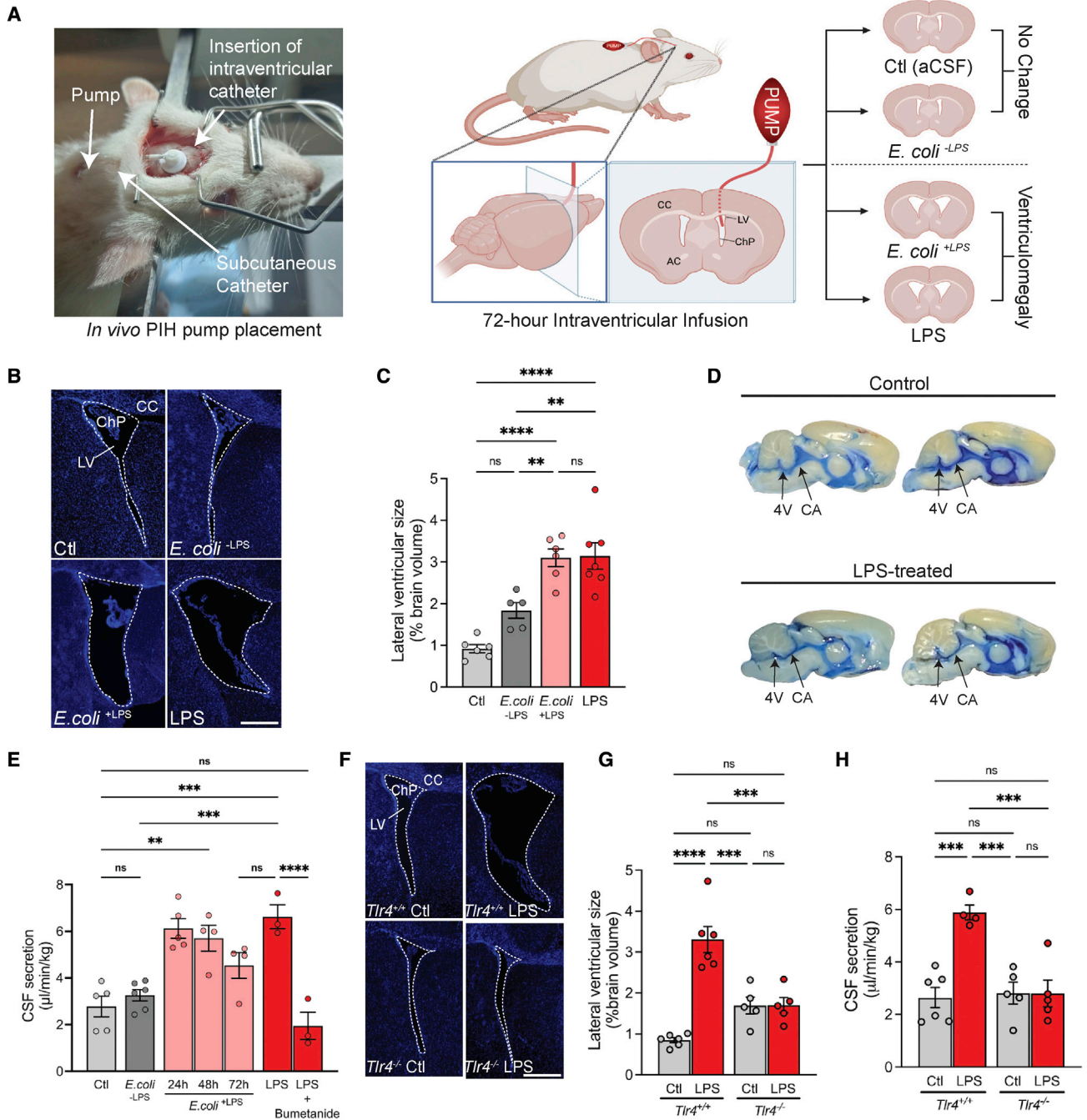


Figure 1. Models of *E. coli* post-infectious hydrocephalus exhibit ChP-mediated CSF hypersecretion

(A) Illustration of two models of post-infectious hydrocephalus (PIH). Insertion of an infusion pump in the lateral ventricle (LV) for *E. coli*^{+LPS}, *E. coli*^{-LPS}, LPS, or artificial CSF (aCSF, Ctl) administration over 72 h. Left, illustration of the subcutaneous pump/catheter and intraventricular catheter placement. Right, schematic demonstrating pump/catheter placement and resulting ventricular changes. CC, corpus callosum; AC, anterior commissure.

(B) Representative immunohistochemical images showing lateral ventricles 72 h after infusion of control, *E. coli*^{+LPS}, *E. coli*^{-LPS}, or LPS (DAPI, blue).

(C) Quantification of lateral ventricular size (% brain volume) after 72 h infusion of aCSF, *E. coli*^{+LPS}, *E. coli*^{-LPS}, or LPS. Volume was calculated from sequential slices through the entire lateral ventricular system (n = 5–7 animals per condition; see STAR Methods).

(D) Ventricular system infusion of Evans blue dye (injected into the LV of Ctl and LPS-treated animals), demonstrating flow through cerebral aqueduct (CA) and fourth ventricle (4V).

(E) Body weight-normalized CSF secretion rates (μL/min/kg) in control (aCSF), *E. coli*^{+LPS} (24, 48, or 72 h), *E. coli*^{-LPS}, LPS (72 h), or LPS + bumetanide (72 h)-treated animals (n = 3–6 animals per condition).

(F) Representative immunohistochemical images of LVs in Ctl vs. LPS-treated *Tlr4*^{+/+} and *Tlr4*^{-/-} rats (DAPI, blue).

(legend continued on next page)

will be considered in future studies.^{51–53} While these results suggest that PIH is associated with the development of acute, communicating ventriculomegaly, as is seen in many human patients,^{54,55} they do not exclude the possibility of alterations in CSF dynamics along other fluid egress pathways.⁵¹

We next directly measured the effect of LPS on the rate of CSF secretion using a validated method in live animals (Figure 1E).^{34,3,56} In this method, mineral oil blocks CSF exit from the third ventricle at the level of the Sylvian aqueduct, preventing contributions to measured CSF secretion from CSF reabsorption pathways distal to this block (Figure S1L). Therefore, this technique measures bona fide lateral ventricle CSF production by the ChP.^{34,3,56} LPS-treated PIH rats exhibited a >2.5-fold increase in CSF secretion relative to controls (Figure 1E). A similar increase in CSF secretion was observed in *E. coli*^{+LPS} hydrocephalic rats but not *E. coli*^{-LPS} control rats (Figure 1E). ICV infusion of aCSF in naive rats at a rate approximating the difference in CSF secretion rates between that of control rats and LPS-induced or *E. coli*^{+LPS} hydrocephalic rats recapitulated the ventriculomegaly observed in both conditions. ICV-delivered bumetanide, an inhibitor of ChP-mediated CSF secretion,^{34,57,58} reduced LPS-induced CSF secretion by >70% (Figure 1E). LPS-induced CSF hypersecretion and ventriculomegaly were attenuated in *Tlr4* knockout rats (*Tlr4*^{-/-})⁵⁹ (Figures 1F–1H). These results suggest that acute ventriculomegaly in PIH models results from an LPS-triggered, TLR4-dependent increase in bumetanide-sensitive CSF secretion from the ChP.

PIH models are associated with robust inflammation of the ChP-CSF interface

To gain molecular insight into the observed ChP-mediated acute CSF hypersecretory response in our models of PIH, we generated transcriptomic and proteomic datasets of micro-dissected lateral ventricle ChP from LPS-induced hydrocephalic and control rats using bulk RNA sequencing (RNA-seq) and quantitative mass spectrometry (Figure 2A). Differential expression analyses of RNA transcripts (Figure 2B, genes) and polypeptides (Figure 2C, proteins) revealed significant differences between LPS-treated and control ChP. Wiki pathway, GO, and Mouse Gene Atlas analyses of the top 100 differentially expressed genes (DEGs) and proteins in PIH vs. control animals revealed enrichment of terms related to innate immunity and inflammation, such as “positive regulation of myeloid leukocyte-mediated immunity” and “microglia pathogen phagocytosis pathway” (Figures 2D and 2E, and Table S1).

We next integrated our bulk multi-omics ChP data with published single-cell and single-nucleus RNA-seq (sc- and snRNA-seq, respectively) of the ChP and brain macrophages.^{6,60} We constructed 21 modules of co-expressed genes from a published scRNA-seq dataset of rodent ChP⁶⁰ (Figure 2F) and found that PIH-associated transcripts converged within a single module associated with monocytes that included dendritic cells

(cDC1s, cDC2s, and migDCs) (module 11, Figure 2G).⁶¹ The most upregulated transcripts and proteins in PIH converged in another immune cell-specific co-expression module (module 17, Figure 2G).⁶¹ Genes in Modules 11 and 17 were both significantly enriched in pathways related to the recruitment of circulating myeloid/lymphoid cells and chemokine/interferon receptor signaling, as well as ChP secretory activity including chloride ion binding and ligand-gated ion channel activity (Figure 2H; Table S1).

Multiple cytokines responsible for inflammatory cell signaling and modulation and multiple chemokines responsible for the recruitment of circulating myeloid and lymphoid cells, were significantly increased in the CSF of LPS-treated animals compared with controls (Figures 2I and S1M). Among these, the most highly upregulated (>30-fold increase, $p = 0.0017$) was C–C motif chemokine ligand 2 (Ccl2). Levels of Ccl5 and C–X–C motif ligand 5 (Cxcl5), tumor necrosis factor- α (Tnf α), Il-1 β , Il-6, and other interferons and interleukins were also significantly increased. These findings indicate that CSF of PIH animals exhibits a pro-inflammatory state absent from normocephalic (non-hydrocephalic) control animals and similarly treated *Tlr4*^{-/-} rats (Figure 2I).

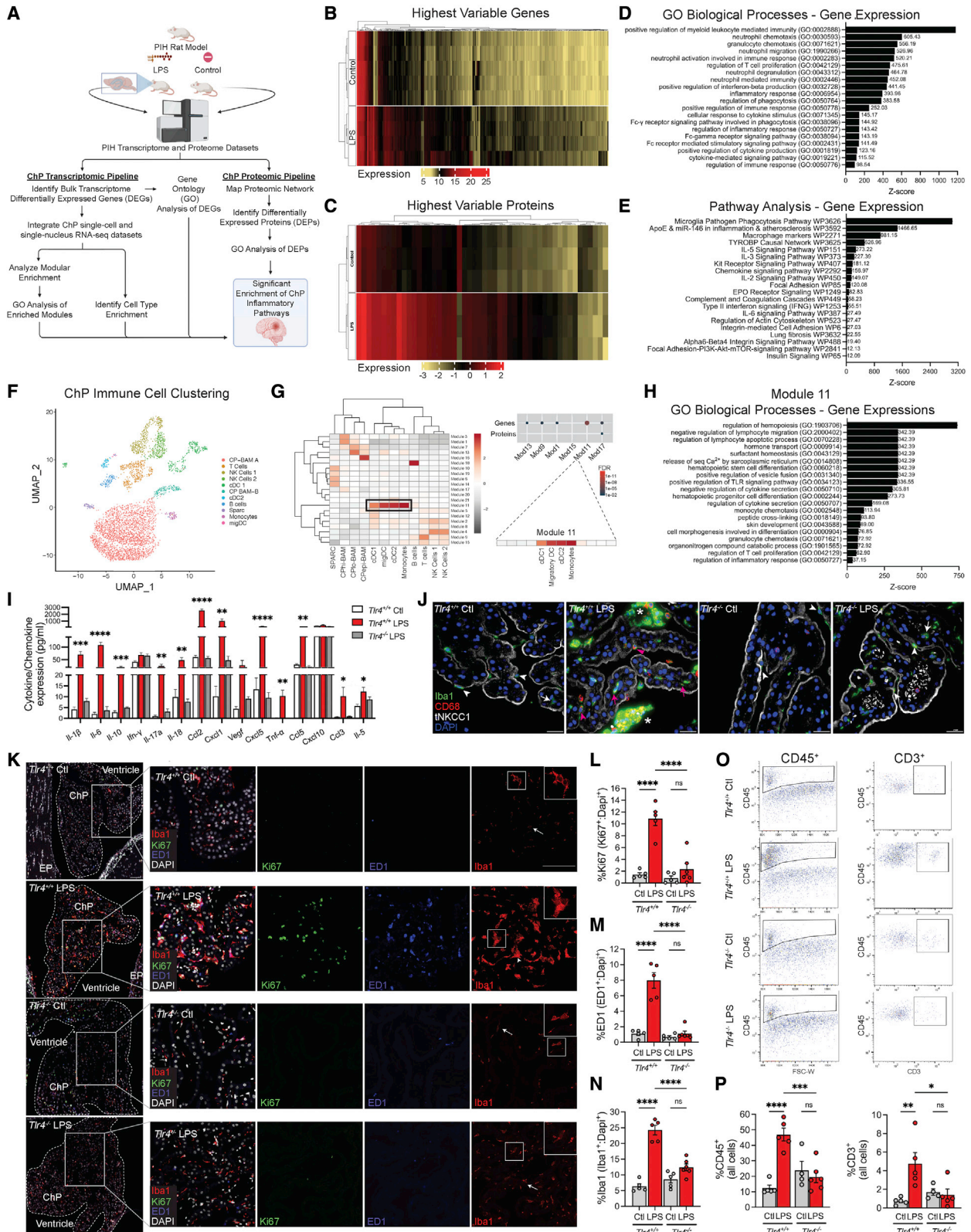
LPS-treated animals demonstrated accumulation and proliferation of Iba1⁺ macrophages at the apical, CSF-facing ChP surface and ChP stromal compartment between the basolateral membrane and endothelium (Figures 2J–2N). Iba1⁺ cells likely include immune cells recruited from the periphery^{3,60} and CNS border-associated macrophages (BAMs), consisting of epilexal (Kolmer) and stromal subtypes. In contrast to their quiescent appearance in controls,⁶⁰ BAMs in PIH rats exhibited amoeboid-like shape, increased circularity (Figures 2J and 2K),⁶² and increased CD68/ED1 positivity (Figures 2K and 2M), all indicative of increased phagocytic activity.⁶³ ChP-associated Iba1⁺ and CD68/ED1⁺ cells were reduced in similarly treated *Tlr4*^{-/-} rats (Figures 2K–2N). In comparison with *E. coli*^{+LPS}-treated animals, the ChP of *E. coli*^{-LPS} rats exhibited a milder inflammatory reaction (Figures S2A–S2C). Similar to human patients with PIH,^{64–67} *E. coli*^{+LPS}-treated animals and, to a lesser extent, *E. coli*^{-LPS} animals also exhibited immune cell activation in the meninges lining the CSF spaces and cortex (Figure S2).

Fluorescence-activated cell sorting (FACS) of micro-dissected, dissociated lateral ventricle ChP labeled with an antibody against CD45, a glycoprotein that marks immune cells of peripheral origin,^{68,69} revealed higher CD45⁺ cell numbers in the ChP of PIH animals than of controls (Figures 2O and 2P, left panels). CD3⁺ T cell number was also increased (Figures 2O and 2P, right panels). LPS-mediated increases in ChP-associated CD45⁺ peripheral immune cells and CD3⁺ T cells were attenuated in *Tlr4*^{-/-} animals (Figures 2O and 2P). These data suggest that PIH is associated with TLR4-dependent accumulation and activation of peripherally derived immune cells and resident BAMs at the ChP that elicit a robust innate immune response characterized by a “CSF cytokine

(G) Quantitation of LV size (% brain volume) in Ctl and LPS-treated *Tlr4*^{+/+} and *Tlr4*^{-/-} rats ($n = 5–6$ animals per condition).

(H) Body weight-normalized CSF secretion rates ($\mu\text{L}/\text{min}/\text{kg}$) of *Tlr4*^{+/+} Ctl, *Tlr4*^{+/+} LPS-treated, *Tlr4*^{-/-} Ctl, and *Tlr4*^{-/-} LPS-treated rats ($n = 4–6$ animals per condition). 2.5 \times mag, scale bars, 0.25 m. Error bars, mean \pm SEM; each symbol represents one animal. * $p < 0.05$, ** $p < 0.01$, *** $p < 0.001$, **** $p < 0.0001$, ns, not significant, by one-way ANOVA.

See also Figure S1.



(legend on next page)

storm.” This is consistent with the ChP-CSF-brain interface inflammation in patients with PIH and other forms of acquired hydrocephalus.^{67,70–72}

SPAK kinase links pro-inflammatory CSF cytokine signaling to ChP-mediated CSF secretion

Analysis of ChP snRNA-seq results⁶ (Figures S3A–S3E) revealed high baseline *Tlr4* expression in ChP-associated macrophages and myeloid lineage immune cells, but scant expression in ChP epithelial cells (Figures S3B–S3D). Expression profiles of immune-related genes in adult ChP epithelial cells further revealed 3 unique subclusters (Table S2), all with low-level *Tlr4* expression. In contrast, even under basal conditions, ChP epithelial cells exhibited significant levels of expression for multiple receptors of pro-inflammatory cytokines upregulated in CSF of PIH animals (Figure 2I) and humans,²⁴ including TNF α , IL1 β , IL6, CCL2, and IFN γ . We hypothesized CSF cytokines elaborated by activated immune cells at the ChP stimulate their receptors on ChP epithelial cells to promote CSF secretion. Consistent with this hypothesis, quantitative real-time PCR of micro-dissected ChP epithelial cells showed higher expression of *Ccr2*, *Relt*, and *Il1r1* in LPS-treated animals than in controls (Figure S3F). The TNF- α receptor *Relt* was also significantly upregulated at the apical membrane in PIH rats, but not in similarly treated *Tlr4*^{-/-} rats (Figures S3G and S3H).

The bumetanide sensitivity of the acute CSF hypersecretory response in PIH implicates the NKCC1 cotransporter in disease pathogenesis. NKCC1 phosphorylation at Thr203, Thr207, and Thr212 by SPAK kinase is required for NKCC1 activity.⁷³ SPAK phosphorylation at Ser373 by WNK1 kinase is required for SPAK kinase activity.⁷⁴ SPAK transduces extracellular stress signals, including NF- κ B-dependent cytokines, into downstream signaling events.⁷⁵ RELT binds SPAK via its C-terminal domain⁷⁶ and TNF- α and IL-1 β stimulate SPAK kinase activity in a TLR4- and NF- κ B-dependent manner to increase intestinal epithelial transport.^{29,75} We hypothesized that SPAK transduces TLR4-dependent pro-inflammatory CSF signals into a ChP epithelial CSF hypersecretory response by increasing NKCC1 phosphorylation.

Consistent with SPAK functioning downstream of TLR4-mediated immune cell activation in a non-cell-autonomous manner,

expression of *Spak* and *Nkcc1* in ChP epithelial cells far exceeded that in other ChP cell types (Figures S3I and S3J). The phosphorylated, activated species of SPAK (pSPAK) and NKCC1 (pNKCC1)^{73,74,77,78} were upregulated at the ChP apical membrane in PIH rats but not in similarly treated *Tlr4*^{-/-} rats (Figures S3K–S3M). While *Spak* knockout had no effect on LPS-induced increases in ChP-associated immune cell infiltration and activation or RELT expression (Figures S4A and S4B),⁷⁹ it prevented the upregulation of pSPAK-pNKCC1 in ChP epithelial cells (Figures S3K–S3M) and attenuated LPS-induced increases in CSF secretion and ventriculomegaly (Figures S3N and S3O). These data suggest that SPAK mediates molecular cross talk between TLR4-dependent ChP immune cell activation and NKCC1-dependent CSF secretion by ChP epithelial cells via cytokine receptor engagement.

SPAK is a regulatory scaffold of a multi-ion transporter complex at the ChP apical membrane

CSF secretion requires the coordinated function of multiple ion and water transport proteins (Figure 3A).^{7,58} NKCC1 is the canonical SPAK target; however, SPAK regulates multiple ion transport proteins.³⁰ To investigate whether other ion transporters are involved in the SPAK-dependent CSF hypersecretory response, we immunoprecipitated SPAK from micro-dissected ChP of adult *Spak*^{-/-} and *Spak*^{+/+} rats, and adult pigs (a model with increased ChP volume per animal) and analyzed the composition of immunoprecipitates using LC-MS-MS (Figure 3B).³⁴ SPAK was the most abundant protein in the purified immune complexes from wild-type pig and rat ChP but absent from *Spak*^{-/-} ChP. NKCC1, the Na⁺/K⁺ ATPase α -1 subunit ATP1a1, the Cl⁻ channel regulatory protein CLIC6, the K⁺ channel KCNJ13, and WNK1 were among the most significantly enriched SPAK-bound proteins in immunoprecipitates from wild-type pig and rat ChP (Figure 3C). These proteins were absent from *Spak*^{-/-} ChP immunoprecipitates. Pull-down experiments validated these findings (Figure 3D).

snRNA-seq analysis of ChP epithelial cells showed high expression of the genes *Wnk1*, *Stk39* (*Spak*), *Slc12a2* (*Nkcc1*), *Atp1a1*, *Kcnj13*, and *Clic6* in each ChP epithelial cell subcluster at levels significantly higher than other ChP cell types

Figure 2. PIH is associated with robust ChP-CSF interface inflammation

- (A) Schematic of integrated multi-omic analysis.
 (B and C) Heatmaps of the most highly differentially expressed ChP genes (B) and proteins (C) from LPS-treated and control rats (n = 3–5 animals per condition).
 (D and E) (D) GO and (E) pathway analysis of DEGs.
 (F and G) (F) uniform manifold approximation and projection (UMAP) clustering of ChP immune cells and (G, left) gene expression module heatmap for individual cell types using a scRNA-seq brain macrophage atlas.⁶⁰
 (G, upper right) Hypergeometric enrichment analysis of LPS-induced DEGs/DEPs in gene co-expression modules (G, lower right); module 11 gene enrichment demonstrating dendritic cell (DC) and monocyte expression.
 (H) Module 11 GO biological process analysis (see also STAR Methods, Table S1*).
 (I) CSF cytokine/chemokine expression (pg/mL) in Ctl and LPS-treated *Tlr4*^{+/+} and *Tlr4*^{-/-} rats (n = 3 animals per condition).
 (J) Representative IHC of Ctl and LPS-treated *Tlr4*^{+/+} and *Tlr4*^{-/-} rat ChP. Iba1⁺ (green)/CD68⁺ (red) cells located apically (epilexus macrophages, white arrowheads) and within stroma/capillaries (white arrows); activated macrophages (pink arrowheads). Apical membrane tNkcc1 (white); nuclei (DAPI, blue); scale bars, 25 μ m.
 (K) Representative merged (left) and magnified merged and single-channel IHC (right) of Ki-67 (green), ED1 (blue), Iba1 (red), and DAPI (white) in Ctl and LPS-treated *Tlr4*^{+/+} and *Tlr4*^{-/-} rat ChP; senescent (arrows) and activated (arrowheads) Iba1⁺ cells. Scale bars, 50 μ m; insets at right, 2 \times enlarged.
 (L–N) Quantitation of (K) showing DAPI-normalized % Iba1⁺ (L), ED1⁺ (M), and Ki67⁺ cells (N) (n = 5–6 animals per condition).
 (O) Scatterplots and (P) quantitation of FACS-isolated CD45⁺ (left) and CD3⁺ ChP cells (right) (n = 4–6 animals per condition). Error bars, mean \pm SEM; each symbol represents one animal. *p < 0.05, **p < 0.01, ***p < 0.001, ****p < 0.0001, ns, not significant, by one-way ANOVA.
 See also Figures S2, S3, and S4.

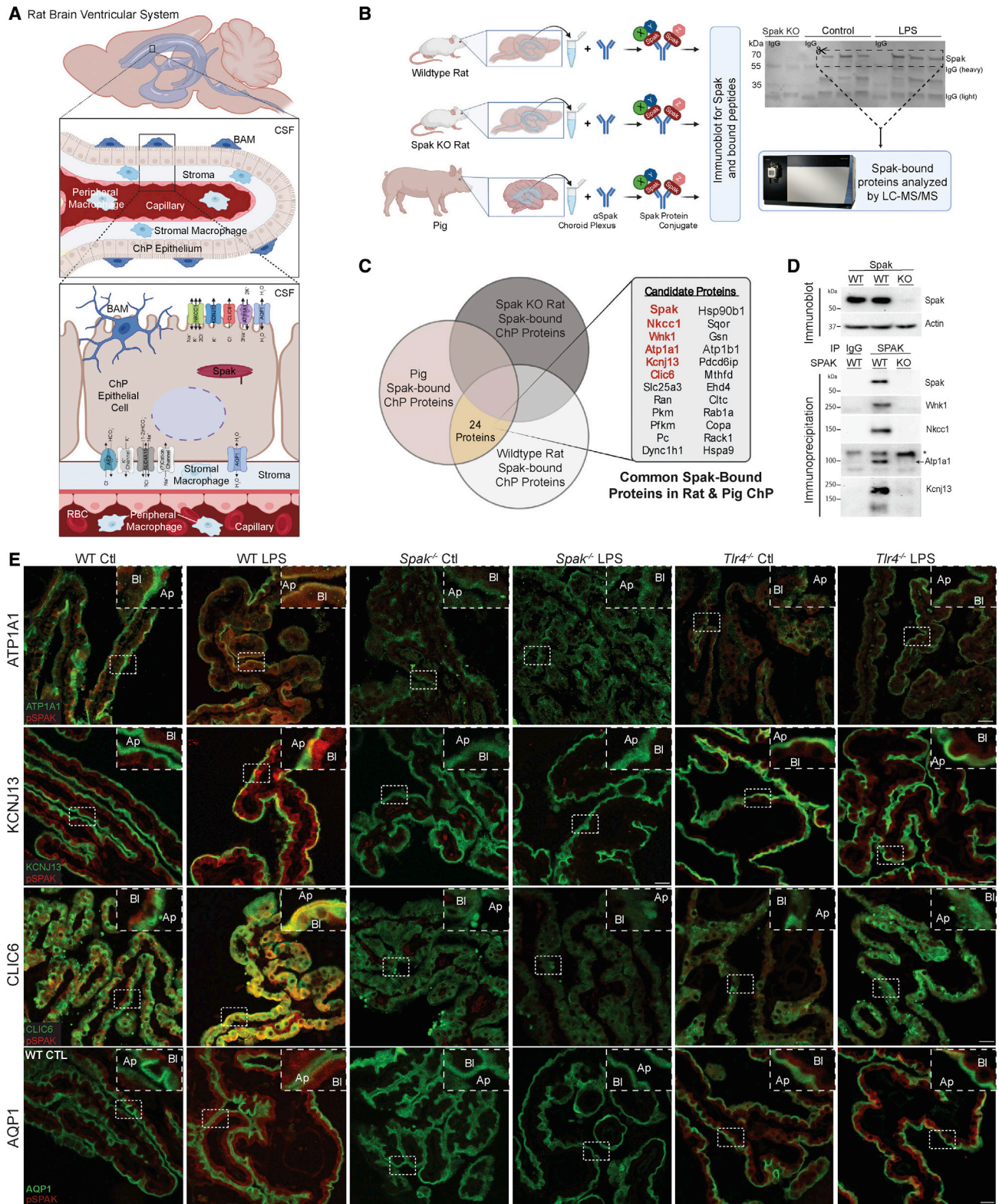


Figure 3. SPAK kinase is a regulatory scaffold for an apically localized multi-ion transporter complex in ChP epithelial cells

(A) Schematic illustrating the rat ventricular system and ChP, highlighting important ion transporters and channels in the apical and basal-lateral membranes of the ChP epithelium. BAM, border-associated macrophage; CSF, cerebrospinal fluid; RBC, red blood cell.

(legend continued on next page)

(Figure S4C). SPAK co-localized with ATP1a1, KCNJ13, and CLIC6 at the ChP apical membrane (Figure 3E). PIH rats had increased *Tlr4*- and *Spak*-dependent colocalization of all three apical transporters, as well as of water channel AQP1, with pSPAK at the ChP apical membrane (Figure 3E). These findings suggest SPAK is both a transducer of immune signals and regulator of ion transporters that are integral to PIH pathophysiology in ChP epithelial cells.

Post-infectious and post-hemorrhagic hydrocephalus share common ChP immune-secretory mechanisms

Intraventricular organisms in PIH and blood products in PHH are similarly associated with CSF immune cell infiltration and cytokine production in patients.^{23,80,81} Bacteria-derived LPS and autologous blood products (e.g. heme) are, respectively, well-known PAMPs and DAMPs for TLR4.^{82,83} We hypothesized that convergent pathophysiology affecting ChP immune-secretory capacity drives the development of acute ventriculomegaly in both PIH and PHH.

To test this, we generated transcriptomic and proteomic datasets of micro-dissected lateral ventricle ChP from a validated rat model of intraventricular hemorrhage (IVH)-induced PHH³⁴ and control rats. The PHH model resembles the PIH model except that blood from the tail vein is harvested and injected directly into the lateral ventricles of the same animal (see STAR Methods). Comparison of the PHH datasets with those from age- and sex-matched PIH rats revealed a striking overlap of the most DEGs and proteins (Figures 4A–4D and Table S3). Highly enriched pathways were related to macrophage-mediated innate immunity, Toll-like receptor signaling, cytokine receptor transduction, and phosphoinositide 3-kinase signaling (Figures 4D–4F and Table S3).

Integrated analysis of the top DEGs and proteins in PHH with scRNA-seq data showed convergence to the same immune cell-specific co-expression module identified in PIH (module 17, Figures 4E and 4F, and Table S3). Similar to PIH rats, PHH rats exhibited increased Iba1⁺, ED1⁺, and Ki67⁺ ChP-associated macrophages (Figures 4G and 4H) and TLR4-dependent increases in CD45⁺ and CD3⁺ T cells at the ChP (Figures 4I and 4J). PHH rats also resembled PIH rats in their >2-fold increased TLR4- and SPAK-dependent ventriculomegaly (Figure 4K); >2-fold increased CSF hypersecretion (Figure 4L); and upregulated pSPAK-pNKCC1 apical membrane ChP expression (Figures 4M–4O). These results show that PIH and PHH share a pathophysiological signature characterized by TLR4-mediated ChP immune cell signaling and SPAK-dependent ChP transepithelial ion transport.

scRNA-seq uncovers molecular cross talk between peripherally derived and resident immune cells and ChP epithelial cells

Given the similarities of the ChP immune response to LPS and IVH, we performed scRNA-seq on microsurgically dissected ChP (Figure 5A) from control, PIH, and PHH animals (Figure 5). We then compared the CD45⁺ and CD45⁻ cell expression profiles (Figures 5B and 5I) using markers (Figures 5C and S5A) defined in the literature.^{6,60} The integrated CD45⁺ dataset consisted of 1,427 control, 3,331 PHH, and 5,529 PIH ChP immune cells. The integrated CD45⁻ dataset consisted of 2,036 control, 718 PHH, and 1,603 PIH ChP non-immune cells. Clustering of CD45⁺ immune cells in control ChP resembled findings previously reported.⁶⁰

Comparing CD45⁺ immune cells in the ChP from PIH and PHH animals demonstrated significantly different immune cell profiles compared with control. However, the inflammatory profiles of the ChP from PIH and PHH animals closely resembled each other (Figures 5B and 5D), with similar increases in macrophage/monocytes and neutrophils (Figures 5B and 5E). Heatmap analysis of the most DEGs in the CD45⁺ dataset showed highly significant overlap for PIH and PHH compared with control (Figure 5D). Interestingly, plasmacytoid DCs (pDCs) and CD4⁺ T cells were particularly increased in PIH (Figures 5B and 5E).

The myeloid cell population was further separated into three main subclusters, in agreement with recently defined markers,⁶⁰ which included stromal BAMs (CP_BAM; C1qa^{hi}Csf1r^{hi}Cd14^{lo}), ChP epiplexus cells (CP_Epi; Sall1⁺), and peripherally derived blood monocytes (Pbm, Cd14^{hi}C1qa^{lo}) (Figures 5F and 5G). The Pbm subcluster was increased in the ChP from PIH and PHH compared with control, reflecting the infiltration of peripheral macrophages (Figures 5F and 5G).⁶⁰ As top markers of the Pbm-2 subcluster included interferon-stimulated genes (such as Irf7, Isg15, Isg20, Ifit2, Ifit3, and Ifitm3), Pbm recruitment is likely a response to upregulated interferon signaling.

The significant increase in Pbm, neutrophils, and pDCs in the ChP of PIH and PHH animals prompted pathway analyses of the top markers for these cell populations (Figures S5B–S5J). Pbm pathway analysis revealed enrichment of pathways related to macrophage function and chemokine/interferon signaling, macrophage and neutrophil chemotaxis and migration, and regulation of dendritic differentiation (Figure S5B). Neutrophil pathway analysis showed enrichment of interferon/chemokine signaling and PI3K-Akt-mTOR signaling pathways (Figure S5D). pDC pathway analysis also identified significant enrichment of TLR signaling, chemokine signaling, and PI3K-Akt-mTOR signaling pathways (Figures S5E and S5F).

(B) (Left) Illustration of SPAK immunoprecipitation and LC-MS/MS analysis of SPAK-interacting proteins detected in the micro-dissected ChP of *Spak*^{+/+} and *Spak*^{-/-} rats, and wild-type pig (see STAR Methods). (Right) Western blot of SPAK, illustrating removal of gel lanes (area of the dashed box) corresponding to SPAK/SPAK-associated proteins for analysis with LC-MS/MS.

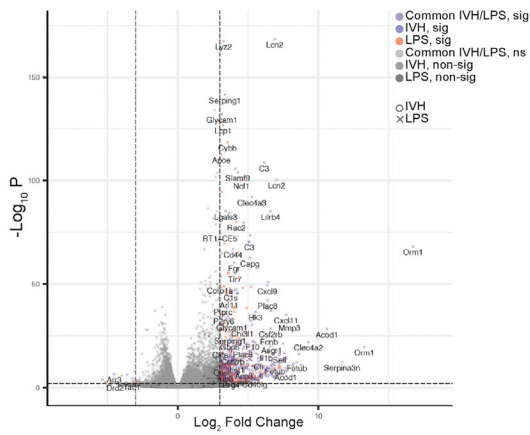
(C) Identification of 24 highly SPAK-bound polypeptides, shared between *Spak*^{+/+} rats and wild-type pig ChP, and absent from immunoprecipitates from lysates of *Spak*^{-/-} rat ChP.

(D) Immunoblot of SPAK (upper blot; beta-actin, loading control) and (lower blots) co-immunoprecipitations of SPAK with LC-MS/MS-identified SPAK-bound proteins WNK1, NKCC1, ATP1A1 (*non-specific band), and KCNJ13 (SDS-resistant tetramer shown) in *Spak*^{+/+} and *Spak*^{-/-} rat ChP.

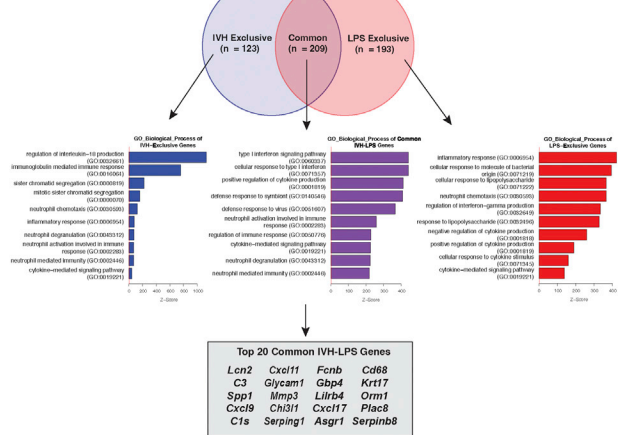
(E) Representative IHC co-staining of pSPAK (red) with ATP1A1 (green, top row), KCNJ13 (green, second row), CLIC6 (green, third row), and AQP1 (green, last row) in ChP of WT, *Spak*^{-/-}, and *Tlr4*^{-/-} animals +/- LPS treatment (n = 6 ChP per genotype, 3 animals per condition). Insets show magnification; Ap, apical membrane; Bl, basolateral membrane of the choroid plexus. 40x, scale bars, 25 μm.

See also Figure S4.

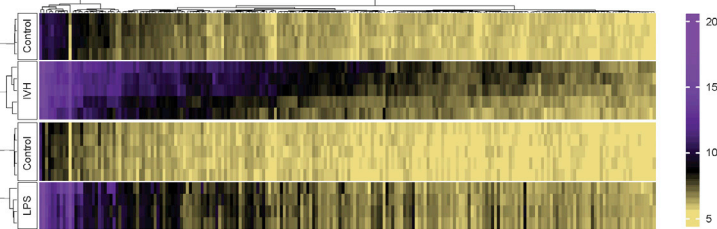
A Highest Variable Genes in PIH and PHH



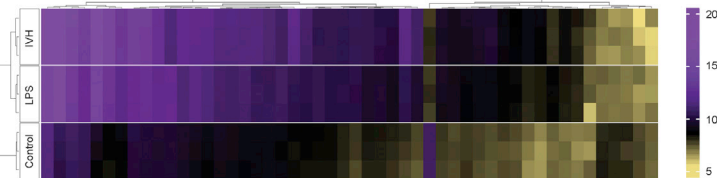
D Genes upregulated in IVH condition and LPS condition



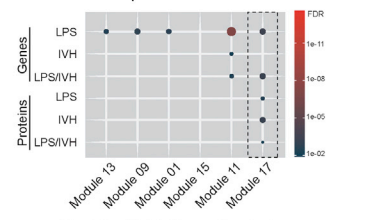
B Common Differentially Expressed Genes (DEGs)



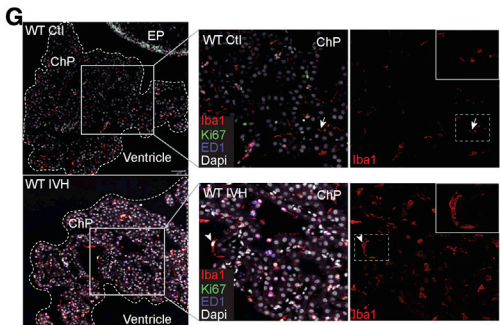
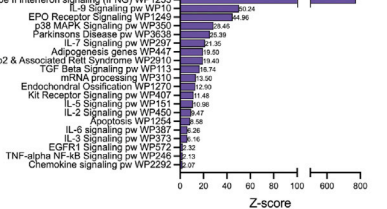
C Common Differentially Expressed Proteins (DEPs)



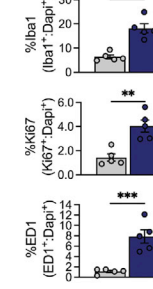
E Co-Expression Modules



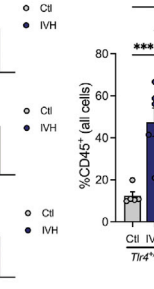
F Module 17: Pathway Analysis



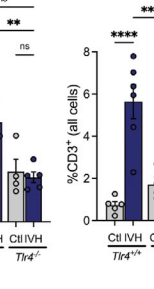
H



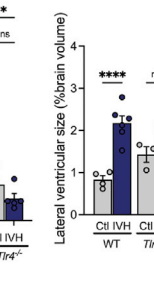
I



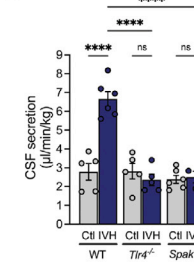
J



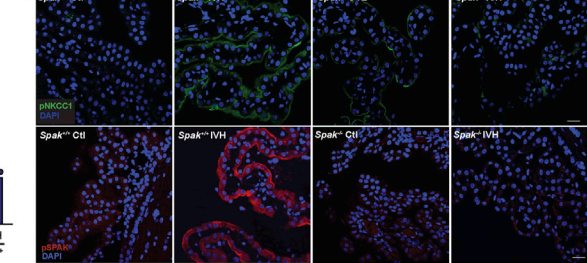
K



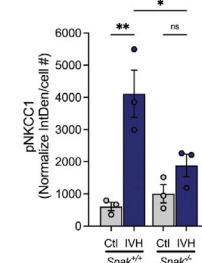
L



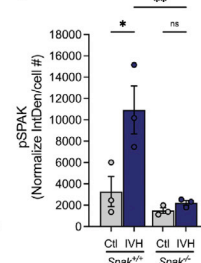
M



N



O



(legend on next page)

The ChP epilexus macrophage (Kolmer cell) cell population transformed similarly in PIH and PHH ChP, compared with controls (Figure 5F). When further subclustered both PIH and PHH exhibited two new populations of ChP-associated Kolmer cells (Figure 5H, blue and green). Pathway analysis revealed enrichment of DNA replication and mitotic division processes in subcluster 1 (Figure S5G), suggesting a subpopulation of replicating Kolmer cells. Pathway analysis for top markers of Kolmer cell subcluster 2 showed enrichment of LPS-mediated signaling, TLR signaling, and chemokine receptor binding, among others (Figure S5H).

Clustering of the ChP CD45⁺ non-immune cell populations demonstrated findings similar to those previously reported (Figure 5I)⁶. Heatmap analysis of the most highly DEGs in the CD45⁺ dataset again revealed substantial overlap for PIH and PHH ChP compared with control ChP (Figure 5J). Subclustering of the epithelial cell (CD45⁺) population uncovered a new ChP epithelial subcluster in PIH and PHH (Figure 5K; subcluster 2), which expressed *Cxcl17*, *Cxcl9*, *Ccl5*, *Il18bp*, and *Irf7* (Table S4, Figure S6). Inflammatory and immune signaling pathways, particularly type I interferon signaling, were enriched in this subcluster in both PIH and PHH (Figures S5I and S5J).

To compare ligand-receptor interactions in control, PIH, and PHH animals, we merged the CD45⁺ and CD45⁺ datasets and applied CellChat,⁸⁴ a scRNA-seq tool used for inferring intercellular communication networks based on the expression of known ligand-receptor pairs in different cell clusters (Figure 6A). Our analysis identified 6 ligand-receptor pathways present in both PIH and PHH ChP that were absent in the control ChP (Figure 6B). Among these, the Osteopontin (*Spp1*) ligand-receptor pathway showed very similar ligand-receptor interaction profiles for both PIH and PHH ChP (Figure 6C). In both groups, the most significant ligand-receptor interactions originated from ChP epilexus macrophages to ChP resident macrophages, monocytes, T cells, B cells, and DCs (Figure 6C). CellChat analysis also identified the ligand-receptor pairs SPP1-CD44 and SPP1-(ITGA4_ITGB1) as the most significant signaling contributors to the *Spp1* communication pathway (Figure 6D). These interactions are known to activate the PI3K-Akt-mTOR signaling pathway.^{85,86}

We next examined ligand-receptor signaling pathways present in all three conditions but independently upregulated in

PIH or PHH ChP compared with the control ChP. Cell-cell communications were very similar for PIH and PHH, showing significant upregulation in inflammatory pathways including MHC-I, CCL, CXCL, and FN1 (Figure 6E). We then compared the ligand-receptor signaling pathways of epithelial and immune cells in PIH and PHH ChP to control ChP. We found inflammatory and cell adhesion pathways such as chemokine (CXCL), Galectin, and Periostin to be activated in both PIH and PHH ChP between epithelial and immune clusters (Figure 6F). The significant CXCL interactions between ChP epithelial and immune cells were mainly sent from epithelial cells to T cells and to dendritic cells for both PIH and PHH compared with control (Figure 6G). Cell-cell communication analysis revealed that ligand-receptor pairs *CXCL11-CXCR3* and *CXCL9-CXCR3* contributed most significantly to the CXCL epithelial-immune cell communication pathway (Figure 6H) in both PIH and PHH, suggesting that ChP epithelial cells play active roles during the inflammatory response.

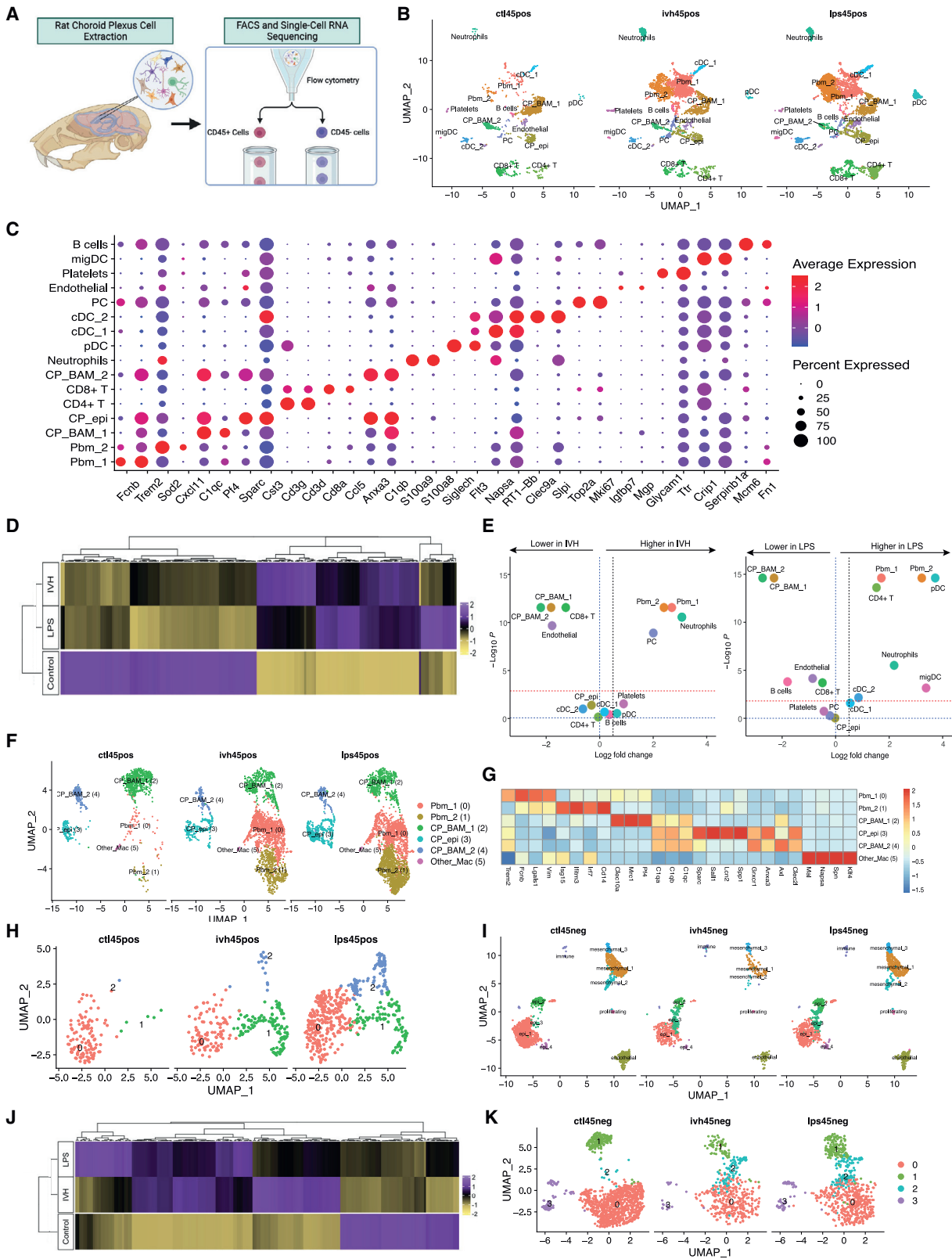
Repurposed systemic immunomodulators treat hydrocephalus by antagonizing ChP-mediated CSF hypersecretion

The importance of highly similar ChP immune-secretory mechanisms to the development of acute ventriculomegaly in PIH and PHH suggests the possibility of shared therapeutic strategies. No clinically approved drugs target TLR4 or SPAK, but multiple agents are in clinical trials or in preclinical development.^{45,87,88}

We therefore mined our ChP -omics data for pathways enriched in both PIH and PHH models that are targeted by clinically approved drugs. Among top-ranked hits, the PI3K-Akt-mTOR signaling pathway (WikiPathways WP2841; Z score 12.13) (Figure 2E) was an appealing target because of its role in both immune cells and SPAK activation.^{89–91} Indeed, the top DEGs and proteins common to PIH and PHH were enriched in multiple phosphatidylinositol pathways, the most significant of which was 1-phosphatidylinositol-3-kinase regulator activity (GO: 0046935; Z score 141.43) (Figures 4D and 4F).⁹² Integration of DEGs with published scRNA-seq data revealed enrichment of the Focal Adhesion-PI3K-Akt-mTOR signaling pathway (WP2841) in co-expression module 11 (Z score 4.16) (Table S1). Consistent with these findings, phosphorylation of S6 ribosomal protein

Figure 4. Post-hemorrhagic and -infectious hydrocephalus models exhibit highly similar ChP immune-secretory pathophysiology

(A–C) (A) Volcano plot and heatmaps of the most highly significant (sig) (B) DEGs and (C) DEPs compared with control from bulk RNA-seq analyses of ChP from Ctl, IVH, and LPS-treated animals (n = 3–5 animals per condition). (D) Venn diagram and GO biological process analysis of genes upregulated in IVH vs. LPS conditions, and those common to both conditions. Outlined box at the bottom shows the top 20 DEGs common to IVH and LPS. (E) Hypergeometric enrichment analysis of gene co-expression modules for DEG/DEPs between LPS and IVH, and shared (LPS/IVH) DEG/DEPs (dashed box highlights shared enrichment in module 17). (F) Module 17 pathway analysis. (G) Representative IHC of Iba1 (red), Ki67 (green), and ED1 (blue) cells in ChP of Ctl and IVH-treated rats (n = 5 animals per condition) (ChP border denoted by dashed white outline; EP, ependyma). Left panel inset, ChP magnification; right panel inset, magnification Iba1⁺ cell (white arrows). Scale bars, 50 μm. (H) Quantitative IHC in (G) showing % (normalized to DAPI) of ED1⁺, Ki67⁺, and Iba1⁺ cells (n = 5 animals per condition). (I and J) FACS quantification of (I) CD45⁺ and (J) CD3⁺ cells in ChP from IVH-treated *Tlr4*^{+/+} and *Tlr4*^{-/-} rats (n = 4–6 animals per condition). (K and L) (K) Quantitation of lateral ventricular size (% brain volume) and (L) body weight-normalized CSF secretion in WT, *Tlr4*^{-/-}, and *Spak*^{-/-} IVH-treated (48 h) rats (n = 3–6 animals per condition). (M) Representative ChP IHC of pNKCC1 (green) and pSPAK (red) expression in Ctl and IVH-treated *Spak*^{+/+} and *Spak*^{-/-} animals. Scale bars, 25 μm. (N–R) Quantitation of (N) pNKCC1 (interval density/cell #) and (R) pSPAK IHC in (O) (n = 6 ChP, 3 animals per condition). Error bars, mean ± SEM; each symbol represents one animal. *p < 0.05, **p < 0.01, ***p < 0.001, ****p < 0.0001, ns, not significant; unpaired t test (K) or one-way ANOVA (L–O, Q, and R). (D–G, abbreviations: pos reg, positive regulation; neg reg, negative regulation; pw, pathway; act, activity; a/o, acting on; FA, focal adhesion; Mφ, macrophage.)



(legend on next page)

(pS6), indicative of mTOR pathway activation, was significantly increased in both ED-1⁺ ChP immune cells and ChP epithelial cells in both PIH and PHH rats, but not in similarly treated *Tlr4*^{-/-} rats (Figure 7A). snRNA-seq analysis revealed high *Mtor* and *Nfkb* gene expression in ChP epithelial cells and hematopoietic cells (Figures 7B, S7A, and S7B). These results suggest that PI3K/Akt/mTOR signaling is a therapeutic target in PHH and PIH.

We tested the hypothesis that systemic treatment with rapamycin, an immunosuppressive mTOR inhibitor, would attenuate the development of acute PIH and PHH by antagonizing inflammation-dependent CSF hypersecretion from ChP epithelial cells. In both PIH and PHH rats intraperitoneal rapamycin (6 mg/kg administered 2–3 h prior to initiating LPS infusion or 2–3 h pre-IVH) decreased upregulated pS6 immunostaining in ChP immune cells and epithelial cells (Figure 7A), reduced numbers of ChP-associated Iba1⁺, ED1⁺, and Ki67⁺ cells (Figures 7C–7F), and attenuated the LPS- and IVH-induced influx of CD45⁺ cells (Figure 7G). Rapamycin also attenuated both LPS- and IVH-induced increases in CSF secretion (Figure 5H), ventriculomegaly (Figures 7I and S7C–S7E), and pSPAK-pNKCC1 abundance at the ChP apical membrane (Figures 7J–7L). Strikingly, delay of rapamycin administration until 3 h after initiating LPS infusion had similar effects, including attenuation of LPS-mediated ventriculomegaly (Figures S7C–S7E) and a decrease in ChP-associated Iba1⁺ and ED1⁺ cells (Figures S7F and S7G). These results suggest that repurposed systemic immunomodulators can ameliorate acute PIH and PHH by antagonizing ChP epithelial cell CSF hypersecretion.

DISCUSSION

Results from multi-modal analysis of CSF dynamics in *E. coli* models of PIH suggest that acute ventriculomegaly results primarily from an LPS-induced increase in ChP-CSF secretion. These data may revise or augment existing paradigms emphasizing obstruction of intraventricular CSF flow. The relevance of these findings is supported by observations in patients that: (1) PIH can develop within hours of CNS infection⁹³ and can precede radiographic evidence of aqueductal obstruction,⁹⁴ (2) destruction of the ChP (with or without an endoscopic third ventriculostomy [ETV]) can effectively treat PIH⁹⁵ and some other

forms of hydrocephalus, and (3) increased CSF secretion can cause hydrocephalus in humans with ChP hyperplasia in the setting of ChP tumors^{96–98} and certain genetic syndromes.^{99–102} Although multiple models of CSF clearance have been proposed (e.g., via vascular basement membranes, the intramural periarterial drainage pathway, perineuronal routes, and skull base lymphatics), their role in hydrocephalus, particularly in chronic hydrocephalus when inflammation-dependent scarring from tissue damage could impact resorptive mechanisms,^{103,104} will be important topics of future investigation.

While we demonstrated that LPS, likely *E. coli*'s most immunogenic virulence factor, is necessary and sufficient to cause CSF hypersecretion and ventriculomegaly in our PIH model, the full immune response to *E. coli* at the ChP-CSF interface likely includes components besides LPS, such as flagellar H-antigens and capsular K-antigens.^{105,106} Indeed, animals treated with LPS-deficient *E. coli*^{-LPS} still exhibit ChP-CSF interface inflammation, albeit less severe than with *E. coli*^{+LPS}, and exhibit a trend toward ventricular enlargement.^{107,108} Moreover, the immune response to *E. coli* and to other infectious agents impacts the meninges and parenchyma.^{107,108} Future studies will explore the involvement of other portals of immune cell entry into the brain and whether PAMPs from other PIH-causing bacteria (e.g., the TLR5 agonist flagellin¹⁰⁹) trigger ChP CSF hypersecretion.

Our data support BAMs on the apical ChP membrane as the “first responders” to microorganisms in the CSF.^{110–113} ChP macrophages express TLRs, which bind PAMPs to activate innate immune responses.^{113,114} Our integrated -omics analysis showed dependence of the acute ChP hypersecretory response in PIH on LPS-induced, TLR4-mediated recruitment of both peripheral blood monocytes and accumulation, proliferation, and activation of resident stromal BAMs (C1qa^{hi}Csf1r^{hi}Cd14^{lo}) and ChP-epilexus macrophages (CP_Epi, Sall1⁺). A similar TLR4-dependent immune cell response was triggered in PHH by intraventricular hemorrhage-derived DAMPs such as heme.^{43,82,115,116} Notably, ChP macrophage depletion attenuates ventriculomegaly following ICV-injection of the pro-inflammatory blood product peroxiredoxin-2.¹¹⁷ These data show the remarkable similarity of the innate immune cell responses to CNS infection and to hemorrhage, and highlight the ChP as a dynamic, cellular heterogeneous tissue with highly regulated immune-secretory capacity.

Figure 5. scRNA-seq uncovers cross talk between peripheral and resident immune cells and epithelial cells at the ChP

- (A) Schematic illustrating the scRNA experimental design and downstream analyses.
- (B) UMAP clustering of ChP CD45⁺ cells across control, IVH-treated and LPS-treated conditions, colored by cell type.
- (C) DotPlot showing gene expression signatures of CD45⁺ cell clusters, with dot size representing the percentage of cells expressing the gene and the color representing average expression within a cluster.
- (D) Heatmap of the top DEGs comparing ChP CD45⁺ cell expression profiles from Ctl, IVH, and LPS-treated animals.
- (E) Volcano plots depicting differences of cluster abundance in IVH-treated and LPS-treated ChP CD45⁺ cells compared with control plotting fold change (log₂) against p value (–log₁₀) based on beta-binomial regression. The red horizontal dashed line indicates the significance threshold.
- (F) UMAP of ChP myeloid cell clusters, including peripheral blood macrophages, CP stromal macrophages, and CP epilexus macrophages, colored by cell type.
- (G) Heatmap of the top DEGs for myeloid subclusters.
- (H) UMAP of ChP epilexus macrophage subclusters, colored by group, showing transformed and proliferating epilexus macrophages in control, IVH, and LPS conditions.
- (I) UMAP clustering of ChP CD45[–] cells across IVH-treated, LPS-treated, and control conditions, colored by cell type.
- (J) Heatmap of top DEGs comparing ChP CD45[–] epithelial cell expression profiles from Ctl, IVH, and LPS-treated animals.
- (K) UMAP of ChP epithelial subclusters, colored by group.

See also Figures S5 and S6.

We found acute PIH and PHH are both characterized by a CSF “cytokine storm” analogous to sepsis-associated elevations of blood circulating cytokines in the settings of systemic infection or widespread tissue damage.^{118,119} These observations correspond to cytokine and immune cell responses in human CSF stimulated by intraventricular infection and hemorrhage.^{23,80,81} CSF cytokines likely engage their cognate receptors on ChP epithelial cells to modulate epithelial cell function. Among upregulated cytokines, CCL2 and its ChP epithelial cell receptor CCR2 recruit macrophages to the ChP-CSF interface in response to maternal immune activation.⁸ The ChP’s ability to detect infection or tissue damage and initiate a counter-response may also be an Achilles’s heel that renders the brain susceptible to attack by circulating immune cells in multiple sclerosis and other diseases.^{12,120,121}

SPAK kinase links ChP immune cell signaling and epithelial function via its interactions with upstream cytokine receptors and downstream ion transport proteins.⁷⁵ The TNF- α receptor RELT binds SPAK to regulate the innate immune system⁷⁶ and increases epithelial transport in experimental inflammatory bowel disease.^{75,122,123} SPAK is a master regulator of the SLC12 family cation-Cl⁻ cotransporters such as NKCC1.¹²⁴ SPAK phospho-activation in the ChP, triggered by LPS or IVH, leads to increased ChP CSF production in part by phosphorylating and thereby stimulating NKCC1. These data accord with the importance of bumetanide-sensitive (NKCC1-mediated) ChP transport for CSF production in humans,¹²⁵ dogs,⁵⁷ rats,³⁴ and mice¹²⁶ and are consistent with the finding that patients with loss-of-function NKCC1 mutations exhibit decreased epithelial secretion and “slit-ventricle” brain morphology indicative of decreased intraventricular CSF volumes.¹²⁷

NKCC1 operates close to its equilibrium electrochemical potential in the ChP as in other epithelia. This suggests the capacity for regulated, bidirectional net ion and fluid transport across the ChP^{77,126} and might account for reported differences in the vector of NKCC1-mediated net ion transport (inward vs. outward), and in net CSF secretion and/or CSF clearance in various developmental¹²⁸ and/or disease contexts.³⁴ We showed SPAK binds not only NKCC1^{124,129} but also other ion transport proteins implicated in CSF secretion including ATP1a1. We predict that SPAK

functions as a regulatory scaffold that senses extracellular and/or intracellular signals (e.g., changes in CSF ionic composition) and then transduces these signals into phosphorylation events to coordinate the activities of an ensemble of associated ion transport proteins.

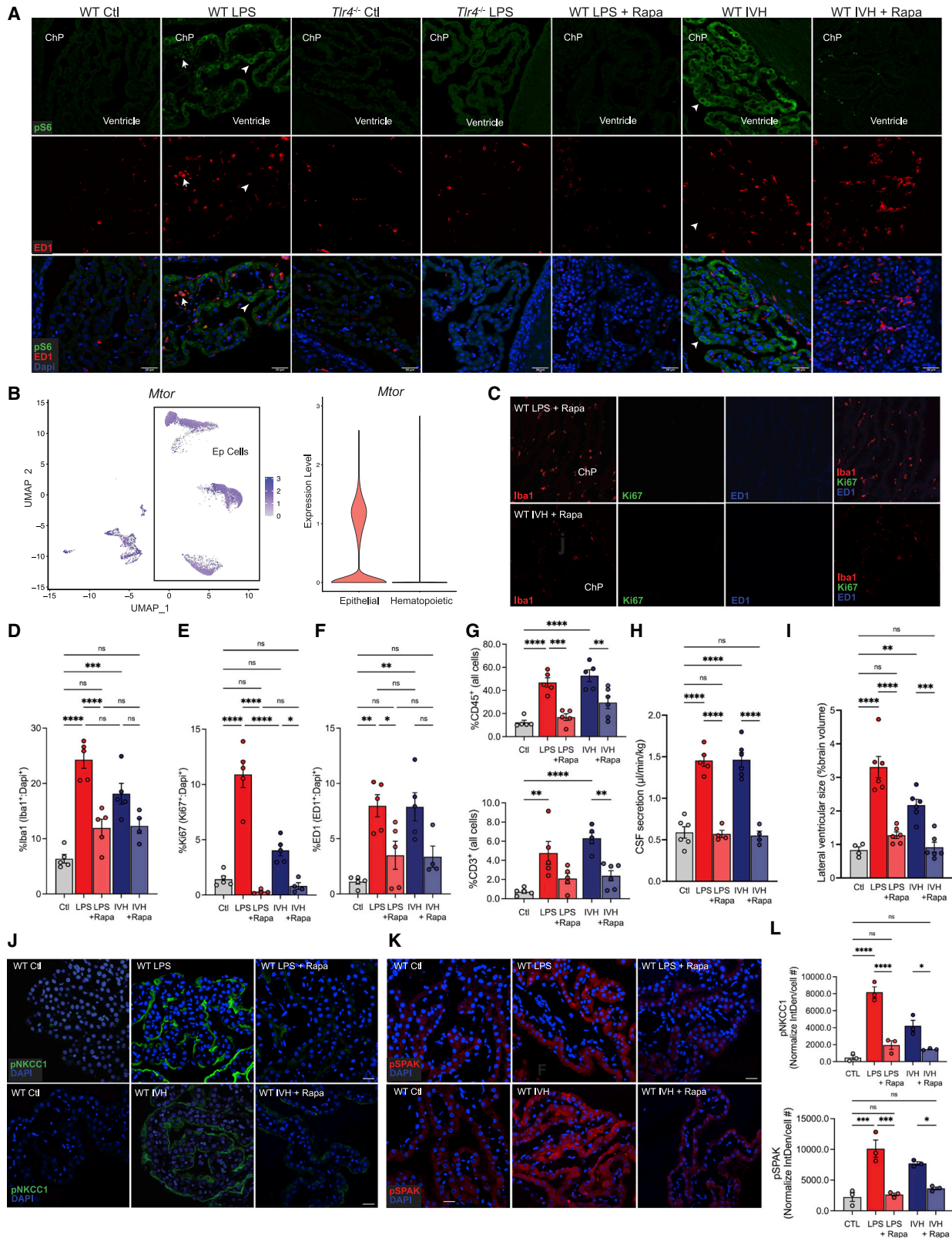
Drugs targeting TLR4 or SPAK have not been clinically approved.^{45,130,131} Our -omics data converged upon PI3K-Akt-mTOR signaling as important for ChP immune-secretory mechanisms in both PIH and PHH, consistent with this pathway’s contributions to immune cell and epithelial cell homeostasis,¹³² and to TLR4^{133,134} and SPAK signaling.^{90,135} “Rapalog” mTOR inhibitors are approved for systemic treatment of allograft rejection and for adjunct treatment of subependymal cell astrocytomas (SEGA).^{136,137} The immunosuppressive effects of mTOR inhibition likely prevail over other growth-mediated pathways in rapamycin’s therapeutic effect on our acquired hydrocephalus models. Other potential beneficial effects of rapamycin may include its autophagy-inducing effects in brain microglia¹³⁸ and inhibition of hypoxia-inducible factor 1 α .¹³⁹ The clinical utility of rapamycin will be better assessed by testing later time points of administration. Repurposed drugs modulating ChP immune-secretory function might be a viable non-surgical treatment strategy for multiple forms of acquired hydrocephalus and for other neuroimmune brain disorders associated with ChP dysfunction.

Limitations of the study

Limitations of our study include our reliance on the rat as a model organism, chosen for its amenability to *in vivo* measurements of CSF secretion and for its CSF volume higher than that of mouse. Future development of non-invasive, imaging-based assays to measure ChP-mediated CSF production, and of ChP-specific gene targeting approaches should overcome present limitations of our direct surgical CSF secretion assay and of current indirect methods to interrogate *in vivo* transporter activity. Additional limitations include the lack of correlative scRNA-seq analysis of CSF from PIH and PHH patients, and lack of clinical data testing efficacy of rapamycin and other immunomodulators as treatments for hydrocephalus. The latter could be studied in patients with high-grade aneurysm rupture complicated by intraventricular hemorrhage and PHH, all

Figure 6. scRNA-seq CellChat analysis reveals ligand-receptor pairs enabling ChP immune-epithelial cell communication

- (A) Schematic illustrating CellChat downstream analyses.
 (B) Identification of 6 ligand-receptor pathways shared between IVH-treated and LPS-treated rats and absent in control.
 (C) Circle plot depicting ligand-receptor interactions of the SPP1 pathway in IVH-treated and LPS-treated ChP. Edge width represents communication probability.
 (D) Bubble plot showing significant ligand-receptor interactions for the SPP1 pathway in IVH-treated and LPS-treated ChP (no significant interactions were found for control). x axis shows the cell groups associated with the interactions. y axis shows the ligand-receptor pairs. Dot color reflects communication probabilities and dot size represents computed p values. Empty space means zero communication probability. p values reflect a one-sided permutation test.
 (E) Upregulated ligand-receptor pairs for IVH-treated and LPS-treated ChP compared with control, showing significant overlap of upregulated pathways in IVH and LPS, with increased signal in SEMA, CD45, MHC-I, FN1, CXCL, CCL, and COMPLEMENT pathway ligand-receptor pairs for both conditions. Dot color reflects communication probabilities, and dot size represents computed p values (from a one-sided permutation test).
 (F) Significant signaling pathways ranked based on differences in the overall information flow within the inferred networks between epithelial and CD45⁺ cells, comparing LPS (left) and IVH conditions (right) to control. The overall information flow of a signaling network is calculated by summarizing all communication probabilities in that network. Rows with high blue-to-red ratio indicate higher ligand-receptor pathway activity for IVH or LPS conditions.
 (G) Circle plot comparing CXCL pathway ligand-receptor interactions among control, IVH-treated, and LPS-treated ChP epithelial and CD45⁺ cell groups. Edge width represents communication probability.
 (H) Comparison of control, IVH, and LPS bubble plots showing significant ligand-receptor interactions between epithelial and CD45⁺ cells for the CXCL pathway. x axis shows the cell groups associated with the interactions. y axis shows the ligand-receptor pairs. Dot color reflects communication probabilities, and dot size represents computed p values (from a one-sided permutation test). Empty space means zero communication probability.



(legend on next page)

currently managed with indwelling intraventricular drains and intermittent imaging.

STAR★METHODS

Detailed methods are provided in the online version of this paper and include the following:

- **KEY RESOURCES TABLE**
- **RESOURCE AVAILABILITY**
 - Lead contact
 - Materials availability
 - Data and code availability
- **EXPERIMENTAL MODEL AND SUBJECT DETAILS**
 - Rodent Model
 - Porcine Model
- **METHOD DETAILS**
 - Model of post-hemorrhagic hydrocephalus
 - Model of post-infectious hydrocephalus
 - ICV-infusion of *E. coli*
 - Measurement of CSF production rates
 - Ventricular volume analysis
 - ICV bumetanide delivery
 - Systemic rapamycin administration
 - ICV injection of Evans Blue Dye
 - CSF cytokine collection
 - Rodent choroid plexus epithelium harvesting
 - Immunohistochemistry
 - Tissue dissociation and flow cytometry
 - Antibodies for western blots
 - Buffers for Western blots
 - Immunoblot and immunoprecipitation analyses
 - qPCR analysis
 - Bulk RNAseq
 - scRNAseq sample preparation
 - Anesthesia and CM catheter placement
 - Magnetic resonance imaging (MRI)
 - Porcine choroid plexus epithelium harvesting
 - Mass-spectrometry (MS) proteomics
 - SPAK Immunoprecipitation for LC-MS/MS
- **QUANTIFICATION AND STATISTICAL ANALYSIS**
 - Data analysis
 - snRNA-seq rat ChP data analysis
 - PIH and PHH rat ChP scRNAseq datasets

- ScRNA-seq mouse ChP immune cell data analysis
- Gene co-expression network creation
- Hypergeometric enrichment test analysis
- Cluster abundance analysis
- Gene Ontology enrichment analysis
- MRI data analysis

SUPPLEMENTAL INFORMATION

Supplemental information can be found online at <https://doi.org/10.1016/j.cell.2023.01.017>.

ACKNOWLEDGMENTS

K.T.K. is supported by grants from the NIH (1R01NS109358-01; 1R01NS111029-01A1), Rudi Schulte Organization, Hydrocephalus Association, Simons Foundation, and March of Dimes. The funders had no role in study design, data collection and analysis, decision to publish, or preparation of the manuscript.

AUTHOR CONTRIBUTIONS

Conceptualization, S.M.R., B.C.R., J.K.K., and K.T.K.; methodology, S.M.R., J.K.K., J.M.S., and K.T.K.; formal analysis, S.M.R., B.C.R., J.K.K., E.K., M.S.M., X.Z., H.B., and T.T.L.; investigation, S.M.R., B.C.R., J.K.K., A.M., G.A., T.D., A.S., P.Q.D., A.G., J.Z., C.N.-W., R.W., A.T., S.K., X.C., and P.F.; writing – original draft, S.M.R., B.C.R., and K.T.K.; writing – reviewing & editing, S.M.R., B.C.R., A.J.K., L.T.H., W.B., M.L.D., D.P.S., K.M., H.B., D.D.L., S.J.S., B.S.C., M.G., J.M.S., R.P.L., S.L.A., E.D., and K.T.K.; visualization, S.M.R., E.K., and G.A.; project administration, S.M.R., A.M., and K.T.K.; funding acquisition, K.T.K.

DECLARATION OF INTERESTS

The authors declare no competing interests.

INCLUSION AND DIVERSITY

We support the inclusive, diverse, and equitable conduct of research.

Received: January 1, 2022

Revised: September 26, 2022

Accepted: January 12, 2023

Published: February 16, 2023

REFERENCES

1. Perez-Riverol, Y., Csordas, A., Bai, J., Bernal-Llinares, M., Hewapathirana, S., Kundu, D.J., Inuganti, A., Griss, J., Mayer, G., Eisenacher, M., et al. (2019). The PRIDE database and related tools and resources in

Figure 7. Repurposed systemic immunomodulators treat hydrocephalus by antagonizing ChP-mediated CSF hypersecretion

(A) Representative IHC of pS6 (green) and ED1 (red) in ChP-associated immune cells (arrows) and epithelial cells (arrowheads) in WT and *Tlr4*^{-/-} animals +/- LPS, and WT LPS and IVH conditions +/- rapamycin (Rapa) (n = 5). Scale bars, 30 μm. DAPI, blue.

(B) snRNA-seq analysis (left panel) and violin plot (right) demonstrating *Mtor* in ChP epithelial (Ep) cells and ChP-associated hematopoietic cells (epithelial, avg Log₂FC = 7.88e-2, p = 1.23e-17).

(C) Representative IHC of Iba1 (red), Ki67 (red), and ED1 (blue) expression in the ChP of WT rats treated with LPS or IVH, in the presence of Rapa.

(D–F) Quantitative IHC of the ChP immune response in (C) in WT LPS and IVH-treated animals ± Rapa. Graphs represent DAPI-normalized % of cells identified as (D) Iba1⁺, (E) Ki67⁺, and (F) ED1⁺ in Ctl, LPS, LPS + Rapa, IVH, and IVH + Rapa-treated animals (n = 4–6).

(G) Quantitation of FACS-isolated CD45⁺ and CD3⁺ cells in Ctl, LPS, LPS+Rapa, IVH, and IVH+Rapa-treated rats (n = 5–6).

(H–K) (H) Weight-normalized CSF secretion and (I) lateral ventricular size (% brain volume) in Ctl, LPS, LPS + Rapa, IVH, and IVH + Rapa-treated animals (n = 4–6).

Representative IHC of (J) pNKCC1 and (K) pSPAK expression in WT Ctl, LPS ±Rapa, and IVH ±Rapa. Scale bars, 25 μm.

(L) Quantitation (Interval Density/cell #) of pNKCC1 and pSPAK IHC in (J) and (K), respectively (n = 6 ChP, 3 animals). Error bars, mean ± SEM; each symbol represents one animal. *p < 0.05, **p < 0.01, ***p < 0.001, ****p < 0.0001, ns, not significant; one-way ANOVA.

See also Figure S7.

- 2019: improving support for quantification data. *Nucleic Acids Res.* 47, D442–D450. <https://doi.org/10.1093/nar/gky1106>.
2. Simard, P.F., Tosun, C., Melnichenko, L., Ivanova, S., Gerzanich, V., and Simard, J.M. (2011). Inflammation of the choroid plexus and ependymal layer of the ventricle following intraventricular hemorrhage. *Transl. Stroke Res.* 2, 227–231. <https://doi.org/10.1007/s12975-011-0070-8>.
 3. Karimy, J.K., Kahle, K.T., Kurland, D.B., Yu, E., Gerzanich, V., and Simard, J.M. (2015). A novel method to study cerebrospinal fluid dynamics in rats. *J. Neurosci. Methods* 241, 78–84. <https://doi.org/10.1016/j.jneumeth.2014.12.015>.
 4. Lodhia, K.R., Shakui, P., and Keep, R.F. (2006). Hydrocephalus in a rat model of intraventricular hemorrhage. *Acta Neurochir. Suppl.* 96, 207–211. https://doi.org/10.1007/3-211-30714-1_45.
 5. Cui, J., Xu, H., and Lehtinen, M.K. (2021). Macrophages on the margin: choroid plexus immune responses. *Trends Neurosci.* 44, 864–875. <https://doi.org/10.1016/j.tins.2021.07.002>.
 6. Dani, N., Herbst, R.H., McCabe, C., Green, G.S., Kaiser, K., Head, J.P., Cui, J., Shipley, F.B., Jang, A., Dionne, D., et al. (2021). A cellular and spatial map of the choroid plexus across brain ventricles and ages. *Cell* 184, 3056–3074.e21. <https://doi.org/10.1016/j.cell.2021.04.003>.
 7. Damkier, H.H., Brown, P.D., and Praetorius, J. (2013). Cerebrospinal fluid secretion by the choroid plexus. *Physiol. Rev.* 93, 1847–1892. <https://doi.org/10.1152/physrev.00004.2013>.
 8. Cui, J., Shipley, F.B., Shannon, M.L., Alturkistani, O., Dani, N., Webb, M.D., Sugden, A.U., Andermann, M.L., and Lehtinen, M.K. (2020). Inflammation of the embryonic choroid Plexus Barrier following Maternal Immune Activation. *Dev. Cell* 55, 617–628.e6. <https://doi.org/10.1016/j.devcel.2020.09.020>.
 9. Engelhardt, B., Vajkoczy, P., and Weller, R.O. (2017). The movers and shapers in immune privilege of the CNS. *Nat. Immunol.* 18, 123–131. <https://doi.org/10.1038/ni.3666>.
 10. Reboldi, A., Coisne, C., Baumjohann, D., Benvenuto, F., Bottinelli, D., Lira, S., Uccelli, A., Lanzavecchia, A., Engelhardt, B., and Sallusto, F. (2009). C-C chemokine receptor 6-regulated entry of TH-17 cells into the CNS through the choroid plexus is required for the initiation of EAE. *Nat. Immunol.* 10, 514–523. <https://doi.org/10.1038/ni.1716>.
 11. Schwartz, M., and Baruch, K. (2014). The resolution of neuroinflammation in neurodegeneration: leukocyte recruitment via the choroid plexus. *EMBO J.* 33, 7–22. <https://doi.org/10.1002/emboj.201386609>.
 12. Rodríguez-Lorenzo, S., Konings, J., van der Pol, S., Kamermans, A., Amor, S., van Horsen, J., Witte, M.E., Kooij, G., and de Vries, H.E. (2020). Inflammation of the choroid plexus in progressive multiple sclerosis: accumulation of granulocytes and T cells. *Acta Neuropathol. Commun.* 8, 9. <https://doi.org/10.1186/s40478-020-0885-1>.
 13. Coulter, I.C., Dewan, M.C., Tailor, J., Ibrahim, G.M., and Kulkarni, A.V. (2021). Endoscopic third ventriculostomy and choroid plexus cauterization (ETV/CPC) for hydrocephalus of infancy: a technical review. *Childs Nerv. Syst.* 37, 3509–3519. <https://doi.org/10.1007/s00381-021-05209-5>.
 14. Kahle, K.T., Kulkarni, A.V., Limbrick, D.D., Jr., and Warf, B.C. (2016). Hydrocephalus in children. *Lancet* 387, 788–799. [https://doi.org/10.1016/S0140-6736\(15\)60694-8](https://doi.org/10.1016/S0140-6736(15)60694-8).
 15. Warf, B.C. (2005). Comparison of endoscopic third ventriculostomy alone and combined with choroid plexus cauterization in infants younger than 1 year of age: a prospective study in 550 African children. *J. Neurosurg.* 103, 475–481. Supplement. <https://doi.org/10.3171/ped.2005.103.6.0475>.
 16. Anderson, I.A., Saukila, L.F., Robins, J.M.W., Akhunbay-Fudge, C.Y., Goodden, J.R., Tyagi, A.K., Phillips, N., and Chumas, P.D. (2018). Factors associated with 30-day ventriculoperitoneal shunt failure in pediatric and adult patients. *J. Neurosurg.* 130, 145–153. <https://doi.org/10.3171/2017.8.JNS17399>.
 17. Kulkarni, A.V., Riva-Cambrin, J., Butler, J., Browd, S.R., Drake, J.M., Holubkov, R., Kestle, J.R., Limbrick, D.D., Simon, T.D., Tamber, M.S., et al. (2013). Outcomes of CSF shunting in children: comparison of Hydrocephalus Clinical Research Network cohort with historical controls: clinical article. *J. Neurosurg. Pediatr.* 12, 334–338. <https://doi.org/10.3171/2013.7.PEDS12637>.
 18. Karimy, J.K., Reeves, B.C., Damisah, E., Duy, P.Q., Antwi, P., David, W., Wang, K., Schiff, S.J., Limbrick, D.D., Jr., Alper, S.L., et al. (2020). Inflammation in acquired hydrocephalus: pathogenic mechanisms and therapeutic targets. *Nat. Rev. Neurol.* 16, 285–296. <https://doi.org/10.1038/s41582-020-0321-y>.
 19. Fleischer, V., Gonzalez-Escamilla, G., Ciolac, D., Albrecht, P., Küry, P., Gruchot, J., Dietrich, M., Hecker, C., Müntefering, T., Bock, S., et al. (2021). Translational value of choroid plexus imaging for tracking neuroinflammation in mice and humans. *Proc. Natl. Acad. Sci. USA* 118. <https://doi.org/10.1073/pnas.2025000118>.
 20. Shipley, F.B., Dani, N., Xu, H., Deister, C., Cui, J., Head, J.P., Sadegh, C., Fame, R.M., Shannon, M.L., Flores, V.I., et al. (2020). Tracking calcium dynamics and immune surveillance at the choroid plexus blood-cerebrospinal fluid interface. *Neuron* 108, 623–639.e10. <https://doi.org/10.1016/j.neuron.2020.08.024>.
 21. Müller, J., Sinnecker, T., Wendebourg, M.J., Schläger, R., Kuhle, J., Schädelin, S., Benkert, P., Derfuss, T., Cattin, P., Jud, C., et al. (2022). Choroid plexus volume in multiple sclerosis vs neuromyelitis optica spectrum disorder: A retrospective, cross-sectional analysis. *Neurol. Neuroimmunol. Neuroinflamm.* 9, e1147. <https://doi.org/10.1212/NXI.0000000000001147>.
 22. Symss, N.P., and Oi, S. (2013). Theories of cerebrospinal fluid dynamics and hydrocephalus: historical trend. *J. Neurosurg. Pediatr.* 11, 170–177. <https://doi.org/10.3171/2012.3.PEDS0934>.
 23. Habiyaemye, G., Morales, D.M., Morgan, C.D., McAllister, J.P., Creve-Coeur, T.S., Han, R.H., Gabir, M., Baksh, B., Mercer, D., and Limbrick, D.D., Jr. (2017). Chemokine and cytokine levels in the lumbar cerebrospinal fluid of preterm infants with post-hemorrhagic hydrocephalus. *Fluids Barriers CNS* 14, 35. <https://doi.org/10.1186/s12987-017-0083-0>.
 24. Lepennetier, G., Hracsko, Z., Unger, M., Van Griensven, M., Grummel, V., Krumbholz, M., Berthele, A., Hemmer, B., and Kowarik, M.C. (2019). Cytokine and immune cell profiling in the cerebrospinal fluid of patients with neuro-inflammatory diseases. *J. Neuroinflammation* 16, 219. <https://doi.org/10.1186/s12974-019-1601-6>.
 25. Cuoco, J.A., Williams, E.L., Klein, B.J., Benko, M.J., Darden, J.A., Olan-sunkanmi, A.L., Witcher, M.R., Rogers, C.M., Marvin, E.A., Patel, B.M., and Entwistle, J.J. (2021). Neutrophil count on admission predicts acute symptomatic hydrocephalus after aneurysmal subarachnoid hemorrhage. *World Neurosurg.* 156, e338–e344. <https://doi.org/10.1016/j.wneu.2021.09.059>.
 26. Berkes, J., Viswanathan, V.K., Savkovic, S.D., and Hecht, G. (2003). Intestinal epithelial responses to enteric pathogens: effects on the tight junction barrier, ion transport, and inflammation. *Gut* 52, 439–451. <https://doi.org/10.1136/gut.52.3.439>.
 27. Doyle, W.J., Skoner, D.P., Hayden, F., Buchman, C.A., Seroky, J.T., and Fireman, P. (1994). Nasal and otologic effects of experimental influenza A virus infection. *Ann. Otol. Rhinol. Laryngol.* 103, 59–69. <https://doi.org/10.1177/000348949410300111>.
 28. Wilson, R., Alton, E., Rutman, A., Higgins, P., Al Nakib, W., Geddes, D.M., Tyrrell, D.A., and Cole, P.J. (1987). Upper respiratory tract viral infection and mucociliary clearance. *Eur. J. Respir. Dis.* 70, 272–279.
 29. Yan, Y., Dalmasso, G., Nguyen, H.T., Obertone, T.S., Charrier-Hisamuddin, L., Sitaraman, S.V., and Merlin, D. (2008). Nuclear factor-kappaB is a critical mediator of Ste20-like proline-/alanine-rich kinase regulation in intestinal inflammation. *Am. J. Pathol.* 173, 1013–1028. <https://doi.org/10.2353/ajpath.2008.080339>.
 30. Shekarabi, M., Zhang, J., Khanna, A.R., Ellison, D.H., Delpire, E., and Kahle, K.T. (2017). WNK kinase signaling in ion homeostasis and human disease. *Cell Metab.* 25, 285–299. <https://doi.org/10.1016/j.cmet.2017.01.007>.

31. Yan, Y., Nguyen, H., Dalmasso, G., Sitaraman, S.V., and Merlin, D. (2007). Cloning and characterization of a new intestinal inflammation-associated colonic epithelial Ste20-related protein kinase isoform. *Biochim. Biophys. Acta* 1769, 106–116. <https://doi.org/10.1016/j.bbexp.2007.01.003>.
32. Weidenfeld, S., and Kuebler, W.M. (2017). Cytokine-regulation of Na⁺-K⁺-Cl⁻ cotransporter 1 and cystic fibrosis transmembrane conductance regulator-potential role in pulmonary inflammation and edema formation. *Front. Immunol.* 8, 393. <https://doi.org/10.3389/fimmu.2017.00393>.
33. Gram, M., Sveinsdottir, S., Cinthio, M., Sveinsdottir, K., Hansson, S.R., Mörgelin, M., Åkerström, B., and Ley, D. (2014). Extracellular hemoglobin - mediator of inflammation and cell death in the choroid plexus following preterm intraventricular hemorrhage. *J. Neuroinflammation* 11, 200. <https://doi.org/10.1186/s12974-014-0200-9>.
34. Karimy, J.K., Zhang, J., Kurland, D.B., Theriault, B.C., Duran, D., Stokum, J.A., Furey, C.G., Zhou, X., Mansuri, M.S., Montejó, J., et al. (2017). Inflammation-dependent cerebrospinal fluid hypersecretion by the choroid plexus epithelium in posthemorrhagic hydrocephalus. *Nat. Med.* 23, 997–1003. <https://doi.org/10.1038/nm.4361>.
35. Purohit, D., Finkel, D.A., Malfa, A., Liao, Y., Ivanova, L., Kleinman, G.M., Hu, F., Shah, S., Thompson, C., Joseph, E., et al. (2021). Human cord blood derived unrestricted somatic stem cells restore Aquaporin Channel expression, reduce inflammation and inhibit the development of hydrocephalus after experimentally induced perinatal intraventricular hemorrhage. *Front. Cell. Neurosci.* 15, 633185. <https://doi.org/10.3389/fncel.2021.633185>.
36. Tan, X., Chen, J., Keep, R.F., Xi, G., and Hua, Y. (2020). Prx2 (peroxiredoxin 2) as a cause of hydrocephalus after intraventricular hemorrhage. *Stroke* 51, 1578–1586. <https://doi.org/10.1161/STROKEAHA.119.028672>.
37. Guillén-Pinto, D., Málaga-Espinoza, B., Ye-Tay, J., Rospigliosi-López, M.L., Montenegro-Rivera, A., Rivas, M., Stiglich, M.L., Villasante-Valera, S., Lizama-Olaya, O., Tori, A., et al. (2020). Neonatal meningitis: a multi-center study in Lima, Peru. *Rev. Peru. Med. Exp. Salud Publica* 37, 210–219. <https://doi.org/10.17843/rpmesp.2020.372.4772>.
38. Huo, L., Fan, Y., Jiang, C., Gao, J., Yin, M., Wang, H., Yang, F., and Cao, Q. (2019). Clinical features of and risk factors for hydrocephalus in childhood bacterial meningitis. *J. Child Neurol.* 34, 11–16. <https://doi.org/10.1177/0883073818799155>.
39. Li, L., Padhi, A., Ranjeva, S.L., Donaldson, S.C., Warf, B.C., Mugamba, J., Johnson, D., Opio, Z., Jayarao, B., Kapur, V., et al. (2011). Association of bacteria with hydrocephalus in Ugandan infants. *J. Neurosurg. Pediatr.* 7, 73–87. <https://doi.org/10.3171/2010.9.PEDS10162>.
40. Hoshino, K., Takeuchi, O., Kawai, T., Sanjo, H., Ogawa, T., Takeda, Y., Takeda, K., and Akira, S. (1999). Cutting edge: toll-like receptor 4 (TLR4)-deficient mice are hyporesponsive to lipopolysaccharide: evidence for TLR4 as the Lps gene product. *J. Immunol.* 162, 3749–3752.
41. Park, B.S., and Lee, J.O. (2013). Recognition of lipopolysaccharide pattern by TLR4 complexes. *Exp. Mol. Med.* 45, e66. <https://doi.org/10.1038/emmm.2013.97>.
42. Janciauskiene, S., Vijayan, V., and Immenschuh, S. (2020). TLR4 signaling by heme and the role of heme-binding blood proteins. *Front. Immunol.* 11, 1964. <https://doi.org/10.3389/fimmu.2020.01964>.
43. Kwon, M.S., Woo, S.K., Kurland, D.B., Yoon, S.H., Palmer, A.F., Banerjee, U., Iqbal, S., Ivanova, S., Gerzanich, V., and Simard, J.M. (2015). Methemoglobin is an endogenous toll-like receptor 4 ligand-relevance to subarachnoid hemorrhage. *Int. J. Mol. Sci.* 16, 5028–5046. <https://doi.org/10.3390/ijms16035028>.
44. Shemie, S., Jay, V., Rutka, J., and Armstrong, D. (1997). Acute obstructive hydrocephalus and sudden death in children. *Ann. Emerg. Med.* 29, 524–528. [https://doi.org/10.1016/s0196-0644\(97\)70227-0](https://doi.org/10.1016/s0196-0644(97)70227-0).
45. Zhang, J., Bhuiyan, M.I.H., Zhang, T., Karimy, J.K., Wu, Z., Fiesler, V.M., Zhang, J., Huang, H., Hasan, M.N., Skrzypiec, A.E., et al. (2020). Modulation of brain cation-Cl⁻ cotransport via the SPAK kinase inhibitor ZT-1a. *Nat. Commun.* 11, 78. <https://doi.org/10.1038/s41467-019-13851-6>.
46. Sarica, C., Tanrikulu, B., Sahin, Y., Dağçınar, A., Baltacıoğlu, F., and Bayrı, Y. (2018). Acute obstructive hydrocephalus due to a giant posterior cerebral artery aneurysm in a pediatric patient. *Pediatr. Neurosurg.* 53, 247–253. <https://doi.org/10.1159/000488458>.
47. Xue, Y., Liu, X., Koundal, S., Constantinou, S., Dai, F., Santambrogio, L., Lee, H., and Benveniste, H. (2020). In vivo T1 mapping for quantifying glymphatic system transport and cervical lymph node drainage. *Sci. Rep.* 10, 14592. <https://doi.org/10.1038/s41598-020-71582-x>.
48. Xue, Y., Gursky, Z., Monte, B., Koundal, S., Liu, X., Lee, H., Michurina, T.V., Mellanson, K.A., Zhao, L., Nemajerova, A., et al. (2022). Sustained glymphatic transport and impaired drainage to the nasal cavity observed in multiciliated cell ciliopathies with hydrocephalus. *Fluids Barriers CNS* 19, 20. <https://doi.org/10.1186/s12987-022-00319-x>.
49. Thalén, S., Maanja, M., Sigfridsson, A., Maret, E., Sörensson, P., and Ugander, M. (2019). The dynamics of extracellular gadolinium-based contrast agent excretion into pleural and pericardial effusions quantified by T1 mapping cardiovascular magnetic resonance. *J. Cardiovasc. Magn. Reson.* 21, 71. <https://doi.org/10.1186/s12968-019-0580-1>.
50. Chen, X., Liu, X., Koundal, S., Elkin, R., Zhu, X., Monte, B., Xu, F., Dai, F., Pedram, M., Lee, H., et al. (2022). Cerebral amyloid angiopathy is associated with glymphatic transport reduction and time-delayed solute drainage along the neck arteries. *Nat. Aging* 2, 214–223. <https://doi.org/10.1038/s43587-022-00181-4>.
51. Zhao, L., Tannenbaum, A., Bakker, E.N.T.P., and Benveniste, H. (2022). Physiology of glymphatic solute transport and waste clearance from the brain. *Physiology (Bethesda)* 37, 0. <https://doi.org/10.1152/physiol.00015.2022>.
52. Proulx, S.T. (2021). Cerebrospinal fluid outflow: a review of the historical and contemporary evidence for arachnoid villi, perineural routes, and dural lymphatics. *Cell. Mol. Life Sci.* 78, 2429–2457. <https://doi.org/10.1007/s00018-020-03706-5>.
53. Hladky, S.B., and Barrand, M.A. (2022). The glymphatic hypothesis: the theory and the evidence. *Fluids Barriers CNS* 19, 9. <https://doi.org/10.1186/s12987-021-00282-z>.
54. Doctor, B.A., Newman, N., Minich, N.M., Taylor, H.G., Fanaroff, A.A., and Hack, M. (2001). Clinical outcomes of neonatal meningitis in very-low birth-weight infants. *Clin. Pediatr. (Phila)* 40, 473–480. <https://doi.org/10.1177/000992280104000901>.
55. Deopujari, C.E., Padayachy, L., Azmi, A., Figaji, A., and Samantray, S.K. (2018). Neuroendoscopy for post-infective hydrocephalus in children. *Childs Nerv. Syst.* 34, 1905–1914. <https://doi.org/10.1007/s00381-018-3901-z>.
56. Liu, G., Mestre, H., Sweeney, A.M., Sun, Q., Weikop, P., Du, T., and Nedergaard, M. (2020). Direct measurement of cerebrospinal fluid production in mice. *Cell Rep.* 33, 108524. <https://doi.org/10.1016/j.celrep.2020.108524>.
57. Javaheri, S., and Wagner, K.R. (1993). Bumetanide decreases canine cerebrospinal fluid production. In vivo evidence for NaCl cotransport in the central nervous system. *J. Clin. Invest.* 92, 2257–2261. <https://doi.org/10.1172/JCI116829>.
58. Karimy, J.K., Duran, D., Hu, J.K., Gavankar, C., Gaillard, J.R., Bayrı, Y., Rice, H., DiLuna, M.L., Gerzanich, V., Marc Simard, J., and Kahle, K.T. (2016). Cerebrospinal fluid hypersecretion in pediatric hydrocephalus. *Neurosurg. Focus* 41, E10. <https://doi.org/10.3171/2016.8.FOCUS16278>.
59. Ferguson, C., McKay, M., Harris, R.A., and Homanics, G.E. (2013). Toll-like receptor 4 (Tlr4) knockout rats produced by transcriptional activator-like effector nuclease (TALEN)-mediated gene inactivation. *Alcohol* 47, 595–599. <https://doi.org/10.1016/j.alcohol.2013.09.043>.
60. Van Hove, H., Martens, L., Scheyltjens, I., De Vlaminck, K., Pombo Antunes, A.R., De Prijck, S., Vandamme, N., De Schepper, S., Van Isterdael, G., Scott, C.L., et al. (2019). A single-cell atlas of mouse brain macrophages reveals unique transcriptional identities shaped by ontogeny and tissue environment. *Nat. Neurosci.* 22, 1021–1035. <https://doi.org/10.1038/s41593-019-0393-4>.

61. Karman, J., Chu, H.H., Co, D.O., Seroogy, C.M., Sandor, M., and Fabry, Z. (2006). Dendritic cells amplify T cell-mediated immune responses in the central nervous system. *J. Immunol.* *177*, 7750–7760. <https://doi.org/10.4049/jimmunol.177.11.7750>.
62. McWhorter, F.Y., Wang, T., Nguyen, P., Chung, T., and Liu, W.F. (2013). Modulation of macrophage phenotype by cell shape. *Proc. Natl. Acad. Sci. USA* *110*, 17253–17258. <https://doi.org/10.1073/pnas.1308887110>.
63. Chistiakov, D.A., Killingsworth, M.C., Myasoedova, V.A., Orekhov, A.N., and Bobryshev, Y.V. (2017). CD68/macrosialin: not just a histochemical marker. *Lab. Invest.* *97*, 4–13. <https://doi.org/10.1038/labinvest.2016.116>.
64. Dodge, P.R., and Swartz, M.N. (1965). Bacterial meningitis—a review of selected aspects. II. Special neurologic problems, postmeningitic complications and clinicopathological correlations. *N. Engl. J. Med.* *272*, 1003. 10 CONCL. <https://doi.org/10.1056/NEJM196505132721906>.
65. Vergouwen, M.D., Schut, E.S., Troost, D., and van de Beek, D. (2010). Diffuse cerebral intravascular coagulation and cerebral infarction in pneumococcal meningitis. *Neurocrit. Care* *13*, 217–227. <https://doi.org/10.1007/s12028-010-9387-5>.
66. Dickson, L.G., and Yassin, M.W. (1969). Meningeal vascular thrombosis and inflammation in pneumococcal meningitis. *J. Egypt. Public Health Assoc.* *44*, 349–355.
67. Engelen-Lee, J.Y., Brouwer, M.C., Aronica, E., and van de Beek, D. (2016). Pneumococcal meningitis: clinical-pathological correlations (MeninGene-Path). *Acta Neuropathol. Commun.* *4*, 26. <https://doi.org/10.1186/s40478-016-0297-4>.
68. Nakano, A., Harada, T., Morikawa, S., and Kato, Y. (1990). Expression of leukocyte common antigen (CD45) on various human leukemia/lymphoma cell lines. *Acta Pathol. Jpn.* *40*, 107–115. <https://doi.org/10.1111/j.1440-1827.1990.tb01549.x>.
69. Rangaraju, S., Raza, S.A., Li, N.X., Betarbet, R., Dammer, E.B., Duong, D., Lah, J.J., Seyfried, N.T., and Levey, A.I. (2018). Differential phagocytic properties of CD45^{low} microglia and CD45^{high} brain mononuclear phagocytes-activation and age-related effects. *Front. Immunol.* *9*, 405. <https://doi.org/10.3389/fimmu.2018.00405>.
70. Sharma, S., Goyal, M.K., Sharma, K., Modi, M., Sharma, M., Khandelwal, N., Prabhakar, S., Sharma, N., R, S., Gairola, J., et al. (2017). Cytokines do play a role in pathogenesis of tuberculous meningitis: a prospective study from a tertiary care center in India. *J. Neurol. Sci.* *379*, 131–136. <https://doi.org/10.1016/j.jns.2017.06.001>.
71. Thwaites, G.E., Macmullen-Price, J., Tran, T.H., Pham, P.M., Nguyen, T.D., Simmons, C.P., White, N.J., Tran, T.H., Summers, D., and Farrar, J.J. (2007). Serial MRI to determine the effect of dexamethasone on the cerebral pathology of tuberculous meningitis: an observational study. *Lancet Neurol.* *6*, 230–236. [https://doi.org/10.1016/S1474-4422\(07\)70034-0](https://doi.org/10.1016/S1474-4422(07)70034-0).
72. Lolanssen, S.D., Rostgaard, N., Oernbo, E.K., Juhler, M., Simonsen, A.H., and MacAulay, N. (2021). Inflammatory markers in cerebrospinal fluid from patients with hydrocephalus: A systematic literature review. *Dis. Markers* *2021*, 8834822. <https://doi.org/10.1155/2021/8834822>.
73. Vitari, A.C., Thastrup, J., Rafiqi, F.H., Deak, M., Morrice, N.A., Karlsson, H.K., and Alessi, D.R. (2006). Functional interactions of the SPAK/OSR1 kinases with their upstream activator WNK1 and downstream substrate NKCC1. *Biochem. J.* *397*, 223–231. <https://doi.org/10.1042/BJ20060220>.
74. Vitari, A.C., Deak, M., Morrice, N.A., and Alessi, D.R. (2005). The WNK1 and WNK4 protein kinases that are mutated in Gordon's hypertension syndrome phosphorylate and activate SPAK and OSR1 protein kinases. *Biochem. J.* *391*, 17–24. <https://doi.org/10.1042/BJ20051180>.
75. Yan, Y., and Merlin, D. (2008). Ste20-related proline/alanine-rich kinase: a novel regulator of intestinal inflammation. *World J. Gastroenterol.* *14*, 6115–6121. <https://doi.org/10.3748/wjg.14.6115>.
76. Polek, T.C., Talpaz, M., and Spivak-Kroizman, T. (2006). The TNF receptor, RELT, binds SPAK and uses it to mediate p38 and JNK activation. *Biochem. Biophys. Res. Commun.* *343*, 125–134. <https://doi.org/10.1016/j.bbrc.2006.02.125>.
77. Delpire, E., and Gagnon, K.B. (2008). SPAK and OSR1: STE20 kinases involved in the regulation of ion homeostasis and volume control in mammalian cells. *Biochem. J.* *409*, 321–331. <https://doi.org/10.1042/BJ20071324>.
78. Richardson, C., and Alessi, D.R. (2008). The regulation of salt transport and blood pressure by the WNK-SPAK/OSR1 signalling pathway. *J. Cell Sci.* *121*, 3293–3304. <https://doi.org/10.1242/jcs.029223>.
79. Dwinell, M.R., Lazar, J., and Geurts, A.M. (2011). The emerging role for rat models in gene discovery. *Mamm. Genome* *22*, 466–475. <https://doi.org/10.1007/s00335-011-9346-2>.
80. Sävman, K., Blennow, M., Hagberg, H., Tarkowski, E., Thoresen, M., and Whitelaw, A. (2002). Cytokine response in cerebrospinal fluid from pre-term infants with posthaemorrhagic ventricular dilatation. *Acta Paediatr.* *91*, 1357–1363. <https://doi.org/10.1111/j.1651-2227.2002.tb02834.x>.
81. Schmitz, T., Heep, A., Groenendaal, F., Hüseman, D., Kie, S., Bartmann, P., Obladen, M., and Felderhoff-Müser, U. (2007). Interleukin-1beta, interleukin-18, and interferon-gamma expression in the cerebrospinal fluid of premature infants with posthemorrhagic hydrocephalus—markers of white matter damage? *Pediatr. Res.* *61*, 722–726. <https://doi.org/10.1203/pdr.0b013e31805341f1>.
82. Figueiredo, R.T., Fernandez, P.L., Mourao-Sa, D.S., Porto, B.N., Dutra, F.F., Alves, L.S., Oliveira, M.F., Oliveira, P.L., Graça-Souza, A.V., and Bozza, M.T. (2007). Characterization of heme as activator of toll-like receptor 4. *J. Biol. Chem.* *282*, 20221–20229. <https://doi.org/10.1074/jbc.M610737200>.
83. Moltani, M., Gemma, S., and Rossetti, C. (2016). The role of toll-like receptor 4 in infectious and noninfectious inflammation. *Mediators Inflamm.* *2016*, 6978936. <https://doi.org/10.1155/2016/6978936>.
84. Jin, S., Guerrero-Juarez, C.F., Zhang, L., Chang, I., Ramos, R., Kuan, C.H., Myung, P., Plikus, M.V., and Nie, Q. (2021). Inference and analysis of cell-cell communication using CellChat. *Nat. Commun.* *12*, 1088. <https://doi.org/10.1038/s41467-021-21246-9>.
85. Kim, J., Erikson, D.W., Burghardt, R.C., Spencer, T.E., Wu, G., Bayless, K.J., Johnson, G.A., and Bazer, F.W. (2010). Secreted phosphoprotein 1 binds integrins to initiate multiple cell signaling pathways, including FRAP1/mTOR, to support attachment and force-generated migration of trophoblast cells. *Matrix Biol.* *29*, 369–382. <https://doi.org/10.1016/j.matbio.2010.04.001>.
86. Bazer, F.W., Song, G., Kim, J., Erikson, D.W., Johnson, G.A., Burghardt, R.C., Gao, H., Carey Satterfield, M., Spencer, T.E., and Wu, G. (2012). Mechanistic mammalian target of rapamycin (mTOR) cell signaling: effects of select nutrients and secreted phosphoprotein 1 on development of mammalian conceptuses. *Mol. Cell. Endocrinol.* *354*, 22–33. <https://doi.org/10.1016/j.mce.2011.08.026>.
87. Anwar, M.A., Shah, M., Kim, J., and Choi, S. (2019). Recent clinical trends in toll-like receptor targeting therapeutics. *Med. Res. Rev.* *39*, 1053–1090. <https://doi.org/10.1002/med.21553>.
88. Josiah, S.S., Meor Azlan, N.F., and Zhang, J. (2021). Targeting the WNK-SPAK/OSR1 pathway and cation-chloride cotransporters for the therapy of stroke. *Int. J. Mol. Sci.* *22*. <https://doi.org/10.3390/ijms22031232>.
89. Nishida, H., Sohara, E., Nomura, N., Chiga, M., Alessi, D.R., Rai, T., Sasaki, S., and Uchida, S. (2012). Phosphatidylinositol 3-kinase/Akt signaling pathway activates the WNK-OSR1/SPAK-NCC phosphorylation cascade in hyperinsulinemic db/db mice. *Hypertension* *60*, 981–990. <https://doi.org/10.1161/HYPERTENSIONAHA.112.201509>.
90. Sørensen, M.V., Saha, B., Jensen, I.S., Wu, P., Ayasse, N., Gleason, C.E., Svendsen, S.L., Wang, W.H., and Pearce, D. (2019). Potassium acts through mTOR to regulate its own secretion. *JCI Insight* *5*, e126910. <https://doi.org/10.1172/jci.insight.126910>.

91. Weichhart, T., Hengstschläger, M., and Linke, M. (2015). Regulation of innate immune cell function by mTOR. *Nat. Rev. Immunol.* *15*, 599–614. <https://doi.org/10.1038/nri3901>.
92. Xu, F., Na, L., Li, Y., and Chen, L. (2020). Roles of the PI3K/AKT/mTOR signalling pathways in neurodegenerative diseases and tumours. *Cell Biosci.* *10*, 54. <https://doi.org/10.1186/s13578-020-00416-0>.
93. Robert, S.M., Reeves, B.C., Marlier, A., Duy, P.Q., DeSpensa, T., Kundishora, A., Kiziltug, E., Singh, A., Allington, G., Alper, S.L., and Kahle, K.T. (2021). Inflammatory hydrocephalus. *Childs Nerv. Syst.* *37*, 3341–3353. <https://doi.org/10.1007/s00381-021-05255-z>.
94. Garoon, R.B., Foroozan, R., and Vaphiades, M.S. (2017). Don't drink in the valley. *Surv. Ophthalmol.* *62*, 383–386. <https://doi.org/10.1016/j.survophthal.2016.04.002>.
95. Stone, S.S., and Warf, B.C. (2014). Combined endoscopic third ventriculostomy and choroid plexus cauterization as primary treatment for infant hydrocephalus: a prospective North American series. *J. Neurosurg. Pediatr.* *14*, 439–446. <https://doi.org/10.3171/2014.7.PEDS14152>.
96. Buxton, N., and Punt, J. (1997). Choroid plexus papilloma producing symptoms by secretion of cerebrospinal fluid. *Pediatr. Neurosurg.* *27*, 108–111. <https://doi.org/10.1159/000121236>.
97. Eisenberg, H.M., McComb, J.G., and Lorenzo, A.V. (1974). Cerebrospinal fluid overproduction and hydrocephalus associated with choroid plexus papilloma. *J. Neurosurg.* *40*, 381–385. <https://doi.org/10.3171/jns.1974.40.3.0381>.
98. Milhorat, T.H., Hammock, M.K., Davis, D.A., and Fenstermacher, J.D. (1976). Choroid plexus papilloma. I. Proof of cerebrospinal fluid overproduction. *Childs Brain* *2*, 273–289.
99. Anei, R., Hayashi, Y., Hiroshima, S., Mitsui, N., Orimoto, R., Uemori, G., Saito, M., Sato, M., Wada, H., Hododuka, A., and Kamada, K. (2011). Hydrocephalus due to diffuse villous hyperplasia of the choroid plexus. *Neurol. Med. Chir. (Tokyo)* *51*, 437–441. <https://doi.org/10.2176/nmc.51.437>.
100. Cataltepe, O., Liptzin, D., Jolley, L., and Smith, T.W. (2010). Diffuse villous hyperplasia of the choroid plexus and its surgical management. *J. Neurosurg. Pediatr.* *5*, 518–522. <https://doi.org/10.3171/2009.12.PEDS0960>.
101. Furey, C., Antwi, P., Duran, D., Timberlake, A.T., Nelson-Williams, C., Matouk, C.C., DiLuna, M.L., Günel, M., and Kahle, K.T. (2018). 9p24 triplication in syndromic hydrocephalus with diffuse villous hyperplasia of the choroid plexus. *Cold Spring Harb. Mol. Case Stud.* *4*, a003145. <https://doi.org/10.1101/mcs.a003145>.
102. Jin, S.C., Dong, W., Kundishora, A.J., Panchagnula, S., Moreno-DeLuca, A., Furey, C.G., Allocco, A.A., Walker, R.L., Nelson-Williams, C., Smith, H., et al. (2020). Exome sequencing implicates genetic disruption of prenatal neuro-gliogenesis in sporadic congenital hydrocephalus. *Nat. Med.* *26*, 1754–1765. <https://doi.org/10.1038/s41591-020-1090-2>.
103. Erickson, M.A., Hartvigson, P.E., Morofuji, Y., Owen, J.B., Butterfield, D.A., and Banks, W.A. (2012). Lipopolysaccharide impairs amyloid beta efflux from brain: altered vascular sequestration, cerebrospinal fluid reabsorption, peripheral clearance and transporter function at the blood-brain barrier. *J. Neuroinflammation* *9*, 150. <https://doi.org/10.1186/1742-2094-9-150>.
104. Manouchehrian, O., Ramos, M., Bachiller, S., Lundgaard, I., and Deierborg, T. (2021). Acute systemic LPS-exposure impairs perivascular CSF distribution in mice. *J. Neuroinflammation* *18*, 34. <https://doi.org/10.1186/s12974-021-02082-6>.
105. Fratamico, P.M., DebRoy, C., Liu, Y., Needleman, D.S., Baranzoni, G.M., and Feng, P. (2016). Advances in molecular serotyping and subtyping of *Escherichia coli*. *Front. Microbiol.* *7*, 644. <https://doi.org/10.3389/fmicb.2016.00644>.
106. Kaczmarek, A., Budzyńska, A., and Gospodarek, E. (2014). Detection of K1 antigen of *Escherichia coli* rods isolated from pregnant women and neonates. *Folia Microbiol. (Praha)* *59*, 419–422. <https://doi.org/10.1007/s12223-014-0315-5>.
107. Hu, X., Deng, Q., Ma, L., Li, Q., Chen, Y., Liao, Y., Zhou, F., Zhang, C., Shao, L., Feng, J., et al. (2020). Meningeal lymphatic vessels regulate brain tumor drainage and immunity. *Cell Res.* *30*, 229–243. <https://doi.org/10.1038/s41422-020-0287-8>.
108. Papadopoulos, Z., Herz, J., and Kipnis, J. (2020). Meningeal lymphatics: from anatomy to central nervous system immune surveillance. *J. Immunol.* *204*, 286–293. <https://doi.org/10.4049/jimmunol.1900838>.
109. Hajam, I.A., Dar, P.A., Shah Nawaz, I., Jaume, J.C., and Lee, J.H. (2017). Bacterial flagellin—a potent immunomodulatory agent. *Exp. Mol. Med.* *49*, e373. <https://doi.org/10.1038/emm.2017.172>.
110. Engelhardt, B., Wolburg-Buchholz, K., and Wolburg, H. (2001). Involvement of the choroid plexus in central nervous system inflammation. *Microsc. Res. Tech.* *52*, 112–129. [https://doi.org/10.1002/1097-0029\(20010101\)52:1<112::AID-JEMT13>3.0.CO;2-5](https://doi.org/10.1002/1097-0029(20010101)52:1<112::AID-JEMT13>3.0.CO;2-5).
111. Ghersi-Egea, J.F., Strazielle, N., Catala, M., Silva-Vargas, V., Doetsch, F., and Engelhardt, B. (2018). Molecular anatomy and functions of the choroidal blood-cerebrospinal fluid barrier in health and disease. *Acta Neuropathol.* *135*, 337–361. <https://doi.org/10.1007/s00401-018-1807-1>.
112. Gu, C., Hao, X., Li, J., Hua, Y., Keep, R.F., and Xi, G. (2019). Effects of minocycline on epileptus macrophage activation, choroid plexus injury and hydrocephalus development in spontaneous hypertensive rats. *J. Cereb. Blood Flow Metab.* *39*, 1936–1948. <https://doi.org/10.1177/0271678X19836117>.
113. Stridh, L., Ek, C.J., Wang, X., Nilsson, H., and Mallard, C. (2013). Regulation of toll-like receptors in the choroid plexus in the immature brain after systemic inflammatory stimuli. *Transl. Stroke Res.* *4*, 220–227. <https://doi.org/10.1007/s12975-012-0248-8>.
114. Shimada, A., and Hasegawa-Ishii, S. (2021). Increased cytokine expression in the choroid plexus stroma and epithelium in response to endotoxin-induced systemic inflammation in mice. *Toxicol. Rep.* *8*, 520–528. <https://doi.org/10.1016/j.toxrep.2021.03.002>.
115. Akira, S., and Takeda, K. (2004). Toll-like receptor signalling. *Nat. Rev. Immunol.* *4*, 499–511. <https://doi.org/10.1038/nri1391>.
116. Laird, M.D., Shields, J.S., Sukumari-Ramesh, S., Kimbler, D.E., Fessler, R.D., Shakir, B., Youssef, P., Yanasak, N., Vender, J.R., and Dhandapani, K.M. (2014). High mobility group box protein-1 promotes cerebral edema after traumatic brain injury via activation of toll-like receptor 4. *Glia* *62*, 26–38. <https://doi.org/10.1002/glia.22581>.
117. Chen, T., Tan, X., Xia, F., Hua, Y., Keep, R.F., and Xi, G. (2021). Hydrocephalus induced by intraventricular Peroxiredoxin-2: the role of macrophages in the choroid plexus. *Biomolecules* *11*. <https://doi.org/10.3390/biom11050654>.
118. Merle, N.S., Paule, R., Leon, J., Daugan, M., Robe-Rybkin, T., Poillierat, V., Torset, C., Frémeaux-Bacchi, V., Dimitrov, J.D., and Roumenina, L.T. (2019). P-selectin drives complement attack on endothelium during intravascular hemolysis in TLR-4/heme-dependent manner. *Proc. Natl. Acad. Sci. USA* *116*, 6280–6285. <https://doi.org/10.1073/pnas.1814797116>.
119. Nader, E., Romana, M., and Connes, P. (2020). The red blood cell-inflammation vicious circle in sickle cell disease. *Front. Immunol.* *11*, 454. <https://doi.org/10.3389/fimmu.2020.00454>.
120. Haas, J., Rudolph, H., Costa, L., Faller, S., Libicher, S., Würthwein, C., Jarius, S., Ishikawa, H., Stump-Guthier, C., Tenenbaum, T., et al. (2020). The choroid plexus is permissive for a preactivated antigen-experienced memory B-cell subset in multiple sclerosis. *Front. Immunol.* *11*, 618544. <https://doi.org/10.3389/fimmu.2020.618544>.
121. Kim, H., Lim, Y.M., Kim, G., Lee, E.J., Lee, J.H., Kim, H.W., and Kim, K.K. (2020). Choroid plexus changes on magnetic resonance imaging in multiple sclerosis and neuromyelitis optica spectrum disorder. *J. Neurol. Sci.* *415*, 116904. <https://doi.org/10.1016/j.jns.2020.116904>.

122. Yan, Y., Dalmaso, G., Nguyen, H.T., Obertone, T.S., Sitaraman, S.V., and Merlin, D. (2009). Ste20-related proline/alanine-rich kinase (SPAK) regulated transcriptionally by hyperosmolarity is involved in intestinal barrier function. *PLoS One* 4, e5049. <https://doi.org/10.1371/journal.pone.0005049>.
123. Yan, Y., Laroui, H., Ingersoll, S.A., Ayyadurai, S., Charania, M., Yang, S., Dalmaso, G., Obertone, T.S., Nguyen, H., Sitaraman, S.V., and Merlin, D. (2011). Overexpression of Ste20-related proline/alanine-rich kinase exacerbates experimental colitis in mice. *J. Immunol.* 187, 1496–1505. <https://doi.org/10.4049/jimmunol.1002910>.
124. Alessi, D.R., Zhang, J., Khanna, A., Hochdörfer, T., Shang, Y., and Kahle, K.T. (2014). The WNK-SPAK/OSR1 pathway: master regulator of cation-chloride cotransporters. *Sci. Signal.* 7, re3. <https://doi.org/10.1126/scisignal.2005365>.
125. Chaplin, E.R., Goldstein, G.W., Myerberg, D.Z., Hunt, J.V., and Tooley, W.H. (1980). Posthemorrhagic hydrocephalus in the preterm infant. *Pediatrics* 65, 901–909.
126. Steffensen, A.B., Oernbo, E.K., Stoica, A., Gerkau, N.J., Barbuskaite, D., Tritsaris, K., Rose, C.R., and MacAulay, N. (2018). Cotransporter-mediated water transport underlying cerebrospinal fluid formation. *Nat. Commun.* 9, 2167. <https://doi.org/10.1038/s41467-018-04677-9>.
127. Stödberg, T., Magnusson, M., Lesko, N., Wredenberg, A., Martin Munoz, D., Stranneheim, H., and Wedell, A. (2020). SLC12A2 mutations cause NKCC1 deficiency with encephalopathy and impaired secretory epithelia. *Neurol. Genet.* 6, e478. <https://doi.org/10.1212/NXG.0000000000000478>.
128. Xu, H., Fame, R.M., Sadegh, C., Sutin, J., Naranjo, C., Della, Syau, Cui, J., Shipley, F.B., Vernon, A., Gao, F., et al. (2021). Choroid plexus NKCC1 mediates cerebrospinal fluid clearance during mouse early postnatal development. *Nat. Commun.* 12, 447. <https://doi.org/10.1038/s41467-020-20666-3>.
129. Thastrup, J.O., Rafiqi, F.H., Vitari, A.C., Pozo-Guisado, E., Deak, M., Mehellou, Y., and Alessi, D.R. (2012). SPAK/OSR1 regulate NKCC1 and WNK activity: analysis of WNK isoform interactions and activation by T-loop trans-autophosphorylation. *Biochem. J.* 441, 325–337. <https://doi.org/10.1042/BJ20111879>.
130. Karimy, J.K., Reeves, B.C., and Kahle, K.T. (2020). Targeting TLR4-dependent inflammation in post-hemorrhagic brain injury. *Expert Opin. Ther. Targets* 24, 525–533. <https://doi.org/10.1080/14728222.2020.1752182>.
131. Matsunaga, N., Tsuchimori, N., Matsumoto, T., and Ii, M. (2011). TAK-242 (resatorvid), a small-molecule inhibitor of toll-like receptor (TLR) 4 signaling, binds selectively to TLR4 and interferes with interactions between TLR4 and its adaptor molecules. *Mol. Pharmacol.* 79, 34–41. <https://doi.org/10.1124/mol.110.068064>.
132. Kotani, T., Setiawan, J., Konno, T., Ihara, N., Okamoto, S., Saito, Y., Murata, Y., Noda, T., and Matozaki, T. (2020). Regulation of colonic epithelial cell homeostasis by mTORC1. *Sci. Rep.* 10, 13810. <https://doi.org/10.1038/s41598-020-70655-1>.
133. Zhou, M., Xu, W., Wang, J., Yan, J., Shi, Y., Zhang, C., Ge, W., Wu, J., Du, P., and Chen, Y. (2018). Boosting mTOR-dependent autophagy via upstream TLR4-MyD88-MAPK signalling and downstream NF- κ B pathway quenches intestinal inflammation and oxidative stress injury. *EBiomedicine* 35, 345–360. <https://doi.org/10.1016/j.ebiom.2018.08.035>.
134. Yu, M., Kang, X., Xue, H., and Yin, H. (2011). Toll-like receptor 4 is up-regulated by mTOR activation during THP-1 macrophage foam cells formation. *Acta Biochim. Biophys. Sin. (Shanghai)* 43, 940–947. <https://doi.org/10.1093/abbs/gmr093>.
135. SenGupta, S., Lorente-Rodríguez, A., Earnest, S., Stippec, S., Guo, X., Trudgian, D.C., Mirzaei, H., and Cobb, M.H. (2013). Regulation of OSR1 and the sodium, potassium, two chloride cotransporter by convergent signals. *Proc. Natl. Acad. Sci. USA* 110, 18826–18831. <https://doi.org/10.1073/pnas.1318676110>.
136. Krueger, D.A., Care, M.M., Holland, K., Agrícola, K., Tudor, C., Mangeshkar, P., Wilson, K.A., Byars, A., Sahnoud, T., and Franz, D.N. (2010). Everolimus for subependymal giant-cell astrocytomas in tuberous sclerosis. *N. Engl. J. Med.* 363, 1801–1811. <https://doi.org/10.1056/NEJMoa1001671>.
137. Li, J., Kim, S.G., and Blenis, J. (2014). Rapamycin: one drug, many effects. *Cell Metab.* 19, 373–379. <https://doi.org/10.1016/j.cmet.2014.01.001>.
138. Ye, X., Zhu, M., Che, X., Wang, H., Liang, X.J., Wu, C., Xue, X., and Yang, J. (2020). Lipopolysaccharide induces neuroinflammation in microglia by activating the MTOR pathway and downregulating Vps34 to inhibit autophagosome formation. *J. Neuroinflammation* 17, 18. <https://doi.org/10.1186/s12974-019-1644-8>.
139. Mengke, N.S., Hu, B., Han, Q.P., Deng, Y.Y., Fang, M., Xie, D., Li, A., and Zeng, H.K. (2016). Rapamycin inhibits lipopolysaccharide-induced neuroinflammation in vitro and in vivo. *Mol. Med. Rep.* 14, 4957–4966. <https://doi.org/10.3892/mmr.2016.5883>.
140. Janostiak, R., Rauniyar, N., Lam, T.T., Ou, J., Zhu, L.J., Green, M.R., and Wajapeyee, N. (2017). MELK promotes melanoma growth by stimulating the NF- κ B pathway. *Cell Rep.* 21, 2829–2841. <https://doi.org/10.1016/j.celrep.2017.11.033>.
141. Hao, Y., Hao, S., Andersen-Nissen, E., Mauck, W.M., 3rd, Zheng, S., Butler, A., Lee, M.J., Wilk, A.J., Darby, C., Zager, M., et al. (2021). Integrated analysis of multimodal single-cell data. *Cell* 184, 3573–3587.e29. <https://doi.org/10.1016/j.cell.2021.04.048>.
142. Gárate, I., García-Bueno, B., Madrigal, J.L., Caso, J.R., Alou, L., Gómez-Lus, M.L., and Leza, J.C. (2014). Toll-like 4 receptor inhibitor TAK-242 decreases neuroinflammation in rat brain frontal cortex after stress. *J. Neuroinflammation* 11, 8. <https://doi.org/10.1186/1742-2094-11-8>.
143. Schindelin, J., Arganda-Carreras, I., Frise, E., Kaynig, V., Longair, M., Pietzsch, T., Preibisch, S., Rueden, C., Saalfeld, S., Schmid, B., et al. (2012). Fiji: an open-source platform for biological-image analysis. *Nat. Methods* 9, 676–682. <https://doi.org/10.1038/nmeth.2019>.
144. Zhang, J., Gao, G., Begum, G., Wang, J., Khanna, A.R., Shmukler, B.E., Daubner, G.M., de Los Heros, P., Davies, P., Varghese, J., et al. (2016). Functional kinomics establishes a critical node of volume-sensitive cation-Cl⁻ cotransporter regulation in the mammalian brain. *Sci. Rep.* 6, 35986. <https://doi.org/10.1038/srep35986>.
145. Anders, S., Pyl, P.T., and Huber, W. (2015). HTSeq—a Python framework to work with high-throughput sequencing data. *Bioinformatics* 31, 166–169. <https://doi.org/10.1093/bioinformatics/btu638>.
146. Love, M.I., Huber, W., and Anders, S. (2014). Moderated estimation of fold change and dispersion for RNA-seq data with DESeq2. *Genome Biol.* 15, 550. <https://doi.org/10.1186/s13059-014-0550-8>.
147. Gu, Z., Eils, R., and Schlesner, M. (2016). Complex heatmaps reveal patterns and correlations in multidimensional genomic data. *Bioinformatics* 32, 2847–2849. <https://doi.org/10.1093/bioinformatics/btw313>.
148. Lee, A.M., Mansuri, M.S., Wilson, R.S., Lam, T.T., Nairn, A.C., and Picciotto, M.R. (2021). Sex differences in the ventral tegmental area and nucleus accumbens proteome at baseline and following nicotine exposure. *Front. Mol. Neurosci.* 14, 657064. <https://doi.org/10.3389/fnmol.2021.657064>.
149. McAlister, G.C., Nusinow, D.P., Jedrychowski, M.P., Wühr, M., Huttlin, E.L., Erickson, B.K., Rad, R., Haas, W., and Gygi, S.P. (2014). MultiNotch MS3 enables accurate, sensitive, and multiplexed detection of differential expression across cancer cell line proteomes. *Anal. Chem.* 86, 7150–7158. <https://doi.org/10.1021/ac502040v>.
150. Miller, M.B., Wilson, R.S., Lam, T.T., Nairn, A.C., and Picciotto, M.R. (2018). Evaluation of the phosphoproteome of mouse alpha 4/beta 2-containing nicotinic acetylcholine receptors in vitro and in vivo. *Proteomes* 6, 42. <https://doi.org/10.3390/proteomes6040042>.
151. Montoro, D.T., Haber, A.L., Biton, M., Vinarsky, V., Lin, B., Birket, S.E., Yuan, F., Chen, S., Leung, H.M., Villoria, J., et al. (2018). A revised airway epithelial hierarchy includes CFTR-expressing ionocytes. *Nature* 560, 319–324. <https://doi.org/10.1038/s41586-018-0393-7>.

152. Becht, E., McInnes, L., Healy, J., Dutertre, C.A., Kwok, I.W.H., Ng, L.G., Ginhoux, F., and Newell, E.W. (2018). Dimensionality reduction for visualizing single-cell data using UMAP. *Nat. Biotechnol.* <https://doi.org/10.1038/nbt.4314>.
153. McGinnis, C.S., Murrow, L.M., and Gartner, Z.J. (2019). DoubletFinder: doublet detection in single-cell RNA sequencing data using artificial nearest neighbors. *Cell Syst.* *8*, 329–337.e4. <https://doi.org/10.1016/j.cels.2019.03.003>.
154. Cao, J., Spielmann, M., Qiu, X., Huang, X., Ibrahim, D.M., Hill, A.J., Zhang, F., Mundlos, S., Christiansen, L., Steemers, F.J., et al. (2019). The single-cell transcriptional landscape of mammalian organogenesis. *Nature* *566*, 496–502. <https://doi.org/10.1038/s41586-019-0969-x>.
155. Federico, A., and Monti, S. (2020). hypeR: an R package for geneset enrichment workflows. *Bioinformatics* *36*, 1307–1308. <https://doi.org/10.1093/bioinformatics/btz700>.
156. Kuleshov, M.V., Jones, M.R., Rouillard, A.D., Fernandez, N.F., Duan, Q., Wang, Z., Koplev, S., Jenkins, S.L., Jagodnik, K.M., Lachmann, A., et al. (2016). Enrichr: a comprehensive gene set enrichment analysis web server 2016 update. *Nucleic Acids Res.* *44*, W90–W97. <https://doi.org/10.1093/nar/gkw377>.
157. Tustison, N.J., Avants, B.B., Cook, P.A., Zheng, Y., Egan, A., Yushkevich, P.A., and Gee, J.C. (2010). N4ITK: improved N3 bias correction. *IEEE Trans. Med. Imaging* *29*, 1310–1320. <https://doi.org/10.1109/TMI.2010.2046908>.
158. Koundal, S., Liu, X., Sanggaard, S., Mortensen, K., Wardlaw, J., Nedergaard, M., Benveniste, H., and Lee, H. (2019). Brain morphometry and longitudinal relaxation time of spontaneously hypertensive rats (SHRs) in early and intermediate stages of hypertension investigated by 3D VFA-SPGR MRI. *Neuroscience* *404*, 14–26. <https://doi.org/10.1016/j.neuroscience.2019.01.030>.
159. Smith, N.M., Ford, J.N., Haghdel, A., Glodzik, L., Li, Y., D'Angelo, D., RoyChoudhury, A., Wang, X., Blennow, K., de Leon, M.J., and Ivanidze, J. (2022). Statistical parametric mapping in amyloid positron emission tomography. *Front. Aging Neurosci.* *14*, 849932. <https://doi.org/10.3389/fnagi.2022.849932>.

STAR★METHODS

KEY RESOURCES TABLE

REAGENT or RESOURCE	SOURCE	IDENTIFIER
Antibodies		
AQP1, Rabbit Recombinant Monoclonal	Abcam	Ab168387 (Abcam Cat# ab168387, RRID:AB_2810992)
ATP1A, Rabbit Polyclonal	Alomone	ANP-001
CD68, Rabbit Monoclonal	CST	97778
CLIC6, Mouse Monoclonal	Santa Cruz	365303 (Santa Cruz Biotechnology Cat# sc-365303, RRID:AB_10851345)
ED1/CD68, Mouse Monoclonal	Millipore	MAB1435 (Millipore Cat# MAB1435, RRID:AB_177576)
IBA1, Goat Polyclonal	Thermo	PA5-18039 (Thermo Fisher Scientific Cat# PA5-18039, RRID:AB_10982846)
KCNJ13, Mouse Monoclonal	Santa Cruz	398810
Ki67, Rabbit Monoclonal	CST	9129
pNKCC1, Rabbit Polyclonal	Millipore	ABS 1004
pSPAK, Rabbit Polyclonal	Millipore	07-2273 (Millipore Cat# 07-2273, RRID:AB_11205577)
RELT, Rabbit Polyclonal	Novus	NBP2-56851
NKCC1, Rabbit Monoclonal	CST	85403S
Anti-WNK1	University of Dundee	S079B
Anti-SPAK	University of Dundee	S365D
Anti-NKCC1	University of Dundee	S022D
Anti-ATP1A1	DSHB	a5 (DSHB Cat# a5, RRID:AB_2166869)
Anti-HRP	Pierce	21130
Anti-beta Actin	Abcam	Ab8227 (Abcam Cat# ab8227, RRID:AB_2305186)
CD16-32	Biolegend	Cat#: 101302 (BioLegend Cat# 101302, RRID:AB_312801)
CD45-PE/cy7	Biolegend	Cat#: 202207 (BioLegend Cat# 202207, RRID:AB_314006)
CD3-647	Biolegend	Cat#: 201408 (BioLegend Cat# 201408, RRID:AB_893304)
Alexa Fluor 488	Invitrogen	Cat#: A32723
Alexa Fluor 555	Invitrogen	Cat#: A32816
Alexa Fluor 647	Invitrogen	Cat#: A32849
Bacterial and virus strains		
<i>E. Coli</i> ^{+LPS} (BD21)	Lucigen	<i>E. coli</i> EXPRESS BL21(DE3)
<i>E. Coli</i> ^{-LPS} (ClearColi)	Lucigen	CLEARCOLI BL21
Chemicals, peptides, and recombinant proteins		
Bumetanide	Sigma-Aldrich	CAS#: 28395-03-1
aCSF	Harvard Apparatus	Item#: 59-7316
Rapamycin	Cayman	Item#: 13346
Deposited data		
Bulk RNA Seq	GEO	GEO: GSE192946
Mass Spectrometry Proteomics Data	PRIDE	PXD030678
ScRNA Seq	GEO	GEO: GSE218143

(Continued on next page)

Continued

REAGENT or RESOURCE	SOURCE	IDENTIFIER
Experimental models: Organisms/strains		
Wistar Rats, Albino	Charles River	Strain code 003
Software and algorithms		
Seurat	Hao et al. ¹⁴⁰	https://satijalab.org/seurat/
Monocle3	Cao et al. ¹⁴¹	https://cole-trapnell-lab.github.io/monocle3/
Cellchat	Jin et al. ⁸⁴	https://github.com/sqjin/CellChat

RESOURCE AVAILABILITY**Lead contact**

Requests for further information should be directed to and will be fulfilled by the lead contact, Kristopher Kahle (kahle.kristopher@mg.harvard.edu).

Materials availability

Rat lines generated in this study have been deposited to the Knockout Mouse Project (KOMP), Charles River, albino wistar rats, strain code 003.

Data and code availability

- Single-cell RNA-seq data have been deposited at GEO and are publicly available as of the date of publication. Accession numbers are listed in the [key resources table](#). The mass spectrometry proteomics data have been deposited to the ProteomeXchange Consortium via the PRIDE¹ partner repository with the dataset identifier PXD030678. Any FACS or microscopy data, confocal, or other, reported in this paper will be shared by the [lead contact](#) upon request. All materials and associated protocols can be found within the [STAR Methods](#) section of this paper, and any relevant papers are also cited for further reference. In addition to the methods provided here, for additional explanations of the IVH protocol or direct CSF measurements, please see published works,^{2,3,4} or additional information can be addressed via contact with the corresponding article of this manuscript.
- This paper does not report original code. All previously published algorithms are listed in the key resources table.
- Any additional information required to reanalyze the data reported in this paper is available from the [lead contact](#) upon request.

EXPERIMENTAL MODEL AND SUBJECT DETAILS**Rodent Model**

Animal experiments were performed under a protocol approved by the Institutional Animal Care and Use Committee (IACUC) of Yale University and in accordance with the guidelines and regulations in the NIH Guide for the Care and Use of Laboratory Animals. Male and Female Wistar rats (Charles River, Wilmington, MA, USA) of wild type and *Stk39*^{-/-79} and *Tlr4*^{-/-59} genotypes, aged 8 weeks (200–350 g) and bred in accordance with an IACUC-approved protocol at the Yale University School of Medicine, New Haven, CT were anesthetized (90 mg/kg body weight ketamine plus 7.5 mg/kg body weight xylazine, i.p.) and allowed to breathe room air spontaneously. Body temperature was maintained at 37 ± 1 °C (Harvard Apparatus, Holliston, MA) throughout the course of the experiments. This study randomly chose animals for either control or experimental conditions and the researchers were not blinded. Female rats were excluded from this study to avoid introducing sex as an additional variable. Animals were determined to be healthy by the veterinary staff, were immunocompetent, no involved in previous procedures (other than those directly related to this project and described below in the [Method Details](#) section), were drug and test naïve (other than those directly related to this project and described below in the [method details](#) section), and were kept under standard, IACUC approved husbandry and housing conditions at Yale.

Porcine Model

All porcine studies were performed in collaboration with the Dardik laboratory at Yale University and in compliance with federal guidelines and protocols approved by the Yale University Institutional Animal Care and Use Committee. Yorkshire male pigs, with mean age of 3.4 months, were delivered to our facility 7–10 days prior to any procedures, kept under standard and IACUC approved husbandry and housing conditions at Yale, and were determined to be healthy after examination by veterinary staff. Animals had not undergone any previous procedures and were drug and test naïve.

METHOD DETAILS

Model of post-hemorrhagic hydrocephalus

IVH was modeled using our previously published methods,³⁴ and detailed here. In an anesthetized animal, the hair on the dorsal side of the skull was initially shaved using clippers. A 2.5 cm incision was made in the proximal tail (beginning 2.5 cm below the rectum) using a scalpel (Bard-Parker, #10 Carbon Steel Surgical Blade) and the tail artery was then aseptically cannulated using a flexible catheter (PE-20) pre-loaded with heparinized saline. The rat was then mounted in a stereotactic apparatus (Stoelting Co., Wood Dale, IL), a 2.5 cm midline scalp incision was made using a new scalpel blade to expose the aponeurosis, and the skin was retracted using Barraquer retractors (Harvard Apparatus). The aponeurosis was then cut via a midline incision and carefully retracted using the same scalpel. The surface of the skull was cleaned using 0.9% Sodium Chloride (Hospira, Lake Forest, IL) and dried using 16 ply 4x4 sterile gauze sponges (Covidien, Mansfield, MA). Any bleeding from the skull was burned using a cautery pen (Bovie, Clearwater, FL). After the skull was dry, a 1 mm burr hole was made using a high-speed drill over the right lateral ventricle (coordinates, $x = -0.8$, $y = -1.7$ mm from bregma) and the skull was subsequently cleaned and allowed to dry using the same method as indicated above. Approximately 150 μL of blood was then drawn from the tail artery catheter into a 1 mL syringe initially filled with 500 μL of heparinized saline and was subsequently discarded. An additional 50 μL of blood was then drawn into a new, sterile 1 mL syringe and immediately transferred into a 500 μL syringe (Hamilton, Reno, NV), which was then mounted to the stereotactic frame. Under stereotactic guidance, 50 μL of freshly collected autologous blood, free from anticoagulants, was infused into the right lateral ventricle (coordinates, $x = -0.8$, $y = -1.7$, $z = -4.5$ mm from bregma), over the course of 5 minutes, and the 26-gauge needle was held in place for an additional 20 minutes to prevent blood backflow from the the burr hole upon needle removal. The incisions were then sutured with a simple uninterrupted stich using 4-0 2.0 Metric DemeGUT absorbable surgical suture (DemeTECH, Miami Lakes, FL). Intraventricular sterile aCSF (Harvard Apparatus) infused in the same manner served as the IVH control condition.

Model of post-infectious hydrocephalus

As in the model of post-hemorrhagic hydrocephalus outlined above, an anesthetized rat with shaved dorsal skull was mounted into a stereotactic apparatus (Stoelting Co.), and a 1-inch midline scalp incision was made with a scalpel blade to expose the fascia on the dorsal side of the skull. The aponeurosis was then incised midline and carefully retracted with the same scalpel blade. The surface of the skull was then cleaned using 0.9% Sodium Chloride, dried with 16 ply 4x4 sterile gauze sponges, and any skull bleeding cauterized by cautery pen. A high-speed drill was used to make a 1 mm burr hole in the dry skull over the right lateral ventricle (coordinates, $x = -0.8$, $y = -1.7$ mm from bregma), and the skull subsequently cleaned and allowed to dry as above. After the skull was sufficiently dry, a brain infusion cannula with depth adjusted to 4.5 mm using 1 spacer (Alzet, Cupertino, CA; brain infusion and cannula kit, #2) was mounted with veterinary surgical cyanoacrylate adhesive (Covetrus, Dublin, OH) into the right lateral ventricle ($x = -0.8$, $y = -1.7$ relative to bregma). A small horizontal incision was then made just above the spinotrapezius muscle overlying the neck and upper back. An osmotic pump (Alzet, 1003D, rate: 1 mL/hr), filled 12h earlier with lipopolysaccharide (LPS; Enzo, Serotype O55:B5) diluted in aCSF (10 ng/mL) or *E. coli* (Lucigen) diluted in aCSF (see below), was then placed subcutaneously in the caudal portion of the dorsum and connected to the cannula attached to the skull using PE tubing provided in the Alzet brain infusion kit. The incisions were then sutured via a simple uninterrupted stich using 4-0 2.0 Metric DemeGUT absorbable surgical suture. Control animals were treated identically, but with aCSF loaded into the osmotic pump.

ICV-infusion of *E. coli*

Wild-type *E. coli* and ClearColi (*E. coli* lacking functional surface LPS; Lucigen BD21; <https://www.nature.com/articles/nmeth.f.367.pdf?origin=ppub>) were cultured originally on standard LB-agar plates. A single colony from each strain was used for inoculation in 10 mL of standard LB broth and incubated overnight at 37 degrees Celsius. To get a specific number of cells per milliliter, 10 mL of LB was then inoculated with 100 μL of the overnight culture and grown at 37 degrees Celsius for 3 hours to achieve bacterial growth at log phase. The cells were harvested by centrifugation at 2000 RPM at 4 degrees Celsius for 10 minutes. The pellet was collected and resuspended in 50 ml of PBS. 1 μL of the 50 ml was then added to 10 ml of LB. 10 μL of the primary dilution was added to 300 μL of LB and plated on a 10cm LB-agar plate. The plates were incubated at 37 degrees Celsius overnight. The number of bacterial colonies were counted, and the colonies/ml determined. This was then used to determine the volume of the 50 mL stock bacteria to be used for brain infusion. The 50 ml stock bacteria was stored in 1x PBS with 10% glycerol at -80 degrees Celsius. *E. coli* cells were diluted into sterile aCSF and delivered ICV via osmotic pump (Alzet 1003D, rate 1 $\mu\text{L}/\text{hr}$) as detailed above for our model of PIH.

Measurement of CSF production rates

Rates of CSF production were measured using our published method,^{34,3} and as described here. Anesthetized rats were mounted in a stereotactic apparatus and a 1.3 mm burr hole was made over the left lateral ventricle (coordinates, $x = -0.8$, $y = +1.7$ relative to bregma). The mounted head was rotated on the ear-bars 90, nose-down, and the suboccipital muscles were dissected to the cisterna magna to expose the atlanto-occipital ligament. The ligament was punctured, and a 23-gauge flexible catheter (PE-20) was advanced 5 mm through the foramen of Magendie to the 4th ventricle. Sterile, molecular grade mineral oil (100 μL ; Sigma Aldrich, St. Louis, MO) was infused into the 4th ventricle to occlude the aqueduct of Sylvius, thereby creating a closed system of CSF circulation. With the rat in the same position, a glass capillary tube (cat # CV8010-300; borosilicate; OD, 1 mm; ID, 0.8 mm; length, 30 cm;

VitroCom, Mountain Lakes, NJ) was advanced through the burr hole into the right lateral ventricle (4.5 mm beyond entry). The volume (V) of CSF that had formed at a given timepoint was calculated as: $V (mm^3) = \pi \cdot r^2 \cdot d$, where r is the radius of the capillary tube and d is the distance CSF traveled within the capillary. Pictures were taken every 5 min over the course of 30 min. The rate of CSF formation ($\mu\text{L}/\text{min}$) could be calculated from the slope of the volume–time relationship.

Ventricular volume analysis

Ventricular volume analysis was performed as we previously published,³⁴ and as described here. Rats were transcardially perfused with 40 mL of ice-cold normal TBS (pH=7.60) followed by 40 mL of ice-cold 10% neutral buffered formalin (NBF; EMD Millipore Corporation). Brains were harvested and kept in 10% NBF overnight, then transferred to a 30% sucrose solution for cryoprotection. The brains were then removed, placed in Optimal Cutting Temperature Compound (OCT; Tissue-Tek, Sakura) for 1 hr at room temperature and frozen in dry ice. The mounted brains were kept at -80°C until transfer to the cryostat, then left 1 hr at -20°C . Brains were then serially sectioned in 25 μm sections). To prevent distortion from cryosectioning and slide mounting, we took high resolution pictures of serial coronal sections (200 μm apart, 14 levels) while the brain was mounted in the cryostat, using uniform parameters of camera positioning, magnification, and external lighting. Imaging software Gimp-2.10 was used to obtain a pixel count of the lateral ventricular and whole brain area of each section. A pixel to mm conversion factor was generated using the standard distance 22 mm sized block. Pixels were converted to area in mm^2 , summed over 14 levels and multiplied by the distance between levels (0.2 mm) to calculate ventricular and brain volume. The ventricular volume was divided by the brain volume to correct for varying brain size among animals.

ICV bumetanide delivery

As previously described,^{34,142} at the time of CSF collection prior to rotating the rat's head to a vertical orientation, a 28-gauge cannula from an Alzet brain infusion kit (#2; Durect) with a single spacer to adjust the depth to 4.5 mm, was stereotactically placed with a single spacer to adjust the depth to 4.5 mm into the burr hole over the left lateral ventricle (coordinates, $x = -0.8$, $y = +1.7$ relative to bregma) and secured to the skull with cyanoacrylate adhesive. The cannula was connected via a preloaded PE-20 catheter to a 1-ml syringe containing bumetanide (2.7 mM, pH 9; Sigma-Aldrich) diluted in aCSF (Harvard Apparatus). The syringe was loaded into a syringe infusion apparatus (Pump elite 11, Harvard Apparatus) and maintained at 37°C . To determine the rate of CSF formation during intraventricular drug infusion, the 'actual infusion rate' of the drug (1.93 $\mu\text{L}/\text{min}$) was subtracted from the 'measured outflow rate' to obtain the operational 'calculated rate of CSF formation'. To assess the effect of a drug, the baseline rate of CSF formation was determined during spontaneous CSF formation (no drug infusion), and the calculated rate of formation was then determined after infusion of bumetanide.

Systemic rapamycin administration

Rapamycin (6 mg/kg in normal saline, IP, Cayman) was administered IP 2-3hr prior to the start of IVH and LPS surgery. At 48h for IVH-treated rats and 72h for LPS-treated rats, rats were then either (i) euthanized and transcardially perfused with TBS (pH = 7.60) and 10% NBF and processed for ventriculomegaly or immunohistochemistry analysis as described above, or (ii) anesthetized for surgery to allow measurement of the rate of CSF secretion as described above.

ICV injection of Evans Blue Dye

Based on our previous methods to determine communication between the cerebral ventricles,³ Evans Blue Dye (Sigma Aldrich; 0.5% in sterile aCSF) was loaded into a 1 mL syringe (BD Syringe, Franklin Lakes, NJ) and connected to a cannula (Alzet; brain infusion and cannula kit, #2) using PE tubing. Anesthetized rats were mounted in a stereotactic apparatus and a 1.0 mm burr hole was made over the right lateral ventricle (coordinates, $x = -0.8$, $y = -1.7$ relative to bregma). The cannula was placed into the right lateral ventricle and dye was infused at a nominal rate of 2 $\mu\text{L}/\text{min}$ for 5 minutes with a syringe pump (Harvard Apparatus; Elite 11). Following infusion, the cannula remained in the ventricle for 30 minutes to prevent back flow and assure adequate circulation of the dye within the CSF spaces. Animals were then transcardially perfused with ice cold TBS (pH = 7.60), brains were harvested and immediately cut sagittally along the interhemispheric line. Images were taken to show the level of patency of the cerebral aqueduct.

CSF cytokine collection

48h after surgery for the PHH model or 72h following surgery for the PIH model, anesthetized rats were mounted in a stereotactic apparatus. The rat's head was rotated on the ear-bars 90, nose-down, and the suboccipital muscles were dissected to the cisterna magna to expose the atlanto-occipital ligament. The ligament was punctured using a 27G PrecisionGlide needle (BD, Franklin Lakes, NJ) attached to a 1 mL syringe (BD, Franklin Lakes, NJ) and inserted into the cisterna magna. CSF (~100 μL) was slowly withdrawn into a syringe and immediately transferred to a 1.5 mL Eppendorf tube on dry ice. Rats were immediately euthanized following CSF collection. Samples were stored at -80°C until shipment on dry ice to Eve Technologies (Calgary, CA) for analysis using their Rat Cytokine Array / Chemokine Array 27 Plex (RD27).

Rodent choroid plexus epithelium harvesting

Immediately following transcardial perfusion with ice cold TBS (pH = 7.60), the brain was isolated and placed in an ice-cold saline bath. Brains were cut sagittally along the interhemispheric line to expose the lateral ventricles, and choroid plexuses were rapidly but carefully dissected from both lateral ventricles using sharp forceps under magnification. Each brain yielded ~3 mg of choroid plexus tissue total, which was collected into a 1.5 mL tube, snap frozen in liquid nitrogen, and stored at -80°C until use.

Immunohistochemistry

Rats were transcardially perfused with ice-cold TBS followed by 10% NBF. Brains were dissected, kept in formalin overnight and dehydrated before paraffin embedding. 5-micron paraffin sections were rehydrated (briefly, slides were incubated in Xylene x10 min (x2), 100% ethanol x5 min (x2), then 95% ethanol x5 min (x2), then 70% ethanol (x1), then washed briefly in diH₂O) prior to antigen-retrieval at 95°C for 40 min using a citrate-based buffer (Retrieve-all system 1, Biolegend). After three TBST washes, the sections were incubated in blocking solution (5% donkey serum solution / TBST) for 1h at room temperature. The primary antibodies (diluted 1:200 in blocking solution) were incubated overnight at 4°C. After three TBST washes, secondary antibodies diluted 1:500 (Alexa Fluor 488, Alexa Fluor 555, Alexa Fluor 647; Invitrogen, Molecular probes) and DAPI (5 ug/ml, Biolegend) was added to the sections and incubated for 1 hour at room temperature and washed in TBST before mounting in Prolong Gold Antifade reagent (Invitrogen) and analysis by epifluorescence microscopy (Nikon Eclipse 90i, Nikon Instruments). The following antibodies were used: AQP1 (Abcam, Rabbit recombinant monoclonal, ab168387), ATP1A1 (Alomone, rabbit polyclonal, ANP-001), CD68 (CST, rabbit monoclonal, 97778), CLIC6 (Santa Cruz, mouse monoclonal, 365303), ED1/CD68 (Millipore, mouse monoclonal, MAB1435), IBA1 (Thermo, goat polyclonal, PA5-18039), KCNJ13 (Santa Cruz, mouse monoclonal 398810), Ki67 (CST, rabbit monoclonal 9129), pNKCC1 (Millipore, rabbit polyclonal, ABS 1004), pSPAK (Millipore, rabbit polyclonal, 07-2273), RELT (Novus, rabbit polyclonal, NBP2-56851), NKCC1 (CST, rabbit monoclonal, 85403S). Colocalization analysis was performed using the Fiji Coloc 2 plug-in.¹⁴³

Tissue dissociation and flow cytometry

Animals were anesthetized with Ketamine/Xylazine and transcardially perfused with ice cold TBS before brain removal. Choroid plexi from bilateral lateral ventricles were microdissected in ice cold HBSS and digested at 37°C for 20 min with Collagenases-I (10 U/mL) and -IV (400 U/mL) and DNaseI (30 U/mL) (this protocol was adapted from Van Hove et al⁶⁰). The cell suspension was blocked with CD16-CD32 antibodies and stained 30 min at 4°C with anti-rat CD45-PE/cy7, CD3-647 or corresponding isotype antibodies (Biolegend) and DAPI- co-stained to monitor cell viability. Cells were subsequently washed in FACS staining buffer (0.5% BSA, 2 mM EDTA in PBS without Calcium/Magnesium) and centrifuged at 350 rcf for 5 minutes. For FACS, cells were resuspended in 300ul of FACS buffer and sorted on a BD ARIA instrument, with gating and analysis by FlowJo software.

Antibodies for western blots

Primary antibodies used were: anti-WNK1 (University of Dundee, S079B), anti-SPAK (University of Dundee, S365D), anti-NKCC1 total antibody (University of Dundee, S022D), anti-Na(+)/K(+) ATPase alpha-1 (ATP1A1) antibody (DSHB, a5), anti-beta Actin antibody (Abcam, ab8227). Horseradish peroxidase-coupled (HRP) secondary antibodies used for immunoblotting were from Pierce. IgG used in control immunoprecipitation experiments was affinity-purified from pre-immune serum using Protein G-Sepharose.

Buffers for Western blots

Buffer A contained 50 mM Tris/HCl, pH 7.5 and 0.1 mM EGTA. Lysis buffer was 50 mM Tris/HCl, pH 7.5, 1 mM EGTA, 1 mM EDTA, 50 mM sodium fluoride, 5 mM sodium pyrophosphate, 1 mM sodium orthovanadate, 1% (w/v) NP40, 0.27 M sucrose, 0.1% (v/v) 2-mercaptoethanol, and protease inhibitors (complete protease inhibitor cocktail tablets, Roche, 1 tablet per 50 mL). TBS-Tween buffer (TTBS) was Tris/HCl, pH 7.5, 0.15 M NaCl and 0.2% (v/v) Tween-20. SDS sample buffer was 1X NuPAGE™ LDS Sample Buffer (NP0007, Invitrogen™), containing 1% (v/v) 2-mercaptoethanol. Protein concentrations were determined following centrifugation of the lysate at 16,000 x g at 4°C for 20 minutes using the using a Pierce™ Coomassie (Bradford) Protein Assay Kit (23200, Thermo Scientific) with bovine serum albumin as the standard.

Immunoblot and immunoprecipitation analyses

Rat choroid plexus lysates were subjected to immunoblot and immunoprecipitation as previously described,^{34,144} and is detailed here. Rat choroid plexus lysates (20 µg) were boiled at 75°C in sample buffer for 10 minutes, resolved by 7.5% sodium dodecyl sulfate polyacrylamide-gel electrophoresis and electrotransferred onto a polyvinylidene difluoride membrane. Membranes were incubated for 30 min with TBST (Tris-buffered saline, 0.05% Tween-20) containing 5% (w/v) skim milk. Blots were then washed three times with TBST and incubated for 1 h at room temperature with secondary HRP-conjugated antibodies diluted 5000-fold in 5% (w/v) skim milk in TBST. After repeating the washing steps, signals were detected with enhanced chemiluminescence reagent. Immunoblots were developed using ChemiDoc™ Imaging Systems (Bio-Rad, Feldkir). Figures were generated using Photoshop/Illustrator (Adobe).

SPAK was immunoprecipitated from rat choroid plexus lysates clarified by centrifugation at 16,000 x g at 4°C for 20 minutes, using SPAK antibody coupled to protein G-Sepharose^{34,144} at a ratio of 1 mg antibody per 1 mL beads. Clarified cell lysate (2 mg) was

incubated 2 h at 4°C with 15 µg of antibody conjugated to 15 µL of protein-G–Sepharose with gentle agitation. Beads were washed three times with 1 mL lysis buffer containing 0.15 M NaCl and twice with 1 mL buffer A. Bound proteins were eluted with 1X LDS sample buffer.

qPCR analysis

Microdissected tissues were snap frozen and stored at -80°C until total RNA was extracted using RNeasy Micro plus kit (Qiagen, 74034) and reverse transcribed (Biorad, 170-8890). Gene expression analysis was determined by quantitative reverse-transcription PCR (Bimake, B21202) using a CFX96 PCR machine (Bio-Rad). The qPCR primer sequences are provided in [Table S5](#). The data were expressed using the comparative threshold cycle (ΔCT) method (GOI, Gene Of Interest vs. Gapdh), and the mRNA ratios were given by $2^{-\Delta\text{CT}}$ compared to housekeeping genes. Gapdh expression was also compared to another housekeeping gene (Hprt1), as an additional control.

Bulk RNAseq

Full length high quality total cell RNA isolated by Qiagen RNeasy Micro RNA kit (Qiagen, <https://www.qiagen.com/us/shop/pcr/rneasy-micro-kit/>). ChP cells were homogenized in 350 µl RLT buffer with beta-mercaptoethanol in TissueLyzer for 10 min and proceed according to the instructions in RNeasy Micro RNA kit and RNAs was eluted in 18 µl dH₂O. 16 µl of elutant was recovered and 1.2 µl was used for the QC. Libraries were run on an Illumina HiSeq 2500 at the Yale Center for Genome Analysis. Expression level for each gene was estimated using Python program HTSeq.¹⁴⁵ Specifically, htseq-count function of HTSeq accumulated the number of aligned reads that falls under the exons of the gene. The R/Bioconductor package “DESeq2” was used to identify differentially expressed genes between cell populations derived from control, IVH-treated and LPS-treated rats.¹⁴⁶ Genes with a log₂-fold change expression greater than 3 and a q-value less than 0.01 were considered significant. The R ComplexHeatmap package was used to visualize the heatmap expression of highly variable genes.¹⁴⁷ Volcano plots were generated using the R package EnhancedVolcano.

scRNAseq sample preparation

Animals were anesthetized with Ketamine/Xylazine and transcardially perfused with ice cold TBS before brain removal. Choroid plexi from bilateral lateral ventricles were microdissected in ice cold HBSS with 30µM Actinomycin D (ActD, Sigma, cat#A1410) and digested at 37°C for 20 min with Collagenases-I and -IV (10 U/mL, 400 U/mL final, Worthington, Cat# LS004194, and LS004184) and DNase I (30 U/mL, Roche, cat# 04716728001) and ActD (3 µM) (this protocol was adapted from Van Hove et al.⁶⁰). For Flow sorting, the cell suspension was blocked with CD16-CD32 antibodies (1:100, biolegend, cat#101302) and stained 30 min at 4°C with anti-rat CD45-PE/cy7 (1:100, biolegend, cat#202207) to and DAPI (50 µg/mL). Cells were subsequently washed in FACS staining buffer (0.5% BSA, 2 mM EDTA in PBS without Calcium/Magnesium) and centrifuged at 350 rcf for 5 minutes. Cells were resuspended in 300 µl of FACS buffer and sorted by CD45 positivity on a BD ARIA instrument. CD45 positive and CD45 negative cells were collected in 0.4% BSA/PBS and 3 µM ActD and sent for 10X 3prime library preparation and sequencing at Yale Center for Genome Analysis.

Anesthesia and CM catheter placement

The rats were anesthetized with ketamine-xylazine (90 mg/kg bodyweight ketamine plus 7.5 mg/kg bodyweight xylazine, i.p.). After loss of righting reflex they breathed an Air:O₂ mix (1:1) spontaneously via a nose cone. Anesthesia was maintained with KX administered every 30 min via an IP catheter. When surgical plane anesthesia was assured by toe pinch before placing the rats in a stereotaxic frame. The dura above the cisterna magna (CM) was exposed and a small 5 mm copper tube (0.32 mm o.d., Nippon Tockushukan, MFG. CO., LTD, Tokyo, Japan) attached to a PE 10 microcatheter was positioned into the CSF compartment and secured in place using cyanoacrylate glue. After surgery, the rats were transferred to the MRI animal bed equipped with a heating waterbed and nose cone.

Magnetic resonance imaging (MRI)

All MRI acquisitions were performed on a Bruker 9.4T/16 magnet (Bruker BioSpin, Billerica MA) interfaced to an Avance III console controlled by Paravision 6.0 software. We used a 30-mm ID planar surface radiofrequency (RF) coil (Bruker BioSpin, Billerica, MA, USA) which was placed under the head of the rats for RF signal reception. A custom-made volume transmit RF coil designed with an internal diameter of 50 mm was used as RF signal transmitter. While in the MRI instrument, the supine rats breathed an Air:O₂ mix (1:1) spontaneously via a nose cone. Heart rate (HR) via oxygen saturation monitoring, respiratory rate and body temperature were continuously monitored (SA Instruments, Stony Brook, NY, USA). The body temperature was kept within ~ 37.0°C using a heated waterbed, and oxygen saturation was kept $\geq 97\%$ during the MRI experiments. **Brain morphometry:** A single flip angle spoiled gradient echo (SPGR) sequence was used to acquire 3D proton density weighted (PDW) MRIs: (repetition time (TR) = 50 ms, echo time (TE) = 4 ms, flip angle (FA) = 7°, Average = 2, field of view (FOV) = 30x30x15 mm, spatial resolution = 0.234x0.234x0.234 mm, scan time ~ 14 min. **Dynamic contrast enhanced MRI:** We acquired pre-contrast (baseline) T1-weighted images and post-contrast T1-weighted imaging of the whole brain. The 3D T1 weighted scans were acquired using a single flip angle spoiled gradient echo (SPGR) sequence: TR = 15ms, TE = 4ms, FA = 15°, Average = 2, FOV = 32x30x30 mm, the spatial resolution= 0.302x0.300x0.300 mm, acquisition time/scan = 5 min). After three baseline T1-weighted scans, 30 µL of 1:10 gadoteric acid (Gd-DOTA, DOTAREM,

Guerbert LLC, Carol Stream IL) diluted in sterile water was infused at a rate of 1.5 $\mu\text{L}/\text{min}$ into CSF through the CM catheter using an infusion pump for a total of 20 min. Post-contrast T1-weighted scans continued for a total 160 min.

Porcine choroid plexus epithelium harvesting

All porcine studies were performed in collaboration with the Dardik laboratory at Yale University and in compliance with federal guidelines and protocols approved by the Yale University Institutional Animal Care and Use Committee. Male Yorkshire pigs of ~ 48 kg and aged 3.4 months were euthanized via lethal injection of Euthasol (0.22 ml/kg).⁵⁶ Euthanized pigs were placed prone on the operating table for brain dissection. A semi-circular scalp incision was made around the vertex of the cranium, the skin was retracted, and the periosteum removed. Using an oscillating bone saw (Dremel Multi-max; Illinois, USA) a frontal craniectomy was performed to expose the underlying dura and cerebral hemispheres. The dura was excised at the midline to gain access to the superior sagittal sinus. The cerebral hemispheres were separated using surgical forceps and the lateral and third ventricles were exposed. The choroid plexus, identified as a highly vascular intraventricular structure, was carefully removed via forceps and placed into sterile saline on ice for molecular analysis.

Mass-spectrometry (MS) proteomics

Frozen pellets of ChP cells were lysed by sonication in RIPA buffer plus 1 \times PhosSTOP phosphatase inhibitor (Roche) and 1 \times cOmplete protease inhibitor cocktail (Roche). Protein (200 μg) for each sample underwent reduction, alkylation, and chloroform-methanol precipitation. Samples were resuspended in 100 mM TEAB (pH 8.5) and digested with trypsin (Promega, 1:50 w/w) overnight at 37°C. Digested samples were acidified and desalted on a C18 Macro Spin Column (The Nest Group). Peptides were eluted in 80% acetonitrile/0.1% trifluoroacetic acid (TFA), then dried by a SpeedVac. The dried peptide pellet from each sample was then TMT labeled according to manufacturer's protocol (Thermo Fisher Scientific) using a TMT10Plex Isobaric Labeling Reagent Kit (Cat#:90110). A label efficiency test was performed on 1/50th of each sample prior to equally mixing the 10 channels, then samples were dried prior to fractionation. Pooled TMT labeled peptides were then dissolved in buffer A and injected onto a Waters ACQUITY UPLC (BEH) C18 column (Waters XBridge BEH130 C18 3.5 μm 4.6 \times 250 mm) at a flow rate of 0.4 mL/min. An orthogonal high pH reverse phase separation was carried out using a Waters H-class UPLC system with Buffers (A:95% water/5% acetonitrile (ACN) with 10 mM ammonium acetate, pH 10; B: 5% water/95% acetonitrile (ACN) with 10 mM ammonium acetate, pH 10) were used to separate the peptides with a 60 min gradient 15% – 55% with buffer B. Total 60 fractions were collected. The fractions were then pooled into 8 fractions, dried and reconstituted in 0.1% formic acid.

Mass spectrometry data were obtained on an Orbitrap Fusion Tribrid Mass Spectrometer (ThermoFisher Scientific, San Jose, CA, USA) coupled to a nanoACQUITY UPLC system (Waters Corporation, Milford, MA, USA) in the Keck MS & Proteomics Resource at Yale University as described in Lee et al.,¹⁴⁸ and detailed here. Individual pooled fractions were loaded into a trapping column (nanoACQUITY UPLC Symmetry C18 Trap column, 180 μm \times 20 mm) and separated with a C18 column (nanoACQUITY column Peptide BEH C18, 75 μm \times 250 mm) at a flow rate of 5 $\mu\text{L}/\text{min}$. Peptides were eluted with a gradient from 6% to 20% mobile phase B over 120 min and then to 40% mobile phase B for another 45 min at a flow rate of 300 nL/min at a flowrate of 300 nL/min with buffers (A: 0.1% formic acid in water and B: 0.1% formic acid in acetonitrile). The data were acquired with data-dependent mode with multinotch synchronous precursor selection (SPS)-MS3 scanning for TMT tags as described previously.¹⁴⁹ The ions above with an intensity threshold of 5000 was selected for collision-induced dissociation (CID)-MS fragmentation. The top 10 fragment ions for each peptide MS2 were notched out and co-fragmented with higher-energy collision dissociation (HCD) to produce MS3 scans and were analyzed in the Orbitrap at a resolution of 60,000.

The proteomics raw data files were processed and quantified by MaxQuant (<https://maxquant.net/maxquant/>) version 1.6.1.0 with Andromeda search engine using the Rat UniProt FASTA database (<http://coxdocs.org/doku.php?id=maxquant:andromeda:start>). Default value of parameters were used in Maxquant unless explicitly stated. Briefly, false-discovery rate (FDR) was set at 1% for proteins and peptides respectively and match between runs was enabled with a default time window of 0.7 min. Search results (TMT reporter ion intensities) were exported as text files. The differentially expressed proteins were identified using the Perseus framework (<https://maxquant.net/perseus/>). Proteins with a \log_2 -fold change expression greater than 1 and a q-value less than 0.05 were considered significant. The R ComplexHeatmap package was used to visualize the heatmap expression of highly variable genes.¹⁴⁷

SPAK Immunoprecipitation for LC-MS/MS

ChP cells were lysed in a lysis buffer containing protease and phosphatase inhibitor by incubating 10 min on ice and then centrifuged at 18,000 g for 5 min at 4°C. Supernatants containing the proteins were first precleared with Protein G beads for 30 min at 4°C and then were split in half and transferred into two clean 1.5 mL Eppendorf tubes. One half of the supernatant was incubated with Protein G beads only (IgG) as control for non-specific binding; the other half of the supernatant was incubated with Protein G beads + anti-SPAK 1°Ab. Incubation with gentle agitation was conducted at 4°C for overnight. Supernatant was removed and beads were washed 4 times with RIPA containing 150 mM NaCl. Bound proteins were then eluted twice with 2 M urea (for in-solution trypsin digestion) or SDS sample buffer for 5 minutes (In-gel trypsin digestion). The elutions of SDS samples buffer were then loaded onto a mini SDS PAGE gel (4-12%, Bio-Rad Laboratories, Hercules, CA). Gel bands/plugs were excised and processed for LCMS/MS analysis.¹⁵⁰ Gel bands/plugs were first cut into small pieces and subjected to the following washes with agitation: 50% (v/v) acetonitrile (5 min), 50% (v/v) acetonitrile/10 mM NH_4HCO_3 (30 min). Gel pieces were dried with a SpeedVac, resuspended in 30 μL

of 10 mM NH_4HCO_3 /0.2 μg digestion grade trypsin (Promega), and incubated for 16 h at 37 °C. Peptides were then acidified with 0.1% (v/v) trifluoroacetic acid (TFA) prior to LC MS/MS analysis on an Orbitrap Fusion mass spectrometer coupled to a nanoACQUITY UPLC¹⁴⁰ located within the Keck MS & Proteomics Resource at Yale.

QUANTIFICATION AND STATISTICAL ANALYSIS

Data analysis

Statistical analysis of CSF secretion, CSF cytokine analysis, ventriculomegaly, and IHC quantification used Prism (GraphPad, San Diego, CA) for one-way ANOVA analysis with Tukey's multiple comparisons, unpaired t-test, or paired t-test. Transcriptomic and proteomic data was analyzed using RStudio (RStudio Inc., Boston, MA). Non-parametric Wilcoxon rank sum test was used to determine statistically significant gene markers in scRNAseq datasets. Numerical data in text and figures are presented as mean \pm standard error of the mean (SE). Rates ($\mu\text{L}/\text{min}$) were calculated as the slope of the volume-time relationship, based on data collected over 20 min or more. Rates were determined for individual animals and averaged across individuals. Sample size calculations were based on two previous studies that used the same model of IVH³⁴ and method for measuring rates of CSF production.^{34,3} The statistical details of each experiment can be found in the figures and corresponding figure legends (including the specific statistical test used, value of n and what each n represents, and the dispersion and precision measures used), except for the scRNAseq datasets. Details for the specific analysis used for the scRNAseq datasets are detailed in the [method details](#) of the [STAR Methods](#) section. Any additional information can be addressed via contact with the corresponding article of this manuscript.

snRNA-seq rat ChP data analysis

As described previously,⁶ the preprocessing and clustering analysis for snRNA mouse choroid plexus cell dataset was completed using Seurat.¹⁴¹ For each nucleus, the number of genes for which there was at least one mapped read, was quantified, and then all nuclei with fewer than 500 detected genes were excluded. Furthermore, all nuclei with more than 10% of total UMI's mapped to mitochondrial genes were excluded. Genes detected in fewer than 10 nuclei were excluded. Expression values $E_{i,j}$ for gene i in nucleus j were calculated by dividing UMI counts for gene i by the sum of the UMI counts in nucleus j , to normalize for differences in coverage, and then multiplying by 10,000 to create TPM-like values (TP10K), and finally computing $\log_2(\text{TP10K} + 1)$.

Selection of variable genes was performed by fitting a logistic regression model to the cellular detection fraction (often referred to as α), using the total number of UMIs per cell/nucleus as a predictor, as in Montoro et al. (2018).¹⁵¹ Outliers from this curve are genes expressed in a lower fraction of cells/nuclei than would be expected, given the total number of UMIs mapping to that gene; that is, likely cell-type or state-specific genes. A threshold of deviance between < -0.15 and < -0.3 was used.

The expression matrix was restricted to the subsets of variable genes and high-quality cells/nuclei noted above. Values were then centered and scaled before inputting them into principal component analysis (PCA) implemented using 'RunPCA' in Seurat, which runs the `irlba` function. For the snRNA-seq data, which included mixed sexes, Y chromosome and X-inactivation genes (`Xist`, `Tsix`) were removed from the variable genes prior to running PCA. The cell embeddings were either the singular vectors themselves or the singular vectors multiplied with the singular values depending on the cell type. After PCA, significant principal components were identified using the elbow-method, when looking at the distribution of singular values. Scores from only those significant principal components were used as the input to further analysis. To embed cells in a graph structure, first a KNN graph was constructed based on the euclidean distance in PCA space, and the edge weights were refined between any two cells based on the shared overlap in their local neighborhoods (Jaccard similarity). This step was performed using the `FindNeighbors` (`reduction='pca'`, `dims=1:50`) command by taking the first 50 principal components as input. To cluster the cells in an unsupervised fashion, the Louvain algorithm (default) was applied to iteratively group cells together, with the goal of optimizing the standard modularity function. The `FindClusters` function (`resolution = 0.5`) was implemented for this procedure. For visualization purposes, the dimensionality of the datasets was further reduced to 2D embeddings using UMAP on the significant PCs via `RunUMAP()` functions of the Seurat package in R.¹⁵² Non-parametric Wilcoxon rank sum test was used to identify differentially expressed markers across all clusters by running `FindAllMarkers(dataset, only.pos = TRUE, min.pct = 0.25, logfc.threshold = 0.25)`. `VlnPlot()`, which shows expression probability distributions across clusters, and `FeaturePlot()`, which visualizes feature expression on a UMAP plot, were used to visualize key genes differentially expressed for individual clusters. Adult epithelial cells were isolated and further sub-clustered in an unsupervised fashion using the Louvain algorithm.

Nucleus doublets were identified using the R package `DoubletFinder` (version `DoubletFinder_2.0.2`).¹⁵³ Briefly, artificial doublets are generated from the data, and for each real data point the fraction of artificial doublets of the nearest neighbors in a latent space is computed. If this fraction is above a certain cutoff, the data point is a doublet. Doublets were calculated for each sample separately after initial data filtering by genes detected and mitochondrial gene expression as per instructions. For each sample, an optimal `pK` (defines the PC neighborhood size) was chosen by computing a parameter sweep (`paramSweep_v3` function), and a `pK` was chosen that maximized the `BCmvn` (mean variance-normalized bimodality coefficient). Doublets were then calculated using the function `doubletFinder_v3()` with parameters; `PCs = 1:30`, `pN = 0.25`, `nEXP = 15%` of cells in the sample, and removed from downstream analysis.

PIH and PHH rat ChP scRNAseq datasets

The preprocessing and clustering analysis for scRNA rat choroid plexus CD45⁺ and CD45⁻ cell datasets for was completed using Seurat.¹⁴¹ Cells with low numbers of genes (200), low numbers of UMIs (500) or high numbers of UMIs (>10000) and mitochondrial gene percentage greater than 10% were removed. The normalization and initial feature selection for each of the six datasets (control, IVH-treated, LPS-treated conditions for CD45⁺ and CD45⁻ cells) were completed individually. The filtered matrices were normalized using 'LogNormalize' methods in Seurat using a size factor of 10,000 molecules for each cell. 2,000 most variable genes were identified by variance stabilizing transformation for each dataset by implementing the FindVariableFeatures function in Seurat v4 (selection.method = "vst"). The experimental conditions were integrated using Seurat's integration pipeline for CD45⁺ and CD45⁻ cell datasets. For integration, 2,000 shared highly variable genes were identified using Seurat's 'SelectIntegrationFeatures()' function. Integration anchors were identified based on these genes using canonical correlation analysis using the 'FindIntegrationAnchors()' function. The data were then integrated using 'IntegrateData()' and scaled again using 'ScaleData()'. Overall, integrated CD45⁺ dataset consisted of 1427 control, 3331 IVH-treated and 5529 LPS-treated cells whereas integrated CD45⁻ dataset consisted of 2036 control, 718 IVH-treated and 1603 LPS-treated cells.

Principal component analysis (PCA) and uniform manifold approximation and projection (UMAP) dimension reduction with 50 principal components were performed. A KNN graph was constructed based on the euclidean distance in PCA space to embed cells in a graph structure, and the edge weights were refined between any two cells based on the shared overlap in their local neighborhoods (Jaccard similarity). This step was performed using the FindNeighbors command (reduction='pca', dims=1:50) by taking the first 50 principal components as input. To cluster the cells in an unsupervised fashion, the Louvain algorithm (default) was applied to iteratively group cells together, with the goal of optimizing the standard modularity function. The FindClusters function (resolution=0.4) was implemented for this procedure. For visualization purposes, the dimensionality of the datasets was further reduced to 2D embeddings using UMAP on the significant PCs via RunUMAP() functions of the Seurat package in R.¹⁵² Non-parametric Wilcoxon rank sum test was used to identify differentially expressed markers across all clusters by running FindAllMarkers(dataset, only.pos = TRUE, min.pct = 0.25, logfc.threshold = 0.25). Further sub-clustering of certain cell populations including myeloid cells, T-cells, epithelial cells was conducted in an unsupervised fashion using the Louvain algorithm. The R ComplexHeatmap package was used to visualize the heatmap expression of highly variable genes.¹⁴⁷ VlnPlot, FeaturePlot and DotPlot functions were used to visualize the gene expression profiles across clusters and conditions

To infer cell-cell interactions based on the expression of known ligand-receptor pairs in different cell types, CellChat was applied to our experimental conditions after merging CD45⁺ and CD45⁻ for each condition. The official workflow and databases were implemented. Briefly, the normalized counts were loaded into CellChat, after which the preprocessing functions identifyOverExpressedGenes, identifyOverExpressedInteractions and projectData with standard parameters set were applied to our datasets. The main analyses were conducted using the functions computeCommunProb, computeCommunProbPathway and aggregateNet with fixed randomization seeds.

ScRNA-seq mouse ChP immune cell data analysis

As described previously,⁶ the preprocessing and clustering analysis for ScRNA mouse choroid plexus immune cell dataset was completed using Seurat.¹⁴¹ Outlier cells were first identified based on three metrics (library size, number of expressed genes and mitochondrial proportion); cells were tagged as outliers when they were four median absolute deviations distant from the median value of each metric across all cells. Secondly, a principal component analysis plot was generated based on the following metrics: 'pct_counts_in_top_100_features', 'total_features_by_counts', 'pct_counts_feature_control', 'total_features_by_counts_feature_control', 'log10_total_counts_endogenous' and 'log10_total_counts_feature_control'. Outlier cells in this principal component analysis plot were identified using the R package mvoutlier. Low-abundance genes were removed using the 'calcAverage' function and the proposed workflow. The raw counts were normalized and log₂-transformed by first calculating 'size factors' that represented the extent to which counts should be scaled in each library. Highly variable genes were detected using the proposed workflow of the scran R package and by applying false discovery rate ≤ 0.05 and var.out\$bio ≥ 0.01 as cutoffs. Highly variable genes were subsequently used for unsupervised dimensionality reduction techniques and principal component analysis.

To embed cells in a graph structure, first a KNN graph was constructed based on the euclidean distance in PCA space, and the edge weights were refined between any two cells based on the shared overlap in their local neighborhoods (Jaccard similarity). This step was performed using the FindNeighbors (reduction='pca', dims=1:50) command by taking the first 50 principal components as input. To cluster the cells in an unsupervised fashion, the Louvain algorithm (default) was applied to iteratively group cells together, with the goal of optimizing the standard modularity function. The FindClusters (resolution=0.5) function was implemented for this procedure. For visualization purposes, the dimensionality of the datasets was further reduced to 2D embeddings using UMAP on the significant PCs via RunUMAP() functions of the Seurat package in R¹⁵². Non-parametric Wilcoxon rank sum test was used to identify differentially expressed markers across all clusters by running FindAllMarkers (dataset, only.pos = TRUE, min.pct = 0.25, logfc.threshold = 0.25). VlnPlot(), which shows expression probability distributions across clusters, and FeaturePlot(), which visualizes feature expression on a UMAP plot) were used to visualize key genes differentially expressed for individual clusters.

Induction of immediate early genes (IEGs) was observed in some of the choroid plexus cells in which two clearly separated macrophage clusters differed only in expression of IEGs and heat shock proteins. These differentially expressed genes closely resembled those identified in a subset of muscle satellite cells and shown to be dissociation-induced genes. Single-cell isolation using either a

standard or ActDmodified protocol was compared to confirm that the IEGs induced in our clusters were also dissociation-induced. This allowed us to identify 224 genes that were upregulated in standard versus ActD samples in Choroid Plexus Border-Associated Macrophages, comprising the dissociation-induced gene list. To correct for dissociation-induced gene expression, which may mask biologically relevant results, this gene list was used to detect cells that were 'dissociation-affected' by plotting expression of all these genes over all cells. The corresponding histogram revealed a clear cutoff that split the cells between 'dissociation-affected' and '-un-affected' cells. This information was added to the metadata attribute of the Seurat object, and this unwanted source of variation was subsequently removed using the 'Regress out' function of the Seurat R package.

Gene co-expression network creation

The gene co-expression modules for the preprocessed and clustered choroid plexus dataset were constructed by using Monocle3's differential expression analysis pipeline.¹⁵⁴ Monocle3's `graph_test` (`neighbor_graph="knn"`) function was used to identify genes that vary between groups of cells in UMAP space. This function employs a statistic from spatial autocorrelation analysis called Moran's I, which Cao et al. showed to be effective in finding genes that vary in single-cell RNA-seq datasets.¹⁵⁴ Genes with FDR-adjusted p-values of less than 0.05 were used to construct gene co-expression networks via UMAP and community analyses. 21 gene modules were created using this pipeline.

Hypergeometric enrichment test analysis

Module gene lists were obtained via Monocle3 as described above. Hypergeometric enrichment analysis was conducted using the R package `hyper`.¹⁵⁵ Syndromic and non-syndromic gene lists for both high confidence and probable genes were used to find modules enriched with Craniosynostosis-related genes. Modules with FDR adjusted p-values less than 0.05 were considered significant.

Cluster abundance analysis

In order to test the difference in cell counts for IVH-treated and LPS-treated ChP compared to control, we used beta-binomial generalized linear model in package `aod::betabin` for both CD45⁺ and CD45⁻ clustering. In our generalized linear model, we set the count of the cell type of interest and the total count of cells of each experimental condition to be the response variable and the experimental condition of the cells to be the independent variable. We tested for Pearson's correlation between the frequency of each cell cluster. We adjusted the p value threshold using Bonferroni correction ($0.05/32 = 0.00156$ for CD45⁺ dataset and $0.05/20 = 0.0025$ for CD45⁻ dataset).

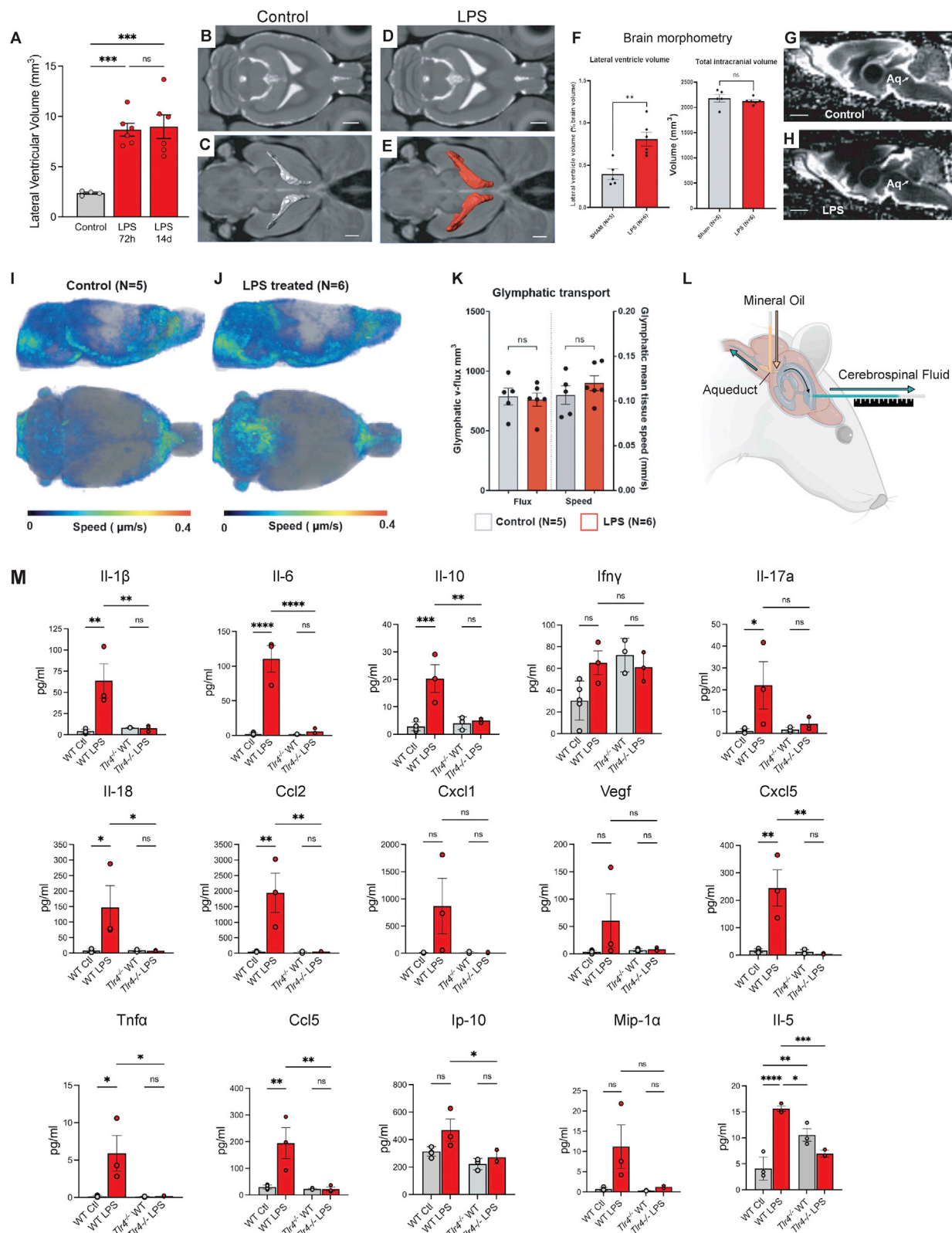
Gene Ontology enrichment analysis

The gene and protein lists for differentially expressed genes and proteins for IVH and LPS conditions from the RNAseq and proteomics experiments, as well as the modules significantly enriched with these genes/proteins, were further studied for gene ontology, pathway and upstream transcription factor enrichment using the `Enrichr` R package.¹⁵⁶ The `Enrichr` contains a diverse and up-to-date collection of over 100 gene set libraries available for analysis and download. The databases for these analyses include gene ontologies (biological processes, cellular components, and molecular functions), biological pathways (Wiki pathways Human and Mouse) and upstream transcription factors (`TRANSFAC` and `JASPAR`). Adjusted p-value of less than 0.05 was considered significant, and combined Z-score was used for ranking.

MRI data analysis

Morphometry of CSF and brain parenchymal volumes (grey matter + white matter) was performed for each rat as previously described. Briefly, The 3D PDW images were corrected for intensity inhomogeneity using the N4 bias field correction algorithm,¹⁵⁷ and then segmented into grey matter (GM), white matter (WM) and CSF brain compartments to calculate their brain parenchymal (GM+WM) and CSF volumes. All the spatial segmentations were performed on SPM12 (<http://www.fil.ion.ucl.ac.uk/spm>) software package platform, using our previously custom-made tissue probability maps.¹⁵⁸ The tissue probability maps generated by segmentation of the individual rat brains were thresholded at 0.5, yielding GM, WM, and CSF binary masks in native space. Spatially normalized average CSF compartment volume maps of the sham controls (N=5) and LPS treated (N=6) rats were subsequently created. In addition to SPM analysis, for each rat manual segmentation of the lateral ventricle volume was performed on the PWD and T1-weighted baseline MRIs using PMOD (PMOD, version 3.908, PMOD Technologies LLC, Zürich, Switzerland). Analysis of DCE-MRI data included correction for head motion, followed by intensity normalization, smoothing, and then voxel-wise percent signal change to baseline was calculated using SPM12 (<https://www.fil.ion.ucl.ac.uk/spm/>).¹⁵⁹ The 'percent signal change from baseline images' was then used for optimal mass transport (rOMT) analysis.⁵⁰ From each rat's whole brain DCE-MRI data series the rOMT analysis produced whole brain binary pathlines endowed with solute speed (representing the local speed and spatial distribution of the pathline networks) from which lymphatic flux and mean tissue solute speed were derived.⁵⁰

Supplemental figures



(legend on next page)

Figure S1. LPS mediates acute and chronic ventriculomegaly, with preserved patency of the cerebral aqueduct and glymphatic transport, and increases cytokine/chemokine expression, related to Figure 1

(A) Quantification of lateral ventricular volume at 72 h and 14 days after an initial 72 h infusion of aCSF (control) or LPS. Volume calculated using sequential slices through entire lateral ventricular system (n = 5–6 animals per condition).

(B–H) Spatially normalized population averaged CSF probability maps overlaid on proton density weighted anatomical MRI brain images of live, anesthetized animals treated with aCSF (control) (B and C) or LPS (D and E). CSF filled ventricles are represented as high intensity signal areas. Top panels (B and D) show MRI images (axial plane view) at the level of the lateral ventricles obtained from voxel-wise morphometric analysis of the CSF compartment, and bottom panels (C and E) show the corresponding 3D volume reconstructions of the lateral ventricles.

(F) Morphometric quantification of the lateral ventricular volume (% brain volume) and total intracranial volume (mm³) for control (sham) and LPS-treated PIH animals.

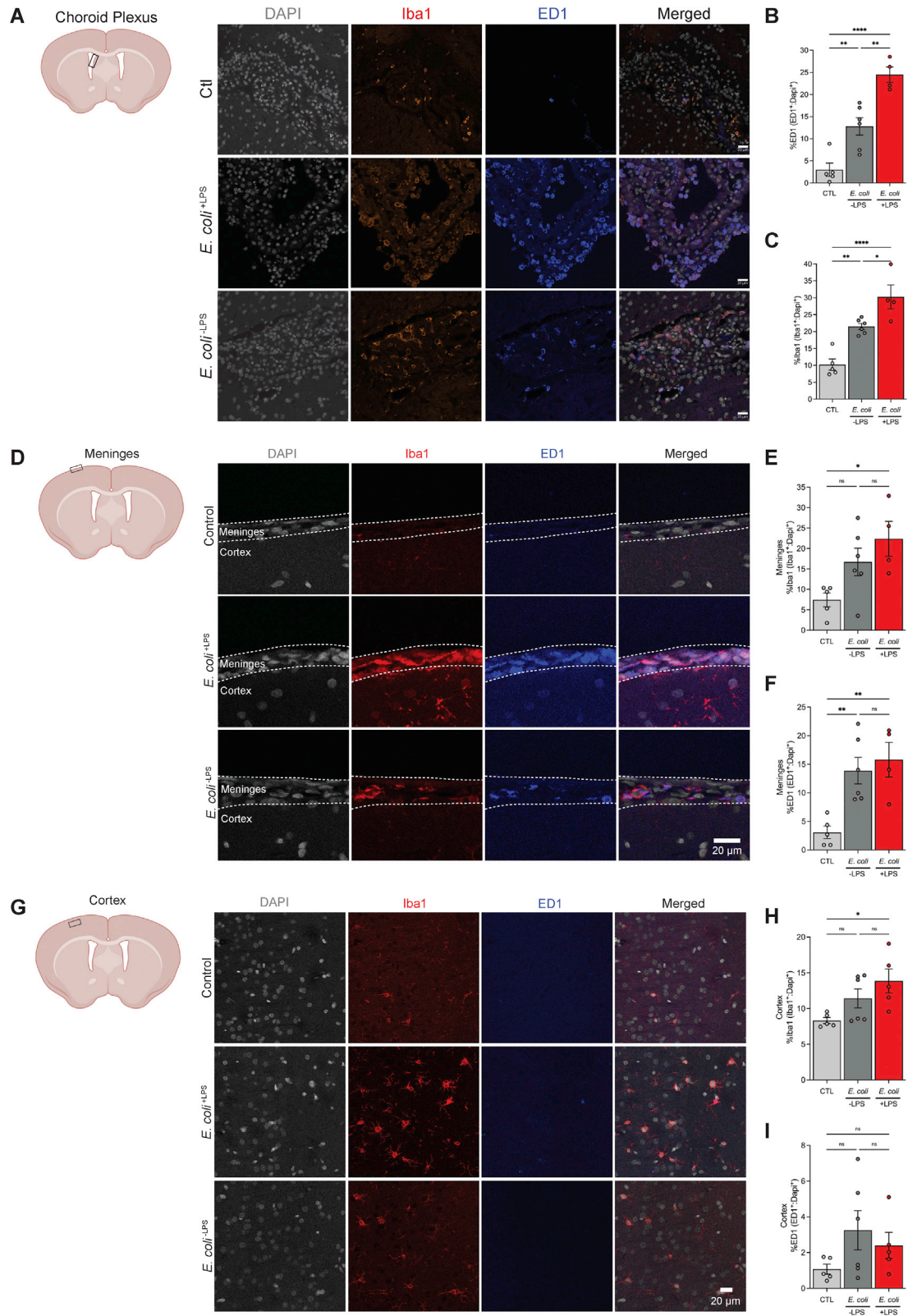
(G and H) CSF contrast-enhanced T1-weighted MRI images (sagittal plane view) of live, anesthetized animals demonstrating patency of the cerebral aqueduct (Aq) in control (G) and PIH animals (H).

(I and J) Average glymphatic flux with superimposed color-coded solute speed maps (μm/s) for control (I) and LPS-treated PIH animals (J). Representative speed maps demonstrating glymphatic transport in sagittal (top panels) and axial (bottom panels) MRI view planes.

(K) Quantification of glymphatic transport metrics including glymphatic v-flux (mm³) and glymphatic mean tissue speed (mm/s).

(L) Schematic illustrating *in vivo* CSF secretion measurements. Mineral oil is administered into the cerebral aqueduct (aqueduct) through a catheter (yellow line and arrow) inserted into the aqueduct, which blocks flow of CSF. A glass capillary tube is then placed through a burr hole in the skull into the lateral ventricle (blue line and arrow). The distance of CSF flow through the capillary tube is measured using a ruler (black) and rate is calculated over time.

(M) CSF cytokine/chemokine expression (from Figure 2) concentrations (from Figure 2, pg/mL) of IL-1b, IL-6, IL-10, IFN γ , IL-17a, IL-18, CCL2, CXCL1, VEGF, CXCL5, TNF α , CCL5, IL-10, MIP-1 α , and IL-5 in Ctl and 72 h LPS-treated *Tlr4*^{+/+} and *Tlr4*^{-/-} rats. For all experimental conditions, n = 4–6 animals per condition. *p < 0.05, **p < 0.01, ***p < 0.001, ****p < 0.0001, ns = not significant, by one-way ANOVA (A) and unpaired t test with Welch correction (K).



(legend on next page)

Figure S2. Choroid plexus, meningeal, and cortical immune reaction in PIH animals treated with *E. coli*^{+LPS}, related to Figure 2

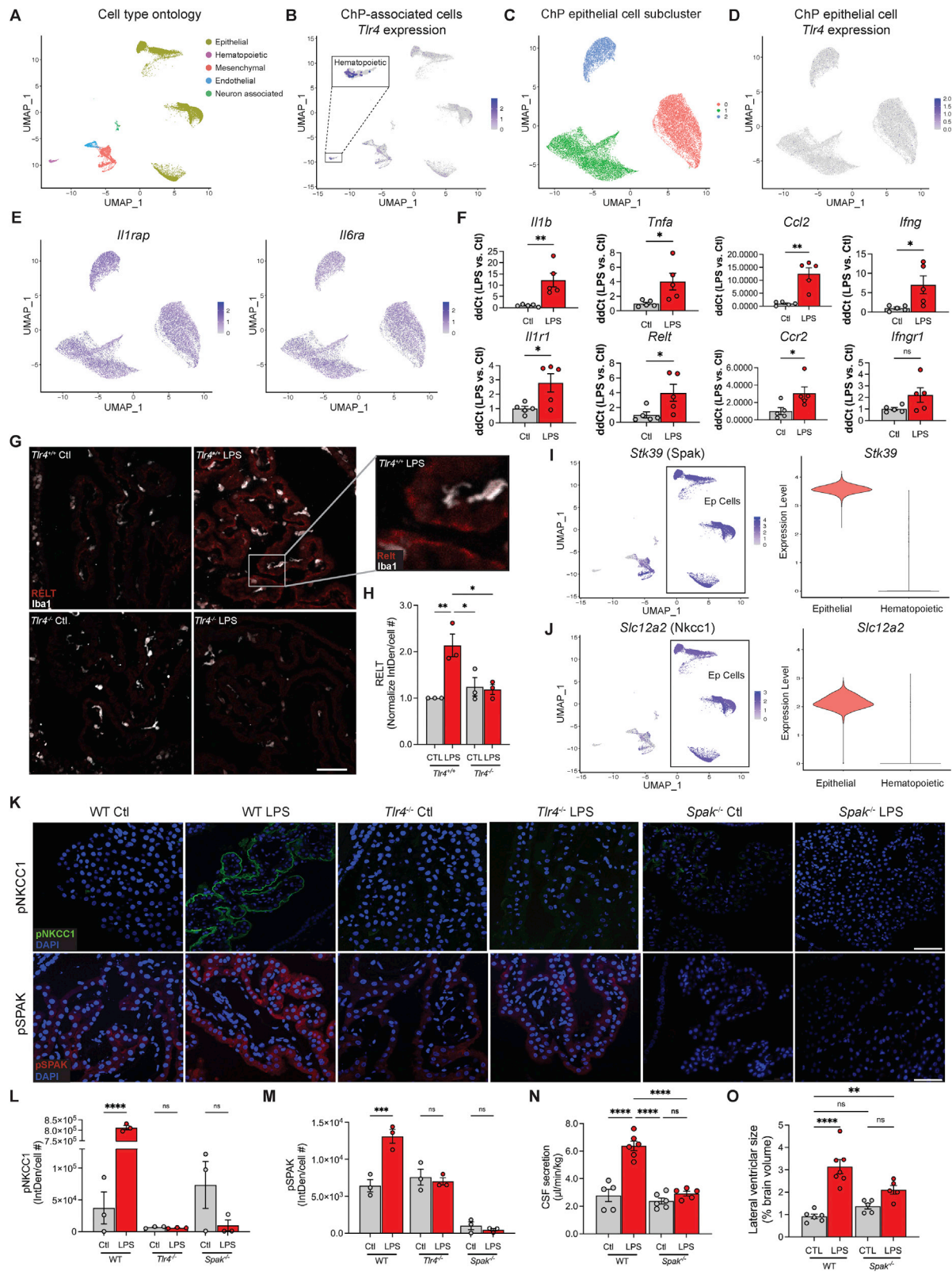
(A) Illustration of a representative coronal brain slice (left panel) indicating location of the ChP (black box) imaged for analysis. Representative IHC (right panel) of Iba1⁺ (red) and ED1⁺ (blue) positive cells in Ctl and *E. coli*^{+/-LPS} rat ChP in single-channel IHC (Dapi, white), as well as merged images. (B and C) Quantification of (A) showing DAPI-normalized % ED1⁺ (B) and Iba1⁺ (C) cells.

(D) Illustration of a representative coronal brain slice (left panel) indicating location of the meninges (black box) imaged for analysis. Representative IHC of Iba1⁺ (red) and ED1⁺ (blue) positive cells in Ctl and *E. coli*^{+/-LPS} rat meninges in single-channel IHC (Dapi, white), as well as merged images.

(E and F) Quantification of (D) showing DAPI-normalized % Iba⁺ (E) and ED1⁺ (F) cells.

(G) Illustration of a representative coronal brain slice (left panel) indicating location of the cortex (black box) imaged for analysis. Representative IHC of Iba1⁺ (red) and ED1⁺ (blue) positive cells in Ctl and *E. coli*^{+/-LPS} rat meninges in single-channel IHC (Dapi, white), as well as merged images.

(H and I) Quantification of (G) showing DAPI-normalized % Iba⁺ (H) and ED1⁺ (I) cells. Scale bars, 20 μ m; n = 4–6 animals per condition. Error bars, mean \pm SEM; each symbol represents one animal. *p < 0.05, **p < 0.01, ****p < 0.0001, by one-way ANOVA.



(legend on next page)

Figure S3. SPAK kinase transduces pro-inflammatory CSF signals in ChP epithelial cells to stimulate NKCC1-dependent CSF secretion, related to Figure 2

(A) UMAP of single-nucleus transcript profiles of adult ChP-associated cells,⁶ colored by cell type.
 (B) *Tlr4* expression in ChP-associated cells (avg. log₂FC = 1.0; p = 5.14e-214).
 (C–E) (C) UMAP of ChP epithelial cell subclusters, colored by group and by expression of (D) *Tlr4*, (E, left) interleukin-1 receptor accessory protein (*Il1rap*) (avg log₂FC = 0.96, p < 10e-300), and (E, right) interleukin 6 receptor (*Il6ra*) (avg log₂FC = 0.23, p = 1.87e-211).
 (F) Quantitative PCR (qPCR) delta-delta CT (ddCT) of mRNA products of cytokine genes *Il1b*, *Tnfa*, *Mcp1*, *Ifng*, and the genes encoding their receptors *Il1r1*, *Relt*, *Ccr2*, *Ifngr1* (n = 5 animals per condition; see Table S5*).
 (G) Representative IHC of ChP TNF receptor RELT (red) and Iba1 (white) in *Tlr4*^{+/+} and *Tlr4*^{-/-} Ctl and LPS-treated animals (inset, 4× magnification).
 (H) Quantitation of (G) (normalized intensity density [IntDen]/cell #) (n = 6 ChP per genotype, 3 animals per condition).
 (I and J) (I) UMAP of cell ontology (left, as in A and violin plots [right] showing expression of *Stk39* (avg. log₂FC = 1.1, p < 10e-300; Epithelial, avg. log₂FC = 4.46, p = 4.22e-233) and (J) *Slc12a2* (avg. log₂FC = 1.3, p < 10e-300; Epithelial, avg. log₂FC = 2.70, p = 8.15e-215).
 (K–M) (K) Representative IHC of phospho-activated NKCC1 (pNKCC1; green, top row) and phospho-activated SPAK (pSPAK; red, bottom row) in Ctl and LPS-treated WT, *Tlr4*^{-/-} and *Spak*^{-/-} rats. Quantitation (interval density/cell #) of (L) pNKCC1 and (M) pSPAK from (K) (n = 6 ChP per genotype, 3 animals per condition).
 (N) Body weight-normalized CSF secretion rate (μL/min/kg) and (O) lateral ventricular size (% brain volume) in *Spak*^{+/+} Ctl, *Spak*^{+/+} LPS, *Spak*^{-/-} Ctl, and *Spak*^{-/-} LPS rats (n = 5–6 animals per condition). Scale bars, 25 μm. Error bars, mean ± SEM; each symbol represents one animal. *p < 0.05, **p < 0.01, ***p < 0.001, ****p < 0.0001, ns = not significant; (F) unpaired t test; (H and L–O) one-way ANOVA.

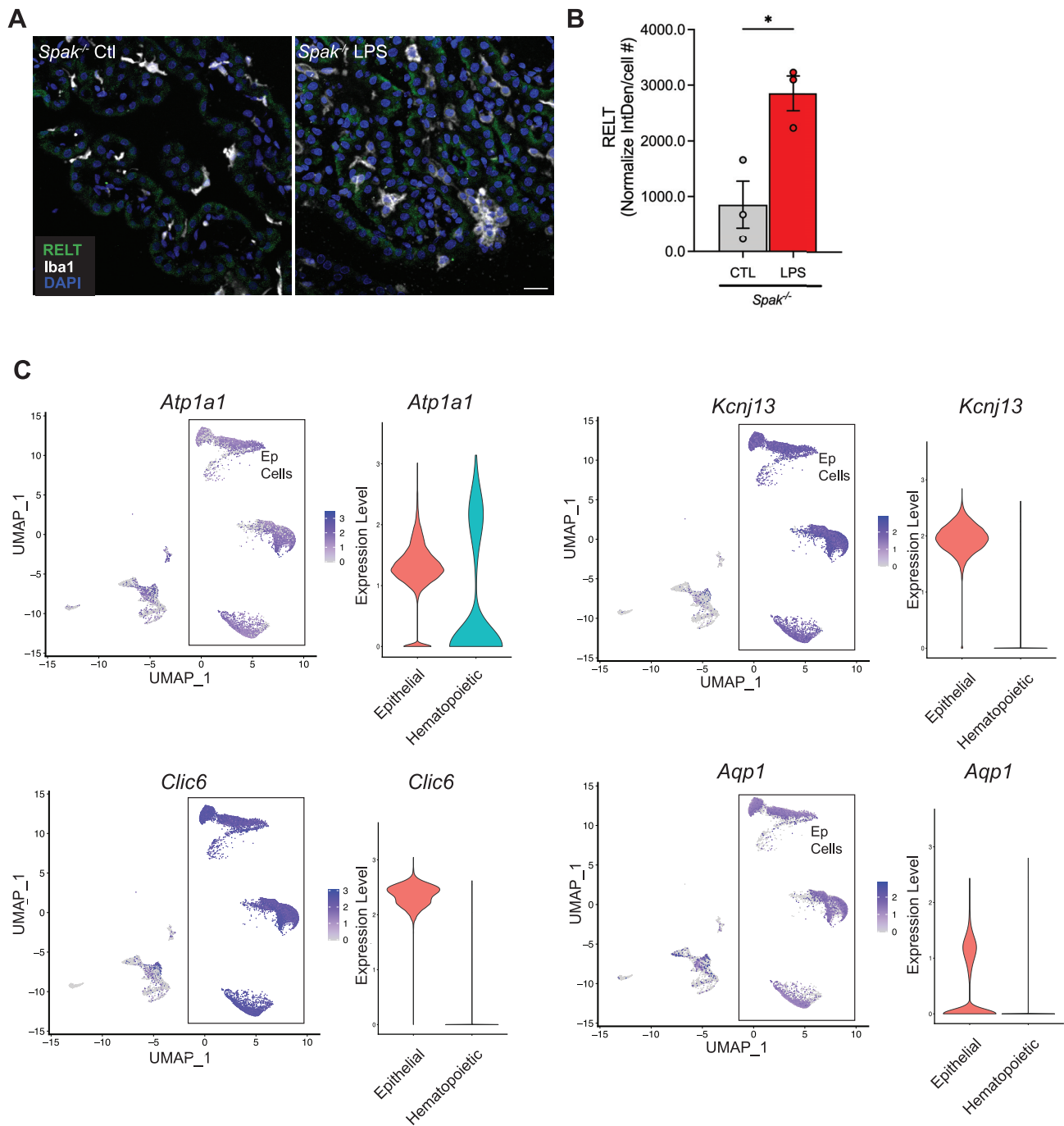


Figure S4. RELT expression in *Spak* KO rats and ChP expression of *Atp1a1*, *Kcnj13*, *Clic6*, and *Aqp1*, related to Figures 2 and 3

(A and B) (A) Representative IHC of Relt (green) and Iba1 (white) in *Spak*^{-/-} Ctl and LPS-treated animals (DAPI, blue) and (B) Quantitation of Relt expression (normalized intensity density (IntDen)/cell #) of *Spak*^{-/-} Ctl and LPS (n = 6 ChP, 3 animals for all conditions). *p < 0.05. Error bars show mean ± SEM, and each symbol represents average data obtained from an individual animal.

(C and D) Expression analysis of SPAK-interacting proteins in the ChP. UMAP of cell ontology (as in Figure S3A, left panels) and violin plots (right panels) of cellular expression of (A) *Atp1a1*, (B) *Kcnj13*, (C) *Clic6*, and (D) *Aqp1* in epithelial and hematopoietic cells.

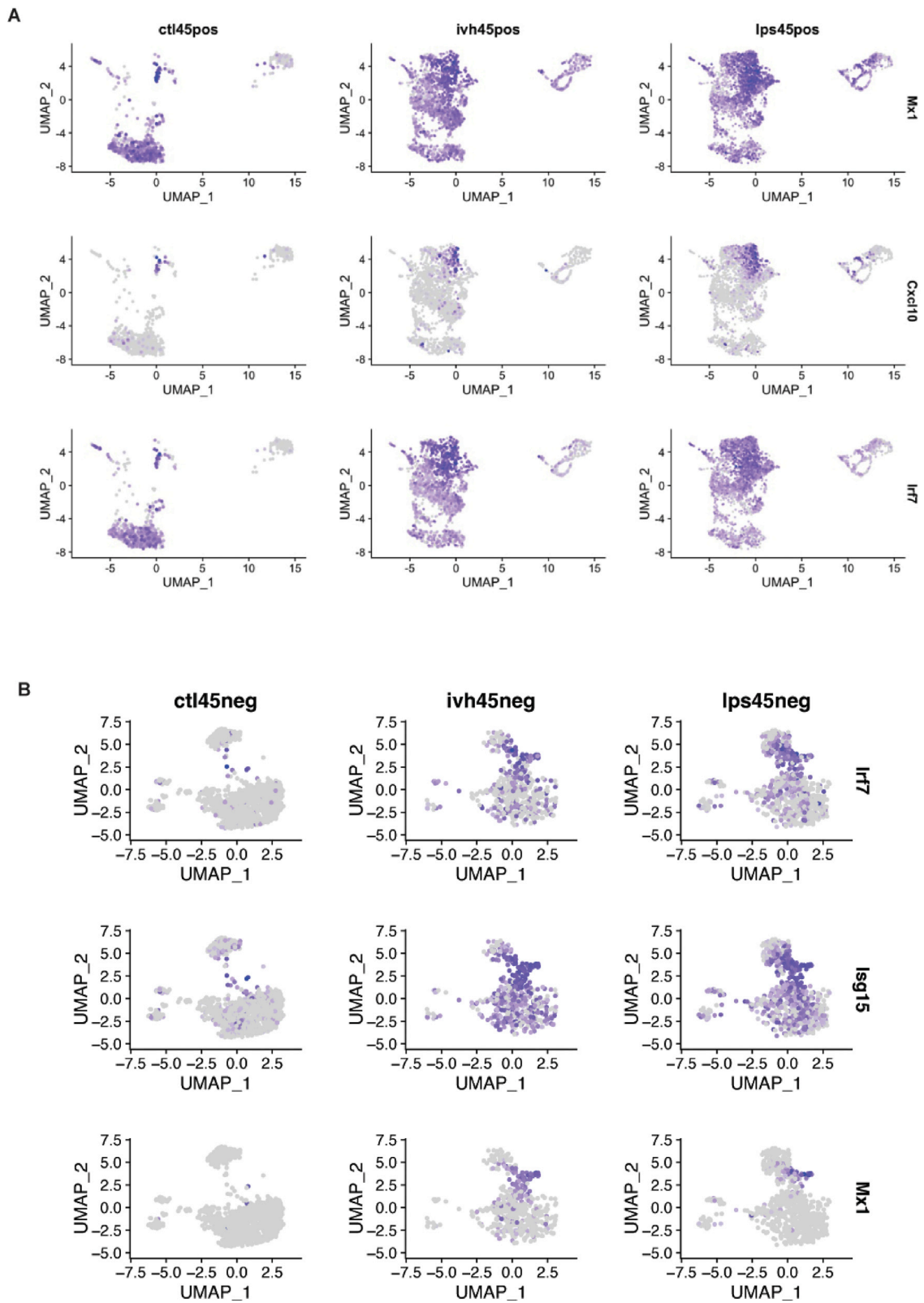


Figure S6. Choroid plexus epithelial and myeloid cells demonstrate expression of key genes in the mTOR/Irf7 pathway, related to Figure 5

(A) Feature plots showing expression of key genes in mTOR/Irf7 pathway in myeloid clusters.

(B) Feature plots showing expression of key genes in mTOR/Irf7 pathway in epithelial clusters.

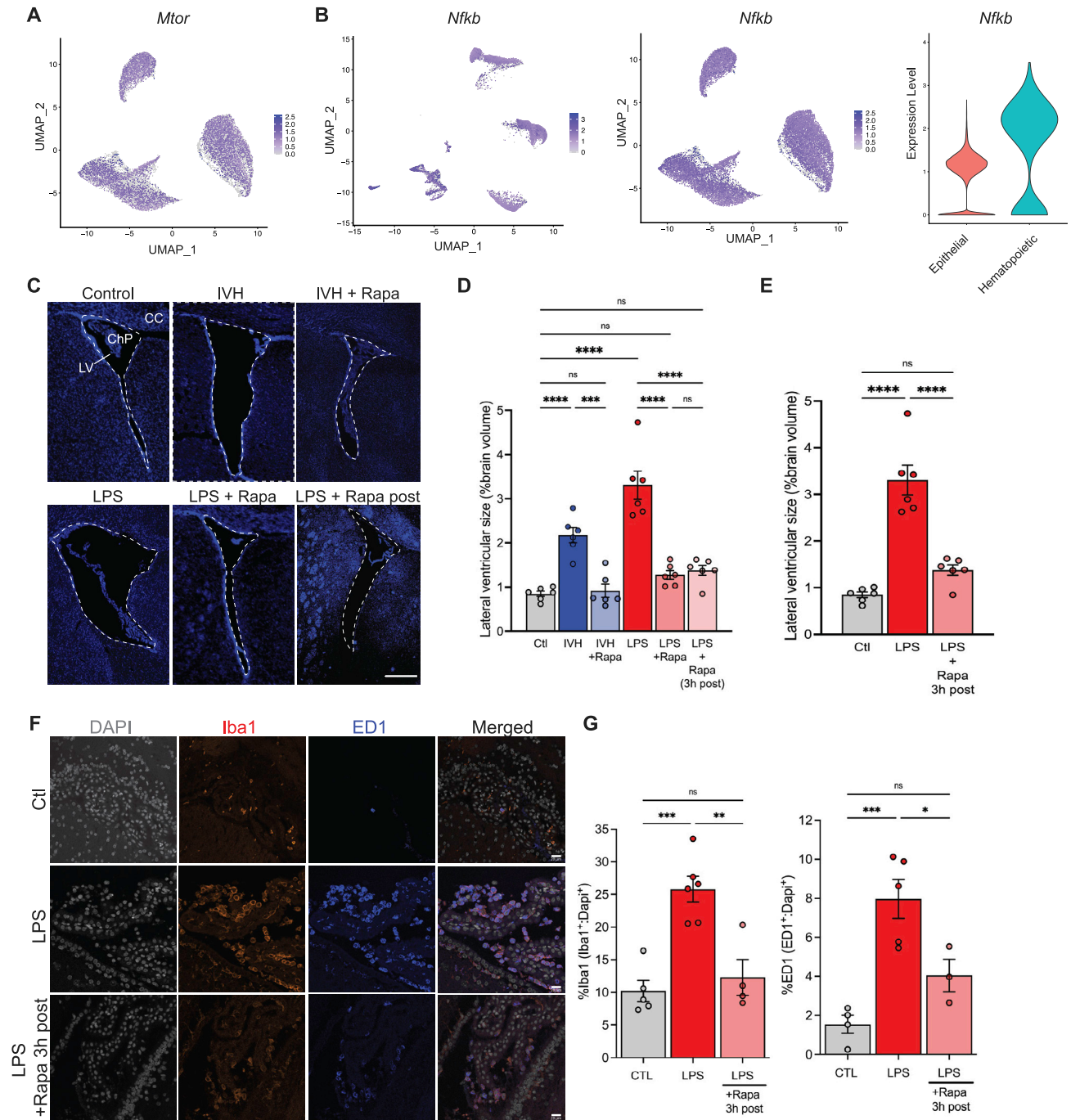


Figure S7. ChP expression of *Mtor* and *NFkB* and treatment of PIH and PHH animals with rapamycin to prevent ventriculomegaly and the ChP immune response, related to Figure 7

(A and B) snRNA-seq analysis of *Mtor* and *NFkB* in the ChP. (A) UMAP of *Mtor* expression across ChP epithelial cell clusters. (B) UMAP of cell ontology (as in Figure S3A) (left panel), ChP epithelial cell clusters (middle panel), and violin plot (right panel) demonstrating *NFkB* expression.

(C) Representative immunohistochemical images of the lateral ventricles (LV) in control, LPS, IVH, LPS ± rapamycin, and IVH ± rapamycin. Rapamycin (Rapa) indicates animals treated with rapamycin prior to LPS administration, Rapa 3 h indicated animal treated with rapamycin after LPS administration. Dashed white line indicating border of lateral ventricle. CC, corpus callosum; ChP, choroid plexus, mag 2.5×.

(D) Quantification of lateral ventricle volume (% brain volume) in control, LPS, IVH, LPS ± rapamycin, and IVH ± rapamycin.

(E) Lateral ventricular size (% brain volume) in Ctl, LPS, and LPS + rapamycin 3 h after initial LPS infusion (Rapa 3 h post) treated animals.

(F) Representative IHC of Iba1 (red) and ED1 (blue) expression in the ChP of rats treated with LPS alone or LPS + Rapa 3 h post. DAPI, white. Scale bars, 20 μm.

(G) Quantitative IHC of the ChP immune response in (F) in control, LPS, and LPS + Rapa 3 h post-treated animals. Graphs represent DAPI-normalized % of cells identified as Iba1⁺ or ED1⁺ in Ctl, LPS, LPS + Rapa 3 h post. N = 3–6 animals per condition. For all graphs, *p < 0.05, **p < 0.01, ***p < 0.001, ****p < 0.0001, ns, not significant, one-way ANOVA. Error bars show mean ± SEM, and each symbol represents average data obtained from an individual animal.